



GRAĐEVINSKI MATERIJALI I KONSTRUKCIJE

BUILDING MATERIALS AND STRUCTURES

Volume 66
March 2023

ISSN 2217-8139 (Print)
ISSN 2335-0229 (Online)
UDK: 06.055.2:62-
03+620.1+624.001.5(49
7.1)=861

1

Society for Materials and Structures Testing of Serbia
University of Belgrade Faculty of Civil Engineering
Association of Structural Engineers of Serbia



CONTENTS

Marija Nedeljković, Nikola Tošić, Erik Schlangen, Sonja Fennis Pre-demolition concrete waste stream identification: classification framework Original scientific paper	1
Vijayalakshmi Ramalingam, Yogesh Balamurugan, Prashant Selvam, Nitish Kanna Kalimuthu, Thosi Giri Influence of biomass ash and coconut shell in scrap steel fiber reinforced concrete Original scientific paper	25
Mohammed Hassoune, Abdelhak Kada, Belkacem Menadi, Belkacem Lamri Numerical thermal performance Aanalysis of light steel insulated walls under fire Technical paper	43
Milena Tomić, Anže Babič, Tatjana Isaković Evaluation of models of the flexural response of rectangular reinforced concrete columns in the post-capping region Technical paper	55
Nađa Simović, Ivan Glišović, Marija Todorović Design of cross-laminated timber (CLT) floors for human-induced vibrations Technical paper	69
Guide for authors	79

EDITORIAL BOARD

Editor-in-Chief

Professor **Snežana Marinković**
University of Belgrade, Faculty of Civil Engineering, Institute
for Materials and Structures, Belgrade, Serbia
e-mail: sneska@imk.grf.bg.ac.rs

Deputy Editor-in-Chief

Professor **Mirjana Malešev**
University of Novi Sad, Faculty of Technical Sciences,
Department of Civil Engineering, Novi Sad, Serbia
e-mail: miram@uns.ac.rs

Associate Editor

Dr. **Ehsan Noroozinejad Farsangi**
Department of Civil Engineering,
The University of British Columbia, Vancouver, Canada
e-mail: ehsan.noroozinejad@ubc.ca

Members

Professor **Jose M. Adam**
ICITECH, Universitat Politècnica de Valencia, Valencia,
Spain

Dr **Ksenija Janković**
Institute for Testing Materials – Institute IMS, Belgrade,
Serbia

Professor Emerita **Dubravka Bjegović**
University of Zagreb, Faculty of Civil Engineering,
Department of materials, Zagreb, Croatia

Professor Academician **Yatchko P. Ivanov**
Bulgarian Academy of Sciences, Institute of Mechanics,
Sofia, Bulgaria

Professor **Tatjana Isaković**
University of Ljubljana, Faculty of Civil and Geodetic
Engineering, Ljubljana, Slovenia

Professor **Michael Forde**
University of Edinburgh, Institute for Infrastructure and
Environment, School of Engineering, Edinburgh, United
Kingdom

Professor **Vlastimir Radonjanin**
University of Novi Sad, Faculty of Technical Sciences,
Department of Civil Engineering, Novi Sad, Serbia

Predrag L. Popovic
Vice President, Wiss, Janney, Elstner Associates, Inc.,
Northbrook, Illinois, USA

Professor **Zlatko Marković**
University of Belgrade, Faculty of Civil Engineering,
Institute for Materials and Structures, Belgrade, Serbia

Professor **Vladan Kuzmanović**
University of Belgrade, Faculty of Civil Engineering,
Belgrade, Serbia

Professor Emeritus **Valeriu A. Stoian**
University Politehnica of Timisoara, Department of Civil
Engineering, Research Center for Construction
Rehabilitation, Timisoara, Romania

Dr **Vilma Ducman**
Head of Laboratory for Cements, Mortars and
Ceramics, Slovenian National Building and Civil
Engineering Institute, Ljubljana, Slovenia

Assistant Professor **Ildiko Merta**
TU Wien, Faculty of Civil Engineering, Institute of
Material Technology, Building Physics, and Building
Ecology, Vienna, Austria

Associate Professor **Ivan Ignjatović**
University of Belgrade, Faculty of Civil Engineering,
Institute for Materials and Structures, Belgrade, Serbia

Professor **Meri Cvetkovska**
University "St. Kiril and Metodij", Faculty of Civil
Engineering, Skopje, Macedonia

Dr **Anamaria Feier**
University Politehnica of Timisoara, Department for
Materials and Manufacturing Engineering, Timisoara,
Romania

Associate Professor **Jelena Dobrić**
University of Belgrade, Faculty of Civil Engineering,
Institute for Materials and Structures, Belgrade, Serbia

Dr **Vladimir Gocevski**
Hydro-Quebec, Mécanique, structures et architecture,
Ingénierie de production, Montréal (Québec), Canada

Dr **Nikola Tošić**
MSCA Individual Fellow, Civil and Environmental
Engineering Department, Universitat Politècnica de
Catalunya (UPC), Barcelona, Spain

Secretary:

Slavica Živković, Master of Economics
Society for Materials and Structures Testing of Serbia, 11000 Belgrade, Kneza Milosa 9
Telephone: 381 11/3242-589; e-mail: office@dimk.rs, veb sajt: www.dimk.rs

English editing:

Professor **Jelisaveta Šafranj**, University of Novi Sad, Faculty of Technical Sciences, Novi Sad, Serbia

Technical support:

Stoja Todorović, e-mail: saska@imk.grf.bg.ac.rs

Aims and scope

Building Materials and Structures aims at providing an international forum for communication and dissemination of innovative research and application in the field of building materials and structures. Journal publishes papers on the characterization of building materials properties, their technologies and modeling. In the area of structural engineering Journal publishes papers dealing with new developments in application of structural mechanics principles and digital technologies for the analysis and design of structures, as well as on the application and skillful use of novel building materials and technologies.

The scope of Building Materials and Structures encompasses, but is not restricted to, the following areas: conventional and non-conventional building materials, recycled materials, smart materials such as nanomaterials and bio-inspired materials, infrastructure engineering, earthquake engineering, wind engineering, fire engineering, blast engineering, structural reliability and integrity, life cycle assessment, structural optimization, structural health monitoring, digital design methods, data-driven analysis methods, experimental methods, performance-based design, innovative construction technologies, and value engineering.

Publishers	Society for Materials and Structures Testing of Serbia, Belgrade, Serbia, veb sajt: www.dimk.rs University of Belgrade Faculty of Civil Engineering, Belgrade, Serbia, www.grf.bg.ac.rs Association of Structural Engineers of Serbia, Belgrade, Serbia, dgks.grf.bg.ac.rs
Print	Razvojno istraživački centar grafičkog inženjerstva, Belgrade, Serbia
Edition	quarterly
Peer reviewed journal	
Journal homepage	www.dimk.rs
Cover	Mixed concrete streams at the recycling plant , <i>from Pre-demolition concrete waste stream identification: Classification framework</i> by Marija Nedeljković, Nikola Tošić, Erik Schlangen and Sonja Fennis
Financial support	Ministry of Education, Science and Technological Development of Republic of Serbia University of Belgrade Faculty of Civil Engineering Institute for testing of materials-IMS Institute, Belgrade Faculty of Technical Sciences, University of Novi Sad, Department of Civil Engineering Serbian Chamber of Engineers

CIP - Каталогизacija u publikaciji
Narodna biblioteka Srbije, Beograd

620.1

GRAĐEVINSKI materijali i konstrukcije = Building materials and structures / editor-in-chief Snežana Marinković
. - God. 54, br. 3 (2011)- . - Belgrade : Society for Materials and Structures Testing of Serbia : University of Belgrade, Faculty of Civil Engineering : Association of Structural Engineers of Serbia, 2011- (Belgrade : Razvojno istraživački centar grafičkog inženjerstva). - 30 cm

Tromesečno. - Je nastavak: Materijali i konstrukcije
= ISSN 0543-0798. - Drugo izdanje na drugom medijumu:
Građevinski materijali i konstrukcije (Online) = ISSN 2335-0229
ISSN 2217-8139 = Građevinski materijali i konstrukcije
COBISS.SR-ID 188695820



Pre-demolition concrete waste stream identification: classification framework

Marija Nedeljković^{*1,2)}, Nikola Tošić³⁾, Erik Schlangen¹⁾, Sonja Fennis²⁾

¹⁾ Delft University of Technology, Faculty of Civil Engineering & Geosciences - Section of Materials & Environment, Stevinweg 1, 2628 CN Delft, The Netherlands

²⁾ Rijkswaterstaat, Ministry of Infrastructure and Water Management, Griffioenlaan 2, 3526 LA Utrecht, The Netherlands

³⁾ Universitat Politècnica de Catalunya, Civil and Environmental Engineering Department, Jordi Girona 1-3, 08034 Barcelona, Spain

Article history

Received: 22 November 2022

Received in revised form:

19 January 2023

Accepted: 21 February 2023

Available online: 30 March 2023

Keywords

concrete quality,
strength, composition,
in situ non-destructive testing,
characteristic quality indicators,
handheld XRF

ABSTRACT

Demand for high quality recycled concrete aggregates (RCA) to offset the use of primary materials is significantly rising due to circular economy goals and high-value reuse of concrete. The quality of RCA significantly affects their availability for new concrete production due to the variability of parent concrete streams. The optimization of recycling procedures is under development to improve the quality of RCA, however, the costs and energy efficiency of such processes are of practical concern. With this in mind, this paper presents a new framework for reducing the variability of RCA quality by identifying concrete members before their demolition. The goal of identifying demolished concrete members from a structure is to provide groups of concrete members with similar mechanical and chemical properties through a systematic classification of the structural members.

The quality assessment of concrete structures and their mechanical and chemical (composition, contamination) properties prior to demolition is generally recognized as challenging due to the absence of guidelines and the lack of easy-to-use in situ characterization techniques. This paper proposes experimental approaches that can non-destructively determine the properties of concrete structures, with a major emphasis on the measurement of the chemical composition of concrete before demolition. Characteristic quality indicators to classify concrete members are first proposed and can be instrumental in setting up future studies. A new method is proposed for in situ chemical composition testing of existing concrete structures; assuming that no records about the parent concrete are available. Next, the challenging parameters for in situ, non-destructive measurements are outlined. The practical application of the proposed method and its uptake in industry can potentially unlock a huge potential for optimized material recovery and contribute greatly to a fully circular construction industry.

1 Introduction

Globally, the construction industry is expanding rapidly [1], while transportation infrastructure is facing significant challenges due to aging, rapid growth in traffic loads, and changing circumstances of existing structures (natural and man-made resilience threats) [2]. As a consequence, a significant amount of construction and demolition waste (CDW) is generated. CDW contains concrete, brick, wood, metal, drywall, plastics, glass, and others [3], of which concrete waste forms the largest part. In Europe, CDW is assessed to be 25–30% of the total waste [4], whereas the level of recycling is still highly variable between the member states [5]. Most countries globally and within the EU still have low performance in CDW generation, management, and recycling [5] because of ineffective CDW regulations; poor data quality; poor reverse logistics; and a low market

readiness for secondary materials [3]. Other sources of demolished concrete are residential and non-residential buildings, civil engineering structures, and the building and pavement industries [6], amongst others. Demolition of concrete structures can have various causes. Primary causes of structural failures, and consequently demolition are poor construction procedures, inadequate assemblage of concrete members, and inadequate behaviour under load [7, 8]. In the Netherlands, for example, the majority of bridges and viaducts in the main highway network have been demolished in the past for functional reasons (improved traffic flow on the road network and railway construction), and the rest were demolished due to technical reasons such as insufficient load-bearing capacity (design loads, accidental overload, deterioration) [9]. Fig. 1. gives an example of demolition. The Hoog Burel viaduct over the A1

* Corresponding author:

E-mail address: M.Nedeljkovic@tudelft.nl

in the Netherlands was more than 50 years old, and the concrete had deteriorated.

Such demolitions have so far primarily been carried out without significant preselection, in particular, without any preselection of concrete. Furthermore, the recycling process principally consisted of simply crushing the waste concrete, which inevitably entailed a degradation in quality [11]. Although in the past two decades, significant effort has been made towards the advancement of concrete recycling and many achievements have been made in both the treatment and application of recycled concrete aggregates (RCA), their use is still very limited in new concrete structures. This is due to the fact that the recycling is mainly focused on mixed concrete streams and, therefore, the quality of RCA is a major concern for concrete producers (Fig. 2).

To address this issue, simple, non-destructive in situ characterization techniques that enable pre-selection prior to demolition and waste stream separation based on concrete properties are required. With this in mind, the primary goal of this paper is to propose a workflow for use in demolition projects that is based on in-situ quality assessment of parent concrete and non-destructive testing. The paper proceeds as follows: Section 2 presents the current demolition and recycling practices that do not rely on selective demolition; Section 3 examines concrete input properties for selective demolition; Section 4 presents a specific workflow towards a selective demolition-based recycling of concrete; Section 5 presents non-destructive in situ concrete characterization techniques; Section 6 outlines further research needed on testing of concrete composition; and Section 7 concludes the paper.



Fig. 1. Demolition of Hoog Burel viaduct (A1), the Netherlands: a) before demolition, b) during demolition (November 2022). Credits go to Rijkswaterstaat [10]



Fig. 2. Mixed concrete streams at the recycling plant

2 Demolition and recycling without prior concrete characterization

The way we handle waste now is based on several EU guidelines, such as the Circular Economy Action Plan [12], the EU Directive 98/2008/EC [13], the EU Directive 2018/851/EC [14], the EU Construction and Demolition Waste Management Protocol [15], and the Guidelines for Waste Audits Before Building Demolition and Renovation [16]. However, concrete producers, construction engineers and real state owners are sceptical towards recycled aggregate concrete since RCA are typically heterogeneous [17] and of lower quality than natural aggregates [18]. In particular, engineers are faced with uncertainties when they have the opportunity to design structural recycled aggregate concrete members [19]. Quality assurance and certification are of paramount importance in order to address these reservations. It is very difficult, if not impossible, to demolish a concrete structure for which there is prior knowledge about the origin and properties of all concrete components. Information about the composition (cement, aggregates, fibres, coating) of each concrete member (strength class, with/without reinforcement, type of reinforcement), and their degree of contamination, is difficult to obtain. Furthermore, they may have been exposed to different environmental conditions (under varying conditions of drying and wetting, chloride environment, carbonation, chemical attack, alkali-aggregate reactions, etc.) [20].

Demolished concrete members can be crushed and processed on site with mobile crushers, or they can be transported to the recycling plant [21]. Preliminary manual sorting is conducted in order to eliminate hazardous materials (e.g., bituminous roofs) and further sorting with magnet pads to segregate metals [22]. Within such a process, there have also been recent advances in automating and robotizing the procedure. For example, ZenRobotics is an advanced and recently applied technology for efficient sorting of input materials (metals, wood, stone, and inert materials) with a heavy-duty picker sorting line (Fig. 3). ZenRobotics uses standard industrial robots and, depending on the application, equips them with a variety of sensors, detectors, and scanners, along with artificial intelligence software, to ensure maximum efficiency. The unit contains near-infrared spectroscopy, hyperspectral imaging sensors, a 3D sensor system, a high-resolution RGB camera, a metal imaging sensor, and a visual light spectrum sensor [23].

As for the recycling process, RCA are produced using the same equipment traditionally used in quarries for the production of natural aggregates, and their appearances are shown in Fig. 4. The most commonly used crushers are jaw and impact crushers [24].

The traditional production processes result in RCA with suitable properties for concrete, provided the CDW are of good enough quality after the initial separation. However, better recovery rates, faster and more efficient production, higher quality recycled aggregates, and additional types of recovered materials (e.g., recycled fines and cement) with suitable quality may be obtained with technologically advanced processes.

Examples of such advances are the Smart Crusher and Concrete to Cement and Aggregate (C2CA). The Smart Crusher separates concrete waste into gravel, sand, and cement with minimal damage to each of these constituents. This is achieved by adjusting the crushing force to an intermediate value between the average compressive strength of the aggregates and that of the hardened cement paste [25, 26]. In order to exert the right force on the aggregates, crushing and grinding are combined. C2CA technology combines a mechanical-based process, the Advanced Dry Recovery (ADR), with a thermal-based one, the Heating-Air Classification System (HAS). Both are mobile technologies suitable for on-site recycling of end-of-life concrete waste. The combination of these technologies is used to recover concrete waste into three product streams: coarse recycled aggregates (4–12 mm), fine recycled aggregates (0.25–4 mm), and an ultrafine fraction (<0.25 mm). While ADR is a mechanical system that crushes and sorts wet concrete wastes according to their particle size, HAS uses a combination of thermal and air classification methods to separate and activate the hydrated cement paste [27].

At the moment, all of these technologies are more expensive and more energy-consuming relative to established ones, making such recycled aggregates economically unviable as a competitive alternative to concrete made of natural aggregates. The energy consumption of RCA production was measured and plotted against the water absorption of coarse RCA in conventional and advanced recycling processes [28]. On the one hand, energy consumption was up to 62 times higher with advanced recycling processes than in the case of ordinary concrete recycling. On the other hand, water absorption has decreased.



Fig. 3. ZenRobotics technology heavy picker sorting line [23]

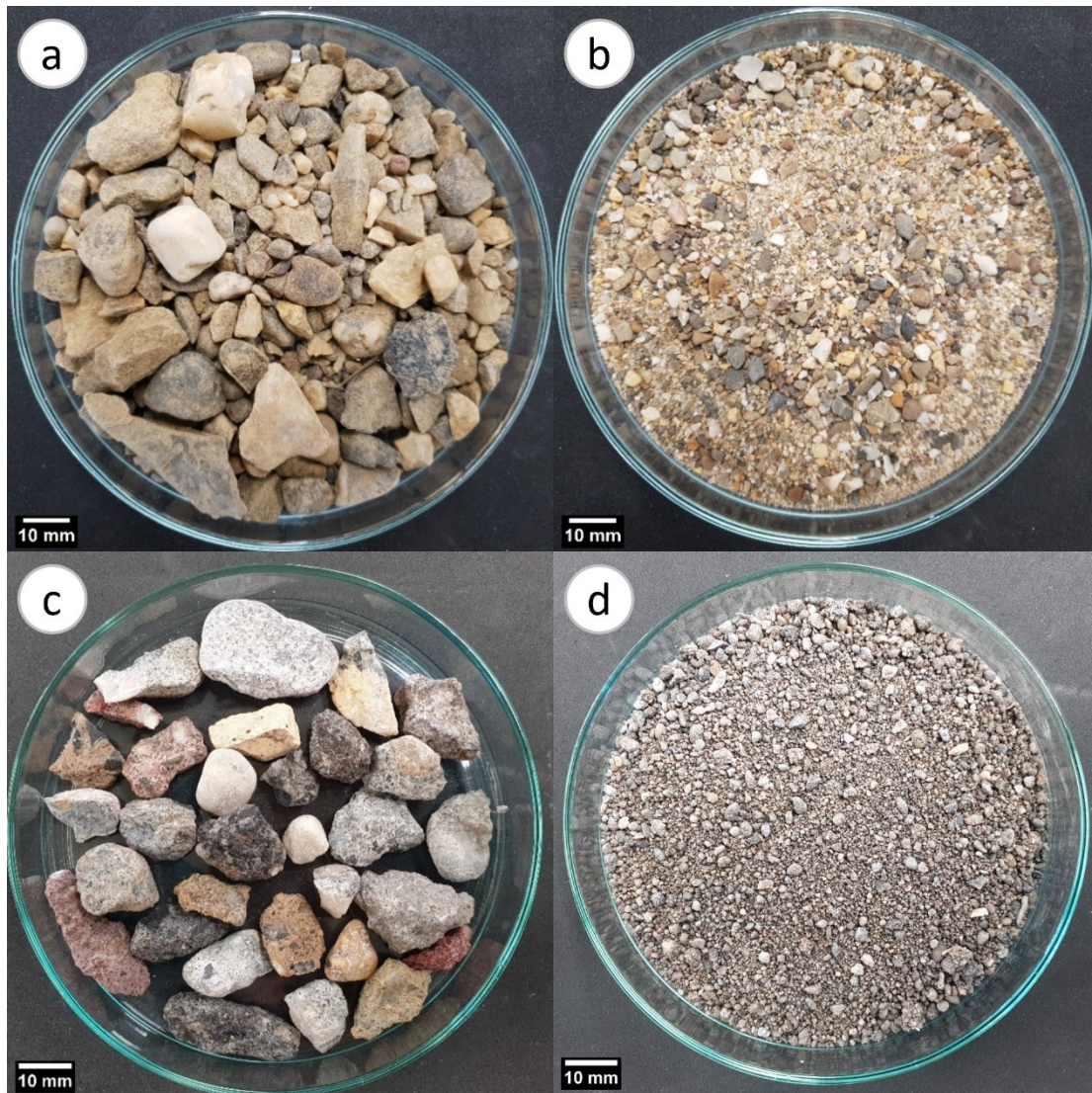


Fig. 4. Crushed natural materials (a) gravel and (b) sand versus recycled concrete aggregates (c) coarse and (d) fine

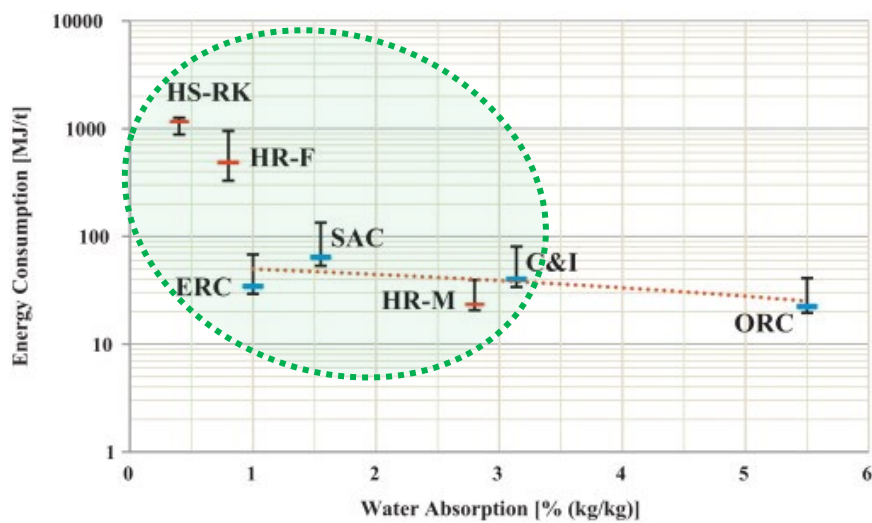


Fig. 5. Energy consumption per metric tonne (allocated to fine and coarse fraction) vs water absorption of RCAs subjected to advanced recycling processes. ORC (ordinary recycling); ERC (eccentric rotor crusher); C&I (compression and impact); SAC (screw abrading crusher); HR-M (heating by microwave oven and rubbing); HR-F (heating by kerosene furnace and rubbing); HS-RK (heating by rotary kiln and sorting), adopted from [28]

In addition, none of these advanced recycling techniques can recognize the quality of the input concrete waste. Such information can be of extremely high value for the wider application of RCA in producing structural concrete, that is, recycled aggregate concrete [29]. Therefore, selective/gradual demolition and sorting of concrete waste is another route for ensuring the correct management of recycled material. However, this route is not a preferred practice by demolition contractors for a number of reasons, such as insufficient space at the demolition site, too little time for additional sorting, or excessively low efficiency due to small quantities of waste to be sorted in different streams [30]. Furthermore, there are no specific workflows or visualisation tools established for selective demolition. Moreover, selective demolition was shown to induce high costs for the demolition sector [31]; the actual effort, if measured in time, skills, and labour, is significantly higher than for conventional demolition [5]. However, adaptive planning of the deconstruction works and ways of optimising cost-effective processes can also lead to considerable reductions in deconstruction duration and costs [31, 32]. In addition, if design codes emphasise the environmental aspects of the construction and give designers more opportunities for material sourcing, the chances of reuse through smart demolition and/or selective dismantling can be enhanced [32].

3 Concrete input properties for selective demolition

Visualisation tools allow for selective dismantling planning and therefore also allow one to foster demolition practices according to waste management priorities [33]. For correct concrete for waste management, it is necessary to define characteristic quality indicators for parent concrete. The RCA properties and parameters affecting new concrete are water absorption, composition, alkali-silica reactivity, contamination, and other critical parameters that may be related to compressive strength. Those parameters and their effect on new concrete are further examined, which led to the selection of key characteristic quality indicators for parent concrete screening in Section 3.5.

3.1 Compressive strength of parent concrete

The characteristic concrete compressive strength at 28 days is the value used by structural engineers for the design of new concrete structures. By evaluating fundamental parameters such as the compressive strength of parent concrete before demolition, crucial properties of RCA before their use in new concrete can be predicted. One of the distinguishing features of RCA is their water absorption. In a systematic literature review, Silva et al. [34] concluded that the increasing strength of the parent concrete may cause a reduction in the water absorption of the resulting RCA. In fact, Kou and Poon [35] examined the effect of the wide range of parent concrete strengths on the water absorption of RCA. RCA, derived from stronger parent concrete, had lower water absorption values. This effect was more distinct for RCA, with a maximum particle diameter of 10 mm compared to 20 mm [35].

Table 1 summarizes experimental data from the literature on the 28-day compressive strength of fine or coarse RCA concrete in relation to the parent concrete's source and strength. It must be noted that in the majority of reviewed studies in the literature, the properties of the parent concrete were unknown, and RCA was produced from a mix of concrete waste from different sources and of unknown quality [36-40]. Therefore, such studies were not reported in Table 1. Nonetheless, these studies demonstrated how difficult it is to explain the properties of new concrete with RCA when information on the parent concrete's quality is unavailable.

The compressive strength of concretes with coarse as well as fine RCA fluctuated: it was higher, the same, or lower compared to a reference concrete. The compressive strength is rather sensitive to the high replacement level of RCA (100%), irrespective of the binder composition or cement content, as earlier reported [20]. As Table 1 shows, there is no significant difference between the sources of parent concrete: field or lab concrete, however, there is a significant difference with regard to their compressive strengths. Pedro et al. [41] studied the effect of using RCA (100% replacement of natural coarse aggregates) from different sources (precast rejects or laboratory concrete, with target strengths of 20 MPa, 45 MPa and 65 MPa) on properties of new concrete mixes with target strengths of 20 MPa, 45 MPa and 65 MPa, respectively. The loss of compressive strength of concrete with RCA was less for mixes with higher target compressive strengths (45 MPa and 65 MPa) compared to mixes with lower target compressive strengths (20 MPa). This finding is in line with other studies [42, 43]. The results showed that in terms of compressive strength, the replacement of 100% natural coarse aggregates would be possible when RCA are produced from parent concrete with a minimum compressive strength of 60 MPa [43]. In another study [44], more representative for field-demolished concrete, the compressive strength of parent concrete was 35 MPa and 23 MPa (a 40-year-old highway bridge). The new concrete mixtures were designed with a target 28-day compressive strength of 35 MPa. Concrete with 100% coarse RCA had an 8% lower 28-day compressive strength when produced with the same effective water-to-cement ratio as normal aggregate concrete, while other properties (shrinkage and creep) were comparable [44]. The study by Lotfi et al. [27] demonstrated that recycled aggregate concrete achieved higher compressive strength compared to natural aggregate concrete up to 30% at early ages, and after 90 days this difference became lower, at 5%. In terms of concrete deformations and durability, the concrete mixtures made with RCA derived from parent concrete with higher strength had lower drying shrinkage and higher resistance to chloride ion penetration [35]. It has also been reported that the compressive strength of parent concrete increases its resistance to fragmentation [45]. Overall, studies highlight the need to determine the strength of parent concrete, based on which realistic qualities can be targeted for recycled aggregate concrete [46].

Table 1. Parent concrete strength and 28-day compressive strength of concrete with RCA produced from respective parent concrete

	Parent concrete		28-day compressive strength of concrete with RCA produced from parent concrete													
	*Source/recycling technique	Strength	0%	5%	10%	15%	20%	25%	30%	40%	45%	50%	60%	75%	80%	100%
Fine RCA																
Evangelista [47]	Lab, jaw crusher	29.6 MPa	59.3		59			57.3		57.1		58.8				54.8
Levy [48]	Field (6 months old concrete)	25 MPa	48.5					56.1				46.3				46.6
Yaprak[49]	Lab, jaw crusher	C30/37	45		42			41		40	38	36				29
Pereira [50]	Lab, jaw crusher	37.3 MPa	39.5		40					38.6		37.6				38.6
Pereira (SP1)[50]	Lab, jaw crusher	37.3 MPa	53.3		53.7					51		47.8				45.1
Pereira (SP2)[50]	Lab, jaw crusher	37.3 MPa	65.2		64.6					65.4		63.2				63
Khoshkenari (AW)[51]	Lab, jaw crusher	30 MPa	38													27.9
Khoshkenari (SP)[51]	Lab, jaw crusher	30 MPa	38													32.8
Cartuxo [52, 53]	Lab, jaw crusher	C30/37	49.37		51.17					47.21		43.53				41.2
Cartuxo (SP1)[52, 53]	Lab, jaw crusher	C30/37	66.79		63.86					61.65		58.73				47.36
Cartuxo (SP2)[52, 53]	Lab, jaw crusher	C30/37	80.64		77.41					71.73		69.31				64.72
Bogas (NC)[54]	Lab, jaw crusher	C25/30	50.2					49.9				47.4				43.1
Bogas (HC+SP)[54]	Lab, jaw crusher	C25/30	81					72.7				67.4				58.8
Bogas (HC+SP+AEA)[54]	Lab, jaw crusher	C25/30	67.9					61.8				52.1				44.9
Evangelista[55, 56]	Lab, jaw crusher	28.7 MPa	33.6		32.1					32.7		32.8				30.7
Coarse RCA			0%	5%	10%	15%	20%	25%	30%	40%	45%	50%	60%	75%	80%	100%
Kou [35]	Lab, jaw crusher	35.8 MPa	70													50
Kou [35]	Lab, jaw crusher	51.1 MPa	70													55
Kou [35]	Lab, jaw crusher	61.8 MPa	70													62
Kou [35]	Lab, jaw crusher	87.9 MPa	70													70
Kou [35]	Lab, jaw crusher	101.7 MPa	70													72
Pedro [41]	Rejected concrete produced by precast concrete company	20 MPa	24													22
Pedro [41]	Rejected concrete produced by precast concrete company	45 MPa	39													35
Pedro [41]	Rejected concrete produced by precast concrete company	65 MPa	71													68
Radonjanin [57]	Field and lab	C30/37 and C45/55														44.2
Thomas [58]	Field	25 MPa	35.8						34.6			33.1				30.2
Andreu [43]	Rejected concrete produced by precast concrete company	100 MPa	102.1					108				104.8				108.5
Andreu [43]	Lab, jaw crusher	60 MPa	102.1					102.5				103.1				100.8
Andreu [43]	Rejected concrete produced by precast concrete company	40 MPa	102.1					104.3				96.8				91.2
Tošić [44]	Field (40 years old concrete)	35 MPa and 23 MPa	40.7													37.4
Geng [59]	Lab, jaw crusher	37.5 MPa	39.2													38.9
Geng [59]	Field (40 years old concrete)	38 MPa	39.2						30.8			30.1				25.9

The strength of the parent concrete may also have an impact on the amount of energy required for crushing. In the context of crushability tests, there are no data on the impact of the physical and mechanical properties of concrete on the energy consumption of a crusher during concrete crushing. For this reason, hard rocks will be discussed because of their similarities with concrete (artificial rock). Laboratory studies showed that the crushability of hard rocks is directly associated with the rock strength and mineralogical composition [60]. Rocks with a higher uniaxial compressive strength are "harder" to crush resulting in an increased share of larger particles and the need to use more energy for crushing [61]. Fig. 6 shows the dependence of the specific

crushing energy on the compressive strength of the rocks [61]. In the same study, it was shown that fracture toughness and tensile strength also significantly affect the crushing energy. The impact of bulk density is not large, while hardness has only a minor impact. It is believed that, similar to the increase in energy with the strength of rock, concrete with a higher strength class consumes more energy for crushing in order to achieve the required particle size. During the size reduction processes in a jaw crusher and rod mill for quartz ore (density 2800 kg/m³) with a density slightly higher than that of normal concrete (2400 kg/m³), crushing and grinding energy consumption increase when finer size fractions of the product are desired [62], Fig. 7.

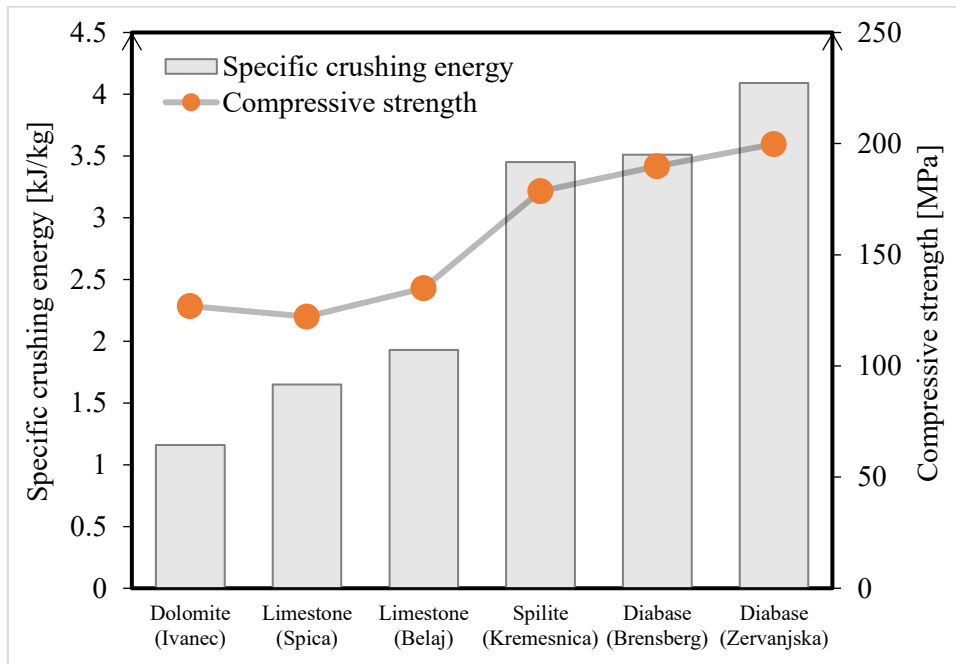


Fig. 6. Dependence of crushing energy on the compressive strength for various rocks [61]

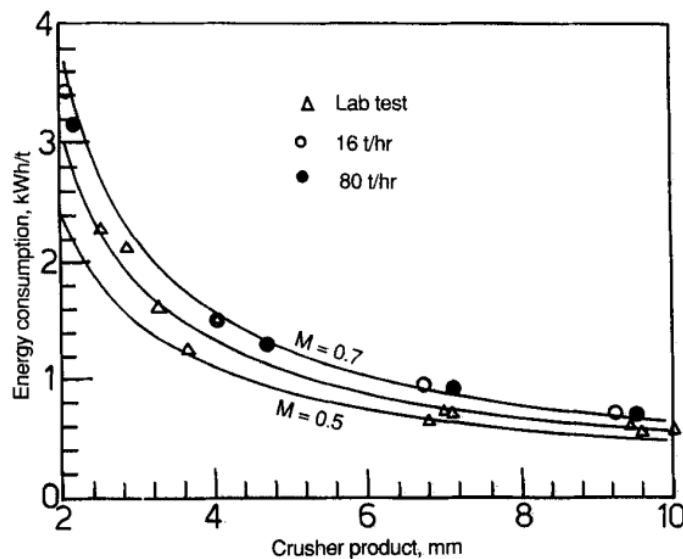


Fig. 7. Energy consumption in different crushing flowsheets, adopted from [62]

3.2 Composition of parent concrete

RCA are the least homogeneous in mechanical, chemical, and composition properties, since they originate from many different concrete waste streams. The chemical composition of the CDW, and therefore of the RCA, shows great variability [63]. The element with the highest average content is Si (47%), with values ranging from 8 to 77%. The proportion of CaO is also high (20% on average) and varies between 4 and 47%. Other components such as Al, Fe, Mg, S, and different alkalis follow as secondary elements. Other minor elements (Mn, P, Sr, Ti), may be present as well. Testing the parent concrete composition can provide two types of information, composition of major components in concrete and possible minor elements and contamination. Other reasons for testing the composition of concrete components before demolition are discussed below.

3.2.1 Identification of cement type

This information can assist in deciding on the application for recycled material. For example, based on cement type, one can decide whether the fine recycled concrete aggregates (fRCA) would be valuable for:

- Alternative raw materials
 - mineral addition for clinker manufacturing. If the use of RCA in concrete mix design is limited by their physical or chemical properties (high absorption, sulphates or alkalis content, etc.), they can be used as raw materials for cement production [63]. The studies show that if the RCA composition, cement type, and cement quarry composition are known, it is possible to produce Portland clinker using RCA as raw materials [63-66]. Schoon et al. [64] incorporated the concrete fines in cement raw meal replacing siliceous materials due to the high SiO₂ contents of recycled materials. However, the percentages of RCA incorporation in the cement raw meal vary greatly, mainly due to the variation in RCA's chemical composition and the use of different natural raw materials (clays and limestone). It was shown that the maximum incorporation rate is mainly between 10–20% (50% of the 180 raw meal calculations), occasionally lower than 5% (13%), or higher than 30% (17%) [63]. The incorporation rates of CDW in an OPC clinker are directly controlled by the CaO or SiO₂ content [63]. The use of CDW for cement production requires better taking into account the effect of the natural raw materials and the RCA chemical composition variability. This is an example of how knowing the composition of RCA can improve clinker manufacturing by avoiding the addition of undesired components, such as clays. Other study reported a greater amount of phyllosilicates in the fine fraction compared to the other fractions [67]. Therefore, the authors indicate that if one is to use recycled fine fractions in mortars and concrete, careful sorting must be carried out to limit the presence of clays.
 - pozzolanic materials [68], in which case the fine fraction of RCA should contain adhered mortar that consists of pozzolanic materials such as fly ash, silica fume, and naturally calcined pozzolana and has a siliceous or silico-aluminous composition as defined by EN 197-1:2011. It should be noted that fRCA and other pozzolanic materials have to be heated. It indeed has an environmental and economic impact, but it may result in more valuable material.
 - fillers [69-72], the candidates would be fRCA with a high CaO or SiO₂ content. These candidates would be

potential alternatives to traditional fillers such as limestone and quartzite.

- As an activator for ground granulated blast furnace slag and pozzolanic materials

Recycled concrete fines can be used for blended cements with the role of an activator. For example, thermally treated fRCA, when dissolved in water, can activate ground granulated blast furnace slag [73] or fly ash [74]. When combined with slag cement, the fine fraction of RCA improves compressive strength when compared to reference mortar (70% slag + 30% CEM I 42.5N) by providing lime for slag dissolution [75]. This occurs only if fRCA originates from OPC-based concrete, which can be known only if parent concrete composition is known.

- CO₂ sequestration

If CO₂ sequestration is the goal of using RCA, the most suitable cement type in adhered mortar in RCA is OPC, which contains the highest levels of CaO and calcium hydroxide (Ca(OH)₂) that can react with CO₂. The addition of fly ash or ground granulated blast furnace slag in partial substitution of OPC decreases the initial content of CaO in the cement matrix, and consequently, it lowers the amount of Ca(OH)₂ to be formed as a result of the cement hydration reaction.

- Durability aspect

When the concrete contains cement with high Al₂O₃ content, such as fly ash- (CEM II) or slag-based cement (CEM III), chloride binding by the cement matrix significantly increases (decreasing free Cl⁻ in the pore solution), as compared to reference concrete made without fly ash [76], which is beneficial for the application of such recycled material in new concrete, where chloride ingress resistance is required. This is yet another example of how knowing the composition of cement in parent concrete can have a beneficial impact on the durability of new concrete with RCA.

3.2.2 Identification of aggregate type

The aggregates of the concrete to be recycled have a large influence on the quality of the future recycled aggregates. For example, as shown in Table 1, different aggregate types lead to different compressive strengths. Furthermore, knowing the composition of aggregates in the parent concrete would assist in determining whether such aggregates would be suitable for the production of fillers usually used for production of concrete, such as limestone filler. In the study of Oksri-Nelfia et al. [72], parent concrete was made with limestone aggregates. Recycled crushed concrete fines (RCCF) had particles with a diameter smaller than 80 μm. The results show that the influence of RCCF on cement hydration is similar to that commonly observed for limestone filler. Fines of up to 25% can be used without affecting the properties of mortars [72]. In another study, Schoon et al. [64] used recycled concrete fines in cement raw meal to replace siliceous materials because the recycled concrete fines had a high SiO₂ content. Knowing the composition of aggregates in the parent concrete may prevent damage to the new concrete with RCA at high temperatures. It has been found that the performance of the recycled aggregate concretes was inferior to that of natural aggregate concrete under high-temperature in terms of the

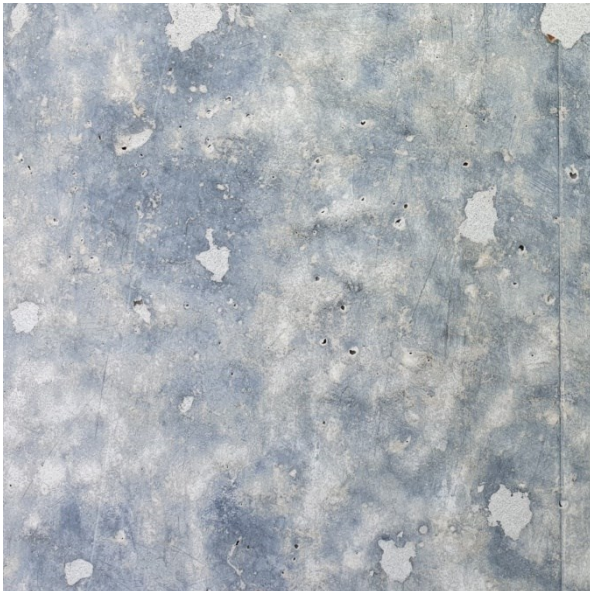
residual properties [77]. The rate of crack growth increased as the temperature rose. This behaviour was explained by the presence of flint in the original aggregates of RCA, which increased in volume during heating [78, 79]. Together, these studies [64, 72, 77] indicate that aggregate characterization in parent concrete is greatly important for predicting the properties of RCA.

3.3 Appearance of sound and potentially damaged concrete

A general definition of the appearance of potentially unhealthy or healthy concrete does not exist [80]. The appearance of a concrete surface can change as a result of ageing, loading, or interaction with the environment to which it is exposed [81], as illustrated in Fig. 8. Newly built reinforced concrete is approximately homogeneously coloured, whereas a long-used concrete structure can suffer for multiple reasons (Figs. 8a–b). Concrete can be painted or

coated (Figs. 8c–d). Efflorescence usually appears as a white coating on the external surface of a concrete slab. A typical example of efflorescence formed by deposits of CaCO_3 is shown in Fig. 8e. The appearance of algae is demonstrated in Fig. 8f. The signs of unhealthy concrete are mostly visible from the surface as disintegrated concrete or severe cracking, Fig. 8g-h. If one wants to study any deleterious effects in depth from the surface, then the samples need to be extracted and analysed in the laboratory. The major deleterious effects, chloride ingress, sulphate attack, and alkali aggregate reactions and their assessment will be further discussed in detail in Section 3.4. These three mechanisms are selected as being critical for concrete contamination and, therefore, need to be considered in the selective demolition of concrete. Other deleterious effects are not addressed, such as carbonation, freeze-thaw attack, and fire. In fact, they do not introduce deleterious contaminants in the concrete that will affect the quality of RCA.

a)



b)



c)



d)





Fig. 8. Concrete surface texture examples: (a) newly built reinforced concrete and formwork marks, (b) spall, (c) white paint, (d) remained coating, (e) efflorescence, (f) algae, (g) crack, dirt and rust stain, (h) steel corrosion and concrete cover damage

3.4 Contamination of parent concrete

The potential contamination of RCA imposes an added challenge for their use given that there might be deleterious pathologies in parent concrete waste streams, such as de-icing salts, sulfate attack, and alkali-silica reaction (ASR). The parent concrete contamination referred to here is related to two aspects, external and internal, as illustrated in Fig. 9.

External contamination of the parent concrete is mainly limited to the concrete cover and, as such, has an insignificant influence on the properties of the RCA. RCA has been shown in several studies to have negligible chloride content (less than 0.01% by mass of aggregate [82, 83]) and water-soluble sulfates below the allowable limit of 1% [71, 83, 84].

The internal presence of critical species such as chloride ions, sulfate ions, or potentially reactive aggregates (Fig. 9.2) overall in the concrete structural member makes the parent concrete decisive for the quality of the RCA [85] and it is of major concern for the quality of RCA. Several studies [86-88] reported reactive RCA, but they were also innocuous to alkali-silica reactions [82]. The extent of reactivity/expansion reached by a concrete member before its demolition will influence the extent of expansion that can be obtained with RCA produced from that concrete member. RCA produced from concretes that have suffered from a high degree of reactivity/expansion/damage can suffer less expansion compared to a similar proportion of unreacted aggregate material of the same origin. This is likely due to the consumption of reactive phases in the RCA; also, it is possible that the residual mortar that surrounds parts of

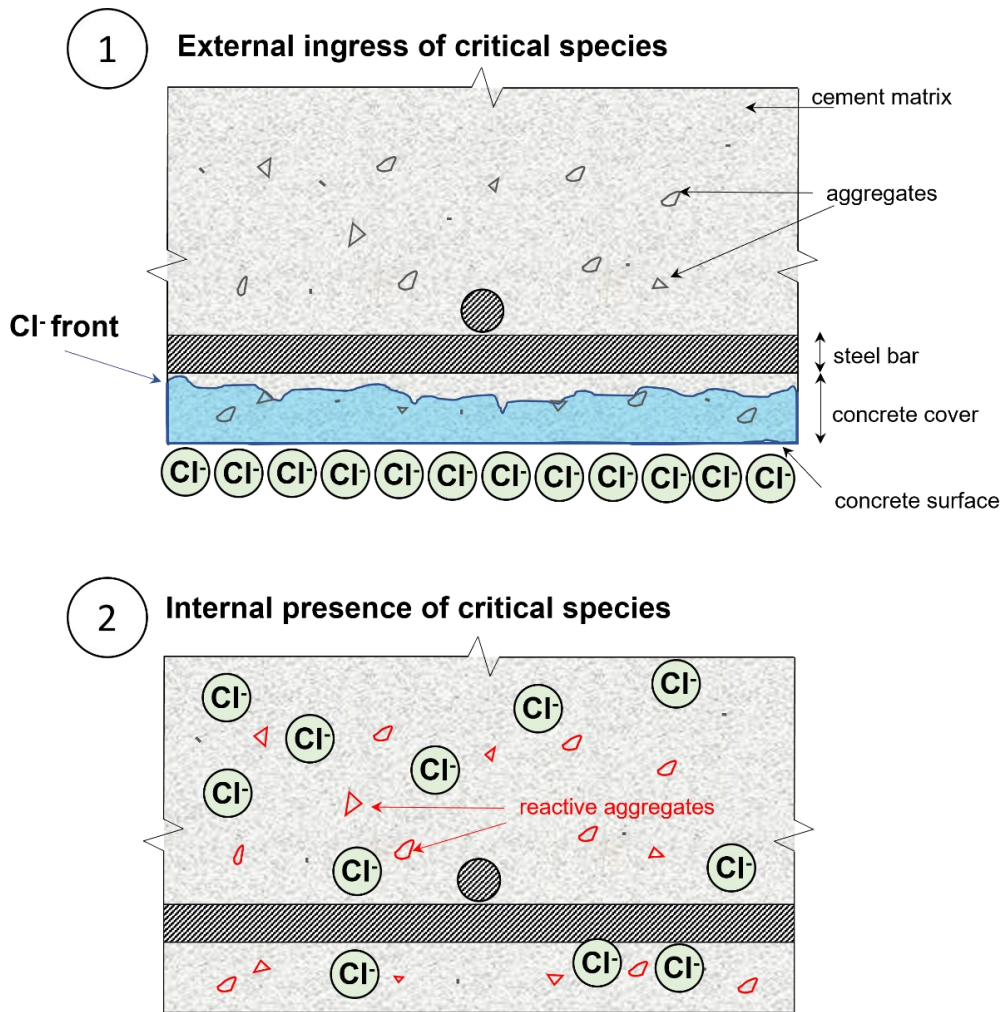


Fig. 9. Contamination of parent concrete caused by 1) external ingress of critical species such as chloride ions being mainly limited to the concrete cover, and 2) internal presence of critical species such as chloride ions or potentially reactive aggregates overall the concrete structure

reactive particles limits the exposure of the original aggregate to the concrete pore solution, thus reducing further reaction [85]. On the other hand, recycling/crushing of concrete incorporating some reactive aggregate materials can also rejuvenate the reactivity of the original aggregate by exposing reactive silica from fresh aggregate surfaces, thus resulting in a higher expansion of concrete incorporating such RCA compared to “stabilized” original gravel material [85].

To ensure that RCA are not a potential internal source of contaminants for new concrete, selective demolition is required. It would also decrease the number of tests that such aggregates need to pass in order to be used in new concrete. according to EN 12620:2002+A1:2008.

3.5 Characteristic quality indicators

To enable the use of RCA as European Standard EN 12620:2002+A1:2008 [89]-conforming products, it is necessary to test the parent concrete quality of each concrete member of a structure before demolition. The characteristic quality indicators are crucial for a comparative

assessment of various types of concrete. Criteria for selecting characteristic quality indicators for parent concrete testing and sorting were as follows: Literature review in Sections 3.1–3.4 and relevance of an indicator to the production and classification of RCA, available techniques to assess certain concrete properties in situ, robustness of the testing, automation capability, process speed, relevance of a quality indicator to a recycler. Quality indicators that are technically feasible to be assessed on concrete structures before demolition are surface visual inspection for deterioration and measurement of parent concrete strength and composition. These are three key characteristic quality indicators that can be linked to properties of RCA and their production, such as energy consumption during crushing, strength and type of cement and aggregates used in parent concrete, and potential alkali silica reactivity. The properties of parent concrete help determine which parts of the concrete structure can be recycled together and which parts should be kept separate to obtain concrete batches of known and consistent quality.

4 Workflow toward more rational concrete waste management

Selective demolition of concrete structures should involve a detailed plan and a workflow. The specific workflow is presented on an example of the concrete bridge in Fig. 10, where different parts of the bridge are sorted using characteristic quality indicators and the concrete is characterized before it is demolished and recycled. Recyclers can have the opportunity to select concrete with properties that best suit their crushing technology and business model. After recycling concrete members of known origin and quality, an advanced classification of recycled materials can be made in separate stockpiles: recycled

concrete aggregates from high-strength concrete without contamination (stockpile 1), recycled concrete aggregates from normal-strength concrete without contamination (stockpile 2), recycled concrete aggregates from lightweight aggregate concrete (stockpile 3) without contamination, and others (recycled concrete aggregates from contaminated concrete). Finally, the individual stockpiles will benefit the concrete producers, as their origin and quality will be known upon delivery. For efficient concrete sorting, testing of parent concrete quality would be essential. The following section presents guideline for non-destructive testing of concrete properties which are critical for concrete sorting before demolition.

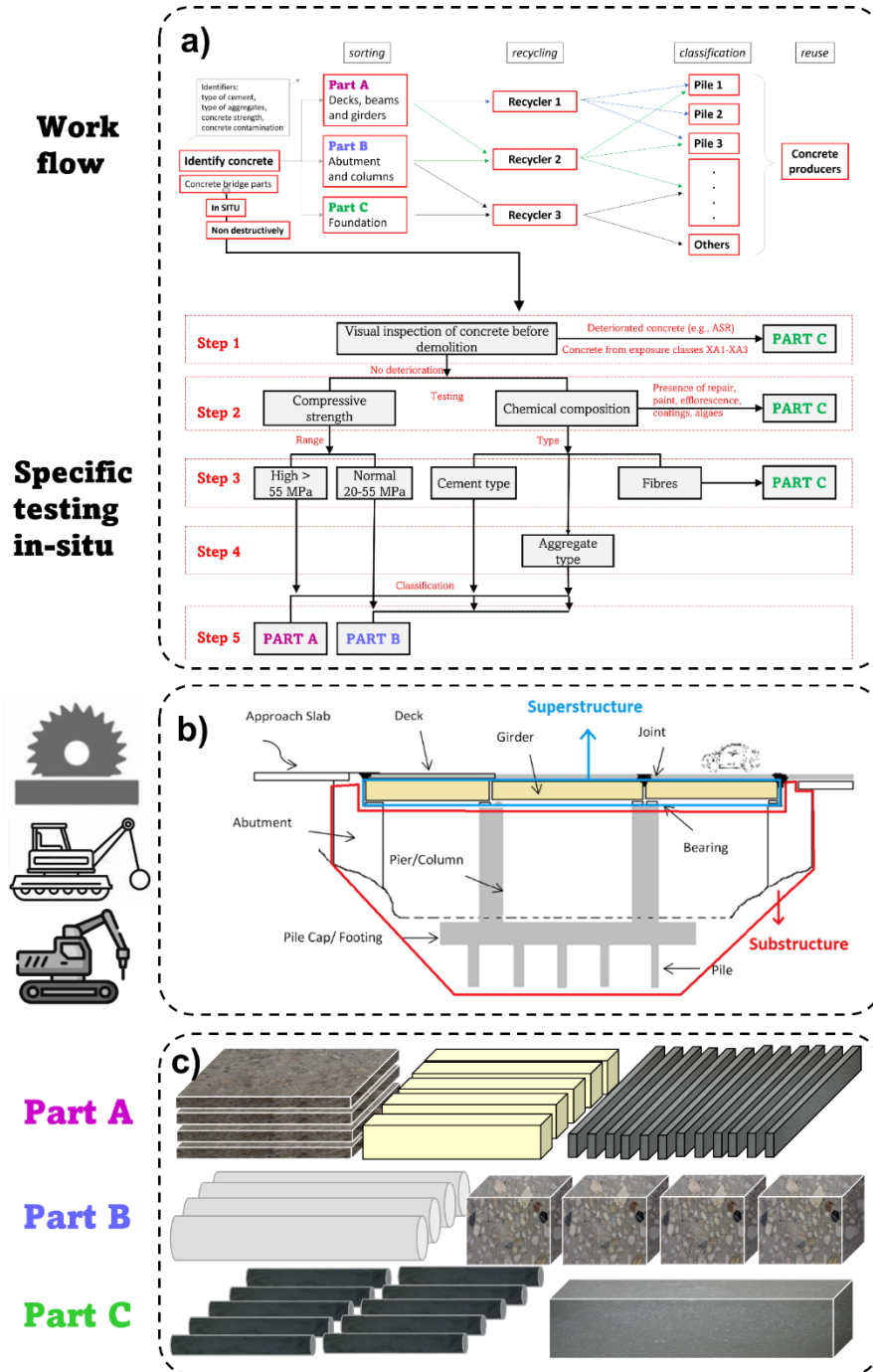


Fig. 10a) Workflow to implement in demolition projects, including specific in-situ testing and classification of concrete members based on strength and composition, b) an example of concrete bridge parts, c) their sorting prior to recycling and classification of concrete members based on a), (Bridge drawing adopted from [90])

5 In-situ testing of concrete properties

5.1 Compressive strength of concrete

The destructive testing requires the extraction of a concrete sample from the structure, which is then analysed in a laboratory. The extraction of such samples tends to be laborious and time consuming. Compared with destructive testing, non-destructive testing offers a promising way towards strength assessment since many non-destructive testing parameters are sensitive to material strength variations [91], and non-destructive testing can be deployed at many locations in real time at construction sites [92, 93]. The rebound hammer and ultrasonic pulse velocity tests are the most commonly used non-destructive methods for in situ concrete strength evaluation. The review of factors affecting the reliability of assessing the concrete strength by rebound hammer and cores [94] outlined the following sources of uncertainty: measurement uncertainties [95], strength variability [96], model uncertainties [96], statistical uncertainties of sampling [97], and influence of uncontrolled factors such as concrete degree of saturation and carbonation [91, 98, 99]. The standard EN 12504-2:2021 [100] specifies the method for determining the rebound index, whereas EN 12504-4:2021 [101] specifies the method for determining the ultrasonic pulse velocity, and EN 13791:2019 [99] summarizes guidance for the assessment of the in situ concrete compressive strength in structures. RILEM TC249-ISC also provides recommendations on non-destructive in situ strength assessment of concrete [102, 103]. It is generally stated that the rebound hardness tests of concrete are not intended as an alternative to the compressive strength testing, but with suitable correlation, they can provide an estimate of the in situ strength, which may be sufficient for the purpose of selective demolition. Nevertheless, in the case of selective demolition, non-destructive strength measurements can be verified, i.e., calibrated with results obtained on a discrete number of samples (cores) taken from the structure and tested in the laboratory, which is a common practice. Since the advantages and disadvantages of concrete strength evaluation in situ are well documented in the literature, standards, and guidelines, the present paper is dedicated to a review of methods that can evaluate concrete chemical composition and contamination.

5.2 Concrete chemical composition and contamination assessment

For determining the chemical composition and contamination type of concrete, only a few methods are available. Most of these techniques are destructive, requiring the extraction of a concrete sample from the structure, which is then analysed in a laboratory for mineralogical composition [104] with optical and electron microscopes. The extraction of such samples tends to be laborious and time-consuming. In the next paragraphs, the non-destructive testing methods are presented.

5.2.1 Visual inspection of concrete surface

Visual inspection is one of the most useful and versatile non-destructive techniques, and it is normally undertaken at the initial phase when assessing concrete deterioration by fire and alkali silica reaction. In spite of visual inspection being simple in principle, it may provide core information about the condition of the deteriorated structure and act as a

basis upon which subsequent assessment methods can be performed [105]. Visually apparent deterioration induced by heating includes spalling, cracking, surface crazing, deflection, colour changes, and smoke deterioration; attack by acids and alkalis includes exposed cement paste completely disintegrating together with any calcareous aggregate; ASR includes, among others, cracks (map cracking) and secondary deposits of alkali-silica gel that may appear on the outer concrete surface [106]. These indicators of deteriorated concrete can be assessed visually and further assessed using more advanced methods. A visual inspection of a concrete surface can lead to the immediate classification of a concrete member due to characteristic signs of concrete deterioration. This can be the first line of concrete quality assessment. In the case of non-deteriorated concrete, it is necessary to employ element-characterization techniques for the determination of the chemical composition of the concrete to assess its classification and future application of RCA.

5.2.2 Analysis of concrete composition with a handheld X-Ray Fluorescence Analyzer

State-of-the art techniques relevant to in-situ measurements for determining the material element composition non-destructively, are handheld laser-induced breakdown spectroscopy (hLIBS) and handheld X-Ray fluorescence (hXRF) analyzers. In general, a single LIBS spectrum can be obtained in a fraction of a second, whereas typically tens of seconds to minutes are needed to acquire an XRF spectrum [107]. However, XRF is a non-destructive technique, whereas LIBS is micro-destructive, as each laser shot removes a few nanograms of material from the sample surface, forming a surface crater. Thus, a LIBS analysis of a particular spot on a sample cannot be repeated and cannot be compared to other techniques, which represents a drawback for LIBS [107]. In laboratories, conventional desktop XRF has been one of the most widely used spectroscopic methods for testing the element composition of materials for decades. The hXRF brought a large revolution to the field of chemical materials characterization. Based on previous experience with concrete bulk composition testing with desktop XRF, the hXRF is particularly promising for studying concrete composition in situ. In the field of concrete science, typical desktop XRF is widely applied for the characterization of raw materials used for concrete production, including RCA in powder form. Moreover, the standard EN 196-2: 2014 [108] presents XRF as a method for cement composition testing in laboratories.

The hXRF possesses many advantages, including easy of use, non-destructive testing, the portability (for fieldwork), fast results, large numbers of analysed spots, satisfactory accuracy, and precision [109]. It therefore has a wide application foreground in material science, such as rocks, ores, metals, soil, ceramics, manufactured glass, geoarchaeology, art, and paintings [110-114]. A recent study [115] has shown promising results regarding in situ versus laboratory characterization of historical structures in marine environments using hXRF. hXRF-based methods have been used for the in situ characterization of concrete pavements [116], concrete from nuclear material processing, and liquid waste systems [117]. hXRF readings can also be used to estimate the percentages of sand, silt, and clay in the soil [118].

Fig. 11 shows the working mechanism. An hXRF analyser includes an X-ray source, which irradiates the sample, and an X-ray detector, for detecting the X-ray

fluorescence emitted by the sample in response to the irradiation. Each element in the sample emits X-ray fluorescence in energy bands that are characteristic of the element. The detected X-ray fluorescence is analysed to find the energies, or equivalently, the wavelengths of the detected photons, and the qualitative and/or quantitative composition of the sample is determined based on this analysis [119]. A mixture of elements irradiated by a sufficiently energetic X-ray beam absorbs the incident X-rays and re-emits other X-rays, the wavelengths of which are characteristic of the elements in the sample, and the intensities of which may be correlated with their concentrations [120]. Elements from magnesium to uranium are within the detection limit and can be analysed [121]. The device is equipped with a small screen that shows the results instantly, once the device is calibrated for the specific materials (Fig. 12). The measurement times are very short, such that it is possible to collect data for up to 100 samples in a single day [109].

Regarding concrete in situ identification in the context of sorting and selective demolition based on composition, hXRF is believed to be a key solution to this issue owing to

its compatibility with lab XRF (Table 2) for concrete characterization, easy installation, maintenance, and large-scale applications. Furthermore, because hXRF can perform non-destructive analysis with minimal sample preparation, it is ideal for in situ concrete structural members. Moreover, hXRF is largely used in the mining and cement industries and can detect a large range of elements characteristic of concrete. However, the hXRF-based method has yet to be studied and applied for determining the chemical element composition of in situ concrete structures. Therefore, hXRF is recommended for a laboratory proof-of-concept to identify and quantify elements in various types of concrete and, therefore, various used cement and aggregate types for the concrete demolition concept. In comparison to destructive, time-consuming, and relatively expensive techniques for concrete characterization in situ, hXRF can be generally applied as a first approach to estimate concrete chemical composition in situ. This would be helpful for ensuring the identification of concrete at the source, improving the demolition efficiency, guiding the quality of recycled concrete, and decreasing the number of standard chemical tests in the laboratory.

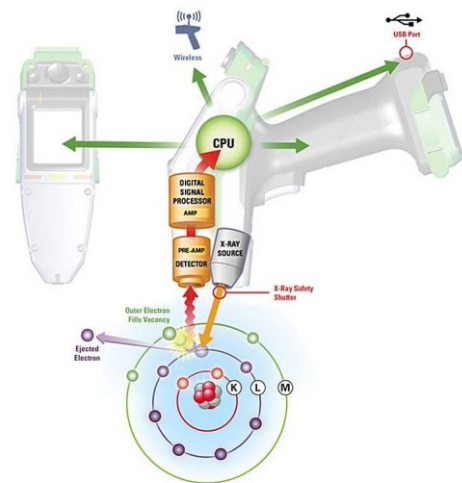


Fig. 11. The X-ray instrument emits energy which changes the electrons orbitals [122]



Fig. 12. The use of hXRF BRUKER device

Table 2. A general comparison between conventional desktop XRF (BRUKER S2 PUMA Series 2) and BRUKER Handheld XRF (S1 TITAN 800) instrument settings

Settings	Conventional desktop XRF (S2 PUMA Series 2)	Handheld XRF (S1 TITAN 800)
Range of detectable elements	Na–Am C–Am with light element (LE) detector	Mg–U
X-Ray tube Anode	Pd or Ag anode	Rh anode
Excitation source	4000 W (50 kV, 2000µA)	4W (50 kV, 200 µA)
X-ray beam path	Vacuum, Air, Helium, Nitrogen	Air (1 bar)
Spot size	1–34 mm	3–8 mm
Filter	10–position automatic filter changer	5–position automatic filter changer
Sample type	Loose powders, granules, solids, pressed pellets, fused beads, and liquids	Loose powders, granules, solids, pressed pellets, fused beads
Sample preparation	Drying	No preparation needed
Scan duration	6–30 s	30 s –10 min
Working distance	contact measurement	contact measurement

6 Further research on hXRF for concrete

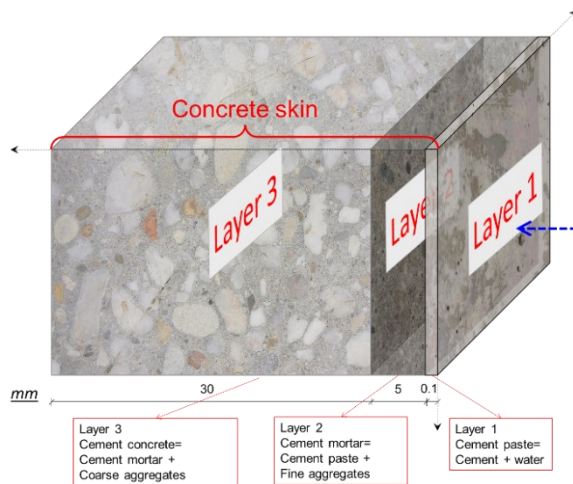
6.1 Parameters affecting measurements

There are several influential parameters that need attention for hXRF measurements:

- Distinction between cement and aggregates.

Because the spot size of the hXRF aperture varies between 3 and 8 mm depending on the device, the heterogeneity of the tested material can have a significant impact on the results [121]. When testing the chemical composition of hardened concrete, the challenge lies in recognizing cement paste, fine and coarse aggregates due to partial overlap in particle size distribution and, in some cases, similar element oxides.

Kreijger [123] showed that the skin of a concrete structure consists of three layers, the cement skin (~0.1 mm thick), the mortar skin (~5 mm) and the concrete skin (~30 mm), as shown in Fig. 13. Therefore, it is hypothesized that testing the chemical composition of the surface (first concrete skin layer) will represent the cement type, while testing the chemical composition of the inner layers will yield aggregate types in a relatively homogeneous environmental setting and therefore can be predicted from the direct element readings of hXRF.



- X-ray beam path, air versus vacuum.

Conventional XRF works in a vacuum, while hXRF operates in air. The question is, what effect does air have on hXRF measurements when compared to measurements in vacuum? A Bruker S1-Titan 600 hXRF analyser with a patented compact collimating device [124] has been used for evaluation of the effect of environmental interferences (specifically in the low energy range up to 10 keV) on the graphite, copper, SiO₂ powder, and UO₂. First, the authors used Monte Carlo simulation to calculate the relative intensity of X-ray energy on the surface in both vacuum and air [125]. The former represents the X-rays immediately after emission from the Rh target, while the latter represents reflection of the X-rays by air between the hXRF and the contact surface of the sample. At higher energy levels hardly any difference can be seen (Fig. 14). Second, in the case of graphite, the effect of the environmental interferences was evaluated to be about 20% on the conformity of the measured and simulated results, while those for copper, SiO₂, and UO₂ were about 1%, 3%, and less than 1%, respectively. These results indicate that samples having elements with higher rates of photoelectric absorption followed by fluorescence compared to scattering tend to decrease the effect of the environmental interferences over the entire spectrum.



Fig. 13. Characterization of the concrete skin. Credits go to Rijkswaterstaat for the photo of the concrete structure on the right

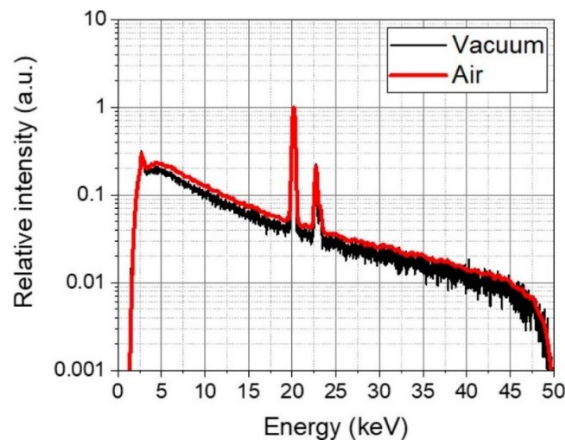


Fig. 14. Monte Carlo N-Particle Transport 6 (MCNP6) simulation of a primary X-ray beam source profile in vacuum and air media [125]. The accelerating voltage is 50 kV

- Filters

hXRF has the possibility of using multiple filters. Filters are used to reduce the intensity of interfering lines and background, and hence improve the signal-to-noise ratio. Normally, background scatter is lower in the vacuum condition, which significantly improves resolution. Filters are placed between the source and the sample (Fig. 15). Commonly used filter materials are aluminium and brass with a thickness between 100 and 1000 μm , depending on the tube lines that have to be filtered out. Fig. 16 shows the effect of different filters implemented in the M4 TORNADO ED-XRF spectrometer on the chemical composition of a historical mortar [115]. The signal on the cementitious mortar was best when no filter was used. This should be considered when testing concrete surfaces.

- Sample preparation.

It is common practice to analyse powders with a conventional desktop XRF analyser. Powdering is a good way to counter mineralogical heterogeneity and is the main justification for sample preparation. If solid flat surfaces are used in geoarchaeology and tested with hXRF, the difference between those and the powdered samples is within counting errors, but not for some heavy elements such as Ti and Fe [109]. In general, there is no gain in instrumental precision by analysing powders instead of unprepared rock cores [127].

Among the correctible elements, three groups can be proposed with regards to the accuracy of hXRF measurements on rock cores versus powders: the elements or oxides better determined on rock cores, those better determined on powders, and those that show similar results (Fig. 17) [127]. This suggests that when measuring concrete surface composition, powdering should be investigated to demonstrate whether the testing of solid surface and powdered surface provides similar results and whether all concrete elements are acceptable in both media.

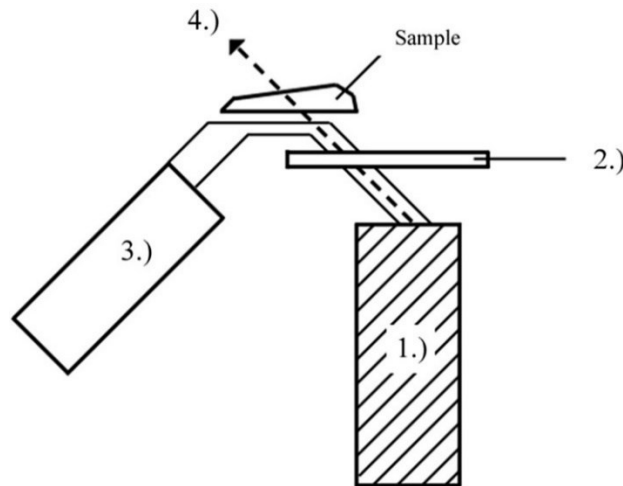


Fig. 15. Scheme of hXRF, including: (1) X-ray source (rhodium tube); (2) filter (6 mil Cu, 1 mil Ti, 12 mil Al); (3) detector; as well as (4) beam path at 45°angle, adopted from [126]

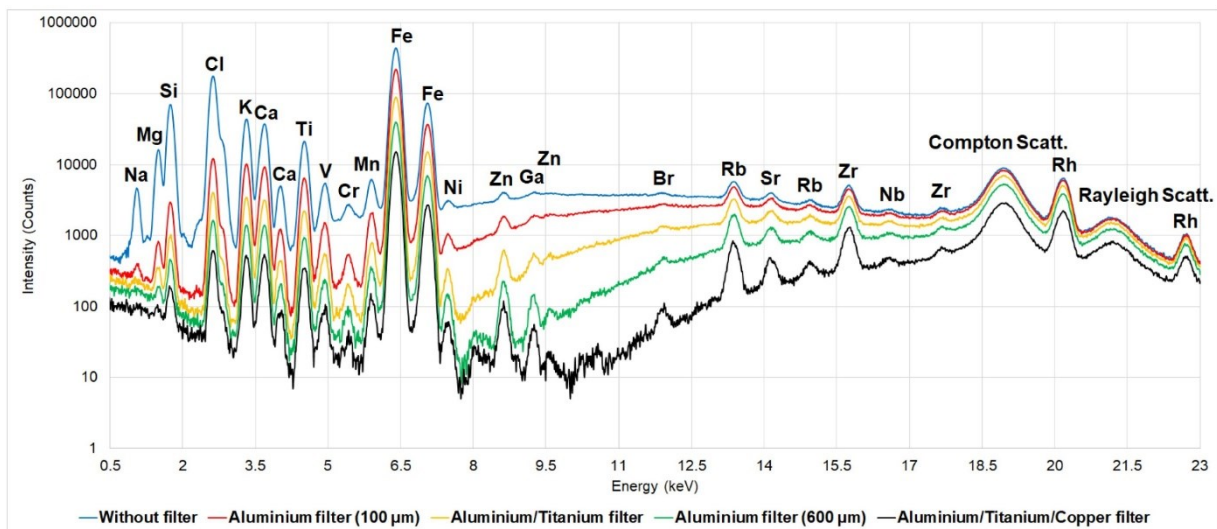


Fig. 16. A comparison of detection power using different filters implemented in the M4 TORNADO ED-XRF spectrometer applied to a historical mortar as an example of signal improvement [115]

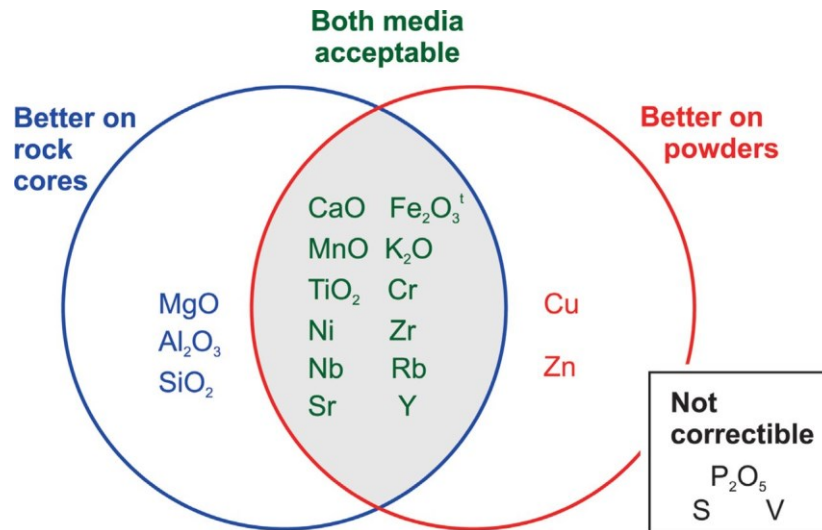


Fig. 17. A Venn diagram represents the three groups of correctible elements: (1) elements better determined in situ on rock cores with respect to accuracy, (2) elements better determined on powders and (3) elements showing similar results regardless of the media. The diagram also shows the elements that are detected but not correctible. The following elements and oxides are determined in mining plus mode for best results: Al_2O_3 , CaO , Fe_2O_3 , MgO , MnO , Ni , SiO_2 , and Zr . The following elements and oxides are determined in soil mode for best results: Cr , K_2O , Nb , Rb , Sb , TiO_2 and Y . Adopted from [127]

- Concrete surface roughness.

Surface irregularities (e.g., pores, voids, cracks) on rough surfaces or in the middle layers of concrete (Figs. 18, 19) have the potential to store measurements. Particularly, moisture and air are retained in these irregularities. Thus, attention should be given to the sample preparation to find the optimal surface roughness and moisture for the contacting surfaces to achieve optimal performance of the hXRF measurements (avoiding air gaps and contact with water). Pretreatments such as grinding and polishing,

significantly smooth the concrete surface, but they also may create different micrometer-sized irregularities. Thus, grinding, even if performed carefully, creates various irregularities of different shapes (such as scratches) that are produced by the abrasive particles in the grinding paper. The homogeneity of the microstructure, the level of purity, the size and distribution of aggregate particles, and other hard constituents (e.g., fibres) in the concrete matrix are the parameters that may influence the results.

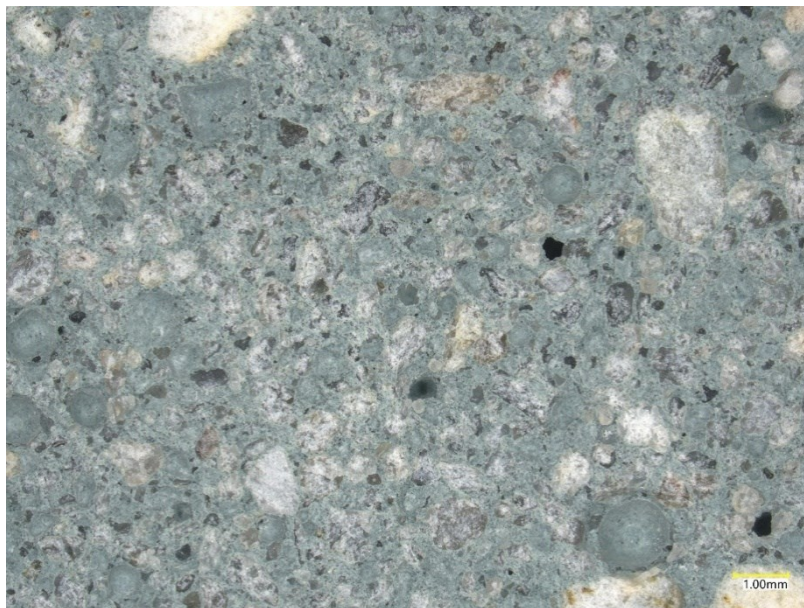


Fig. 18. Concrete middle section topography (measured by focus variation microscopy 20 \times , lateral resolution: 2 μ m, vertical resolution: 50 nm)

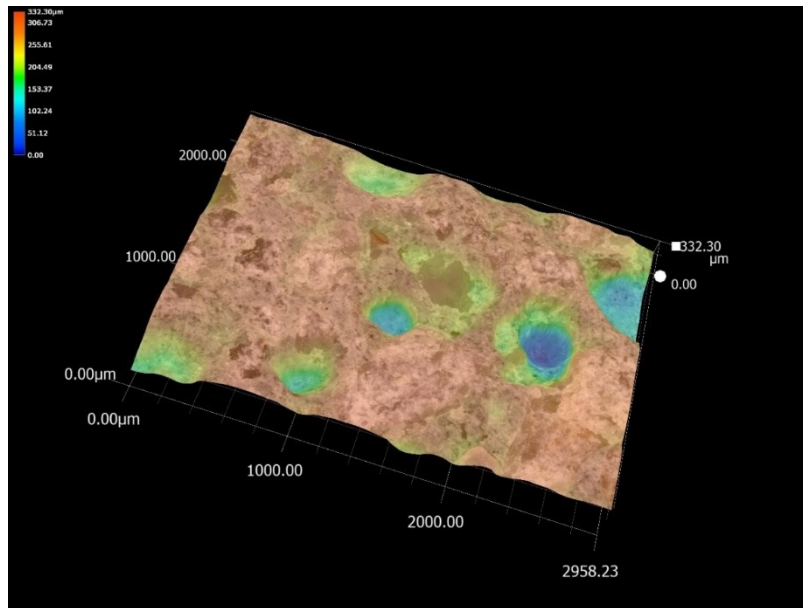


Fig. 19. Three-dimensional height profiles of the concrete middle section (concrete middle section appearance is presented in Fig. 18.)

- Low concentration elements detection.

Regarding concrete contamination such as Cl and S, for their largely lower concentrations compared to, for instance, CaO or SiO₂, a hXRF instrument may incorporate a calcium or lead-anode X-ray tube such as that used by Cesareo et al. [128] to determine Cl and S in frescoes and stone monuments. The detection limits were reported to be 0.04% m/m for Cl and 0.03% m/m for S.

- Validation techniques.

Petrography and the method of extracting elements with acids and then analyzing them with the inductively coupled plasma (ICP) technique are two destructive methods that can be used to study the composition of concrete. In addition, conventional XRF and Energy-dispersive X-ray Spectroscopy (EDS) may be used for the validation of hXRF results.

6.2 Algorithms to automate the characterization and selective demolition of concrete structures

With the rapid advances in data science concerning the easier manipulation of large datasets (big data), the development of machine learning regression models, the increasing use of building information modelling (BIM), digital twins, and the Internet of Things (IoT), significant benefits can be gained by the application of these methods to automating the characterization of concrete as well as the selective demolition of structures.

For instance, an advanced terrestrial laser scanning (TLS)-based method automates the classification of rebar diameters using machine learning in order to enable accurate rebar spacing inspection [129]. In this method, a new methodology named Density based Modelling (DBM) is proposed to improve classification accuracy. Experimental tests on laboratory specimens with rebars of seven different diameters (D10–D40) were conducted, and the results show that the prediction accuracy for the large rebar diameter

group (D25–D40) was up to 97.2%. However, it was found that its performance in predicting small rebar diameter groups (D10–D20) is much lower – around 56.0% [129].

Using data from both ground-penetrating radar (GPR) and electromagnetic induction (EMI), [130] a strategy based on deep learning is used to figure out the cover thickness and diameter of steel bars in reinforced concrete structures. The proposed framework is made up of two parts: 1) finding hyperbolic signals in radargrams, and 2) figuring out the diameter of reinforcement bars and the thickness of the cover.

Non-destructive detection of steel reinforcement corrosion in concrete structures has been achieved using techniques such as ground penetrating radar [131]. Current inspection practices require a large amount of time for inspection and can pose a safety risk to inspectors. These drawbacks could be overcome by using ground robotic systems [131]. Furthermore, work is being conducted on the enrichment of Industry Foundation Classes (IFC) in BIM with data on damage and deterioration [132].

Finally, such technologies should preferably lead to BIM-based frameworks and databanks of material stock for reusing recycled materials and entire structural members [133]. Efforts are already under way to develop BIM models of high level of development (LOD) enriched with data on the static, mechanical, and reuse properties of the built materials and members. From such models merged with LCA and multi-criteria decision-making tools and embedded in city-wide platforms of building stock data, the concepts of „design from stock“ and „design with stock“ can successfully emerge [133] leading to a fully circular construction industry.

7 Conclusions

The various recycling technologies for concrete waste have greatly contributed to increasing the sustainability of waste management. However, mixed concrete streams are becoming more prevalent, and the quality of RCA is uncertain. Advanced solutions for recycling technology cannot address the quality issues of input concrete waste.

Therefore, a new workflow toward a more rational CDW management and the selective demolition of concrete structures in relation to concrete type characterization, is presented in this paper. Knowing the origin of RCA should aid in improving predictions of the impact of their use on the properties of new concrete by separating aggregate stockpiles based on parent concrete properties.

This paper proposes a specific workflow to be implemented in demolition projects for parent concrete origin and quality identification before concrete structure demolition. Compressive strength, chemical composition, and contamination are selected for characteristic quality indicators and concrete classification. Parent concrete strength determines the physical and mechanical properties of RCA, such as energy of crushing and strength. The parent concrete composition can ensure that RCA have the appropriate application (aggregates, mineral addition for clinker manufacturing, pozzolanic material, filler). Contamination evaluation can ensure that the contaminated concrete is kept apart. Non-destructive testing methods are proposed to estimate the quality of the concrete before demolition. A hXRF analyser could potentially be used for concrete composition measurements in situ. hXRF should be considered a preliminary screening tool for concrete quality selection and not a substitute for conventional chemical methods (e.g., desktop XRF, fusion ICP-ES and ICP-MS). The hXRF possesses many advantages, including non-destructive testing, large numbers of analysed spots, high sensitivity, compatibility with lab techniques for material characterization, and easy installation and maintenance. Further research is dedicated to the laboratory proof of a proposed characterization approach for concrete quality assessment.

Considering the above presented evidence, it can be concluded that the practical application of non-destructive concrete characterization for the purposes of selective demolition can significantly increase the sustainability of the construction industry, unlocking a huge potential for optimized material recovery and reuse and contributing greatly to a fully circular construction sector.

Acknowledgements

The first author acknowledges funding provided by the Dutch Ministry of Infrastructure and Water Management (Rijkswaterstaat), SKKB, and in-kind contributions from Scientific Benelux (BRUKER) and Proceq. Special thanks to Wim Ekkelenkamp, Erik Hoven, and Peter Broere for valuable discussions related to concrete demolition and recycling. Student Abdellah Hussein is acknowledged for his insights on the topic of concrete demolition.

References

- [1] Global Material Resources Outlook to 2060 Economic Drivers and Environmental Consequences, (2019) OECD publishing.
- [2] M. Longo, A. Sánchez Rodríguez, Á. S. López Marroquín, A. J. Domínguez, Ó. Bouzas Rodríguez, P. Sanecka, C. Marchiori, M. Rigotti, Review of methodologies and instruments for diagnostics of transport infrastructure, IM-SAFE-Project (2022).
- [3] P. V. Sáez, M. Osmani, A diagnosis of construction and demolition waste generation and recovery practice in the European Union, *J. Cleaner Prod.* 241 (2019), 118400. 10.1016/j.jclepro.2019.118400
- [4] G. Cai, D. Waldmann, A material and component bank to facilitate material recycling and component reuse for a sustainable construction: Concept and preliminary study. *Clean Technol. Environ. Policy* 21(10) (2019) 2015-2032. 10.1007/s10098-019-01758-1
- [5] J. L. Gálvez-Martos, D. Styles, H. Schoenberger, B. Zeschmar-Lahl, Construction and demolition waste best management practice in Europe. *Resour. Conserv. Recycl.* 136 (2018)166-178. 10.1016/j.resconrec.2018.04.016
- [6] C. Zhang, M. Hu, X. Yang, B. Miranda-Xicotencatl, B. Sprecher, F. Di Maio, X. Zhong, A. Tukker, Upgrading construction and demolition waste management from downcycling to recycling in the Netherlands, *J. Cleaner Prod.* 266 (2020) 121718. 10.1016/j.jclepro.2020.121718
- [7] M.H. Faber, Risk and safety in civil engineering, 2007.
- [8] P. Bazant, Q. Yu, G. H. Li, Excessive long-time deflections of prestressed box girders. I: Record-span bridge in Palau and other paradigms, *J. Struct. Eng. ASCE* 138(6) (2012). 10.1061/(ASCE)ST.1943-541X.0000487
- [9] RWS Grote Projecten en Onderhoud, Sloopoorzaken bruggen en viaducten in en over rijkswegen, Iv-Infra b.v. 2016.
- [10] A1: vervanging viaduct Hoog Burel. Available from: <https://www.rijkswaterstaat.nl/wegen/projectenoverzicht/a1-vervanging-viaduct-hoog-burel>.
- [11] F. Tomosawa, T. Noguchi, M. Tamura, The way concrete recycling should be, *J. Adv. Concr. Technol.* 3(1)(2005) 3-16. <https://doi.org/10.3151/jact.3.3>
- [12] European Commission, 'Com/2020/98 Final - Communication from the Commission to the European Parliament, the Council, the European Economic and Social Committee and the Committee of Regions: A New Circular Economy Action Plan for a Cleaner and More Competitive Europe', (2020).
- [13] EU-DIRECTIVE-2008/98/EC of the European Parliament and the Council of 19 November 2008 on Waste and Repealing Certain Directives, Official Journal of the European Union, 2008.
- [14] EU-DIRECTIVE-2018/851/EC of the European Parliament and of the Council of 30 May 2018 Amending Directive 2008/98/EC on Waste, European Union: Official Journal of the European Union, 2018.
- [15] Ecorys, EU Construction & Demolition Waste Management Protocol. 2016, European Commission Brussels, Belgium.
- [16] Commission, E., Guidelines for the Waste Audits before Demolition and Renovation Works of Buildings. 2018, European Commission Brussels, Belgium.
- [17] E. Khoury, W. Ambrós, B. Cazacliu, C. H. Sampaio, S. Remond, Heterogeneity of recycled concrete aggregates, an intrinsic variability, *Constr. Build. Mater.* 175 (2018) 705-713. <https://doi.org/10.1016/j.conbuildmat.2018.04.163>
- [18] M. Pepe, T. M. Grabois, M. A. Silva, L. M. Tavares, R. D. Toledo Filho, Mechanical behaviour of coarse, lightweight, recycled and natural aggregates for concrete, *Proceedings of the Institution of Civil Engineers-Construction Materials*, 173(2)(2020) 70-78. <https://doi.org/10.1680/jcoma.17.00081>.

- [19] N.Tošić, S.Marinković, I.Ignjatović, A database on flexural and shear strength of reinforced recycled aggregate concrete beams and comparison to Eurocode 2 predictions, *Constr. Build. Mater.* 127 (2016) 932-944. <https://doi.org/10.1016/j.conbuildmat.2016.10.058>
- [20] M. Nedeljković, J. Visser, B. Šavija, S. Valcke, E. Schlangen, Use of fine recycled concrete aggregates in concrete: A critical review, *J. Build. Eng.* 38 (2021) 102196. [10.1016/j.jobe.2021.102196](https://doi.org/10.1016/j.jobe.2021.102196).
- [21] J. Pacheco, J. de Brito, Recycled Aggregates Produced from Construction and Demolition Waste for Structural Concrete: Constituents, Properties and Production, *Materials*, 14(19) (2021) 5748. [10.3390/ma14195748](https://doi.org/10.3390/ma14195748)
- [22] N. Roussat, C. Dujet, J. Méhu, Choosing a sustainable demolition waste management strategy using multicriteria decision analysis, *Waste Manage.* 29(1) (2009)12-20. [10.1016/j.wasman.2008.04.010](https://doi.org/10.1016/j.wasman.2008.04.010).
- [23] <https://zenrobotics.com/solutions/heavy-picker/#>.
- [24] M. Alexander and S. Mindess, *Aggregates in concrete (Modern concrete technology)* 2005, Spon Press, London.
- [25] M. V. A. Florea, H. J. H. Brouwers, Properties of various size fractions of crushed concrete related to process conditions and re-use, *Cem. Concr. Res.* 52 (2013) 11-21. [10.1016/j.cemconres.2013.05.005](https://doi.org/10.1016/j.cemconres.2013.05.005).
- [26] K.J. Schenk, Patent No. WO 2011/142663 (2011), The Netherlands.
- [27] S. Lotfi, J. Deja, P. Rem, R. Mróz, E. van Roekel, H. van der Stelt, Mechanical recycling of EOL concrete into high-grade aggregates, *Resour. Conserv. Recycl.* 87 (2014) 117-125. [10.1016/j.resconrec.2014.03.010](https://doi.org/10.1016/j.resconrec.2014.03.010).
- [28] M. Quattrone, S. C. Angulo, V. M. John, Energy and CO₂ from high performance recycled aggregate production, *Resour. Conserv. Recycl.*, 90 (2014) 21-33. [10.1016/j.resconrec.2014.06.003](https://doi.org/10.1016/j.resconrec.2014.06.003).
- [29] N. Tošić, J. M. Torrenti, T. Sedran, I. Ignjatović, Toward a codified design of recycled aggregate concrete structures: Background for the new fib Model Code 2020 and Eurocode 2, *Structural Concrete*, 22(5) (2021) 2916-2938. <https://doi.org/10.1002/suco.202000512>.
- [30] C.F.Hendriks and H. Pietersen, Report 22: SUSTAINABLE raw materials: construction and demolition waste—state-of-the-art report of RILEM technical committee 165-SRM. Vol. 22. 2000: RILEM publications.
- [31] A. Di Maria, J. Eyckmans, K. Van Acker, Downcycling versus recycling of construction and demolition waste: Combining LCA and LCC to support sustainable policy making, *Waste Manage.* 75 (2018), 3-21. <https://doi.org/10.1177/0734242X16657605>.
- [32] S. H. Ghaffar, M. Burman, N. Braimah. Pathways to circular construction: An integrated management of construction and demolition waste for resource recovery. *J. Cleaner Prod.*, 244 (2020), 118710, [10.1016/j.jclepro.2019.118710](https://doi.org/10.1016/j.jclepro.2019.118710)
- [33] M. Rašković, A. M. Ragossnig, K. Kondracki, M. Ragossnig-Angst, Clean construction and demolition waste material cycles through optimised pre-demolition waste audit documentation: A review on building material assessment tools, *Waste Manage. Res.* 38(9) (2020) 923-941. <https://doi.org/10.1177/0734242X209367>.
- [34] R. V. Silva, J. De Brito, R. K. Dhir, Properties and composition of recycled aggregates from construction and demolition waste suitable for concrete production, *Constr. Build. Mater.* 65(2014)201-217. [10.1016/j.conbuildmat.2014.04.117](https://doi.org/10.1016/j.conbuildmat.2014.04.117)
- [35] S. C. Kou, C. S. Poon, Effect of the quality of parent concrete on the properties of high performance recycled aggregate concrete, *Constr. Build. Mater.* 77 (2015) 501-508, [10.1016/j.conbuildmat.2014.12.035](https://doi.org/10.1016/j.conbuildmat.2014.12.035)
- [36] M.Nedeljković, A. Mylonas, V. Wiktor, E. Schlangen, J. Visser, Influence of sand drying and mixing sequence on the performance of mortars with fine recycled concrete aggregates, *Constr. Build. Mater.* 315(2022) 125750. <https://doi.org/10.1016/j.conbuildmat.2021.125750>.
- [37] A. Mylonas, Experimental investigation of concrete mixtures incorporating recycled concrete aggregates, MSc thesis (2021) Delft University of Technology, The Netherlands. <http://resolver.tudelft.nl/uuid:e0075d76-d0c9-4425-8214-9317303e8721>.
- [38] D. Carro-López, B. González-Fontebao, J. De Brito, F. Martínez-Abella, I. González-Taboada, P. Silva, Study of the rheology of self-compacting concrete with fine recycled concrete aggregates, *Constr. Build. Mater.* 96 (2015) 491-501. <https://doi.org/10.1016/j.conbuildmat.2015.08.091>
- [39] S. C. Kou, C. S. Poon, Properties of self-compacting concrete prepared with coarse and fine recycled concrete aggregates, *Cem. Concr. Compos.* 31(9)(2009) 622-627. <https://doi.org/10.1016/j.cemconcomp.2009.06.005>
- [40] I. S. Ignjatović, S. B. Marinković, N. Tošić, Shear behaviour of recycled aggregate concrete beams with and without shear reinforcement, *Eng. Struct.* 141(2017)386-401. <https://doi.org/10.1016/j.engstruct.2017.03.026>.
- [41] D. Pedro, J. De Brito, L. Evangelista, Influence of the use of recycled concrete aggregates from different sources on structural concrete, *Constr. Build. Mater.* 71 (2014) 141-151. <https://doi.org/10.1016/j.conbuildmat.2014.08.030>
- [42] S. Lotfi, C2CA Concrete Recycling Process, PhD thesis (2016) Delft University of Technology, The Netherlands. <https://doi.org/10.4233/uuid:70505a1f-c0d7-47c7-ab62-8d487761c021>
- [43] G. Andreu, E. Miren, Experimental analysis of properties of high performance recycled aggregate concrete, *Constr. Build. Mater.* 52(2014) 227-235. <https://doi.org/10.1016/j.conbuildmat.2013.11.054>
- [44] N. Tošić, S. Marinković, N. Pecić, I. Ignjatović, J. Dragaš, Long-term behaviour of reinforced beams made with natural or recycled aggregate concrete and high-volume fly ash concrete, *Constr. Build. Mater.* 176(2018) 344-358. <https://doi.org/10.1016/j.conbuildmat.2018.05.002>
- [45] S. Omary, E. Ghorbel, G. Wardeh, Relationships between recycled concrete aggregates characteristics and recycled aggregates concrete properties, *Constr. Build. Mater.* 108 (2016) 163-174, [10.1016/j.conbuildmat.2016.01.042](https://doi.org/10.1016/j.conbuildmat.2016.01.042).

- [46] M.Tavakoli, P.Soroushian, Strengths of recycled aggregate concrete made using field-demolished concrete as aggregate, *Materials Journal* 93(2) (1996) 178-181.
- [47] L.Evangelista, J. De Brito, Mechanical behaviour of concrete made with fine recycled concrete aggregates, *Cem. Concr. Compos.* 29(5)(2007) 397-401. <https://doi.org/10.1016/j.cemconcomp.2006.12.004>
- [48] S.Levy, P. Helène, Durability of concrete mixed with fine recycled aggregates, *Exacta*, 5(1) (2007) 25-34.
- [49] H.Yaprak, H. Y.Aruntas, I.Demir, O.Simsek, G.Durmus, Effects of the fine recycled concrete aggregates on the concrete properties. *International Journal of Physical Sciences*, 6(10)(2011) 2455-2461. <https://doi.org/10.5897/IJPS11.253>.
- [50] P. Pereira, L. Evangelista, J. De Brito, The effect of superplasticisers on the workability and compressive strength of concrete made with fine recycled concrete aggregates, *Constr. Build. Mater.* 28(1) (2012) 722-729. <https://doi.org/10.1016/j.conbuildmat.2011.10.050>.
- [51] A. G. Khoshkenari, P. Shafigh, M. Moghimi, H. B. Mahmud, The role of 0–2 mm fine recycled concrete aggregate on the compressive and splitting tensile strengths of recycled concrete aggregate concrete, *Mater. Des.* 64 (2014) 345-354. <https://doi.org/10.1016/j.matdes.2014.07.048>.
- [52] F. Cartuxo, J. De Brito, L. Evangelista, J. R. Jimenez, E. F. Ledesma, Rheological behaviour of concrete made with fine recycled concrete aggregates—Influence of the superplasticizer, *Constr. Build. Mater.* 89 (2015) 36-47. <https://doi.org/10.1016/j.conbuildmat.2015.03.119>.
- [53] F. Cartuxo, J. De Brito, L. Evangelista, J. R. Jiménez, E. F. Ledesma, Increased durability of concrete made with fine recycled concrete aggregates using superplasticizers, *Materials*, 9(2) (2016) 98. <https://doi.org/10.3390/ma9020098>.
- [54] J.A.Bogas, J. De Brito, D. Ramos, Freeze–thaw resistance of concrete produced with fine recycled concrete aggregates. *J. Cleaner Prod.* 115 (2016) 294-306. <https://doi.org/10.1016/j.jclepro.2015.12.065>.
- [55] L. Evangelista, J. De Brito, Flexural behaviour of reinforced concrete beams made with fine recycled concrete aggregates, *KSCE J. Civ. Eng.* 21(1) (2017) 353-363. <https://doi.org/10.1007/s12205-016-0653-8>.
- [56] L. Evangelista, J. De Brito, Durability of crushed fine recycled aggregate concrete assessed by permeability-related properties, *Mag. Concr. Res.* (2018) 1-9. <https://doi.org/10.1680/jmacr.18.00093>.
- [57] V.Radonjanin, M.Malešev, S.Marinković, A. E. S.Al Maly, Green recycled aggregate concrete, *Constr. Build. Mater.* 47(2013) 1503-1511. <https://doi.org/10.1016/j.conbuildmat.2013.06.076>
- [58] J.Thomas, N. N.Thaicavil, P. M.Wilson, Strength and durability of concrete containing recycled concrete aggregates, *J. Build. Eng.* 19(2018)349-365. <https://doi.org/10.1016/j.jobe.2018.05.007>.
- [59] Y.Geng, Q.Wang, Y. Wang, H.Zhang, Influence of service time of recycled coarse aggregate on the mechanical properties of recycled aggregate concrete. *Mater. Struct.* 52(5) (2019) 1-16. <https://doi.org/10.1617/s11527-019-1395-0>.
- [60] E. Köken, A. Özarslan, New testing methodology for the quantification of rock crushability: Compressive crushing value (CCV), *Int. J. Miner. Metall. Mater.* 25(11) (2018) 1227-1236. [10.1007/s12613-018-1675-7](https://doi.org/10.1007/s12613-018-1675-7).
- [61] T. Korman, G. Bedekovic, T. Kujundzic, D. Kuhinek, Impact of physical and mechanical properties of rocks on energy consumption of jaw crusher, *Physicochem. Probl. Miner. Process.* 51(2015). [10.5277/ppmp150208](https://doi.org/10.5277/ppmp150208)
- [62] Y. Zeng, E. Forssberg, Energy consumption in fine crushing and dry rod grinding, *Min. Metall. Explor.* 9(2) (1992)69-72. [10.1007/BF03402973](https://doi.org/10.1007/BF03402973)
- [63] H. Krour, R. Trauchessec, A. Lecomte, C. Diliberto, L. Barnes-Davin, B. Bolze, A. Delhay, Incorporation rate of recycled aggregates in cement raw meals, *Constr. Build. Mater.* 248 (2020) 118217. [10.1016/j.conbuildmat.2020.118217](https://doi.org/10.1016/j.conbuildmat.2020.118217).
- [64] J. Schoon, K. De Buysser, I. Van Driessche, N. De Belie, Fines extracted from recycled concrete as alternative raw material for Portland cement clinker production, *Cem. Concr. Compos.* 58(2015)70-80. [10.1016/j.cemconcomp.2015.01.003](https://doi.org/10.1016/j.cemconcomp.2015.01.003)
- [65] E. Kwon, J. Ahn, B. Cho, D. Park, A study on development of recycled cement made from waste cementitious powder, *Constr. Build. Mater.* 83 (2015) 174-180. [10.1016/j.conbuildmat.2015.02.086](https://doi.org/10.1016/j.conbuildmat.2015.02.086)
- [66] A. Bordy, A. Younsi, S. Aggoun, B. Fiorio, Cement substitution by a recycled cement paste fine: Role of the residual anhydrous clinker, *Constr. Build. Mater.* 132 (2017)1-8. [10.1016/j.conbuildmat.2016.11.080](https://doi.org/10.1016/j.conbuildmat.2016.11.080)
- [67] G. Bianchini, E. Marrocchino, R. Tassinari, C. Vaccaro, Recycling of construction and demolition waste materials: a chemical–mineralogical appraisal, *Waste Manage.* 25(2) (2005)149-159. [10.1016/j.wasman.2004.09.005](https://doi.org/10.1016/j.wasman.2004.09.005).
- [68] K. Kalinowska-Wichrowska, M. Kosior-Kazberuk, E. Pawluczuk, The properties of composites with recycled cement mortar used as a supplementary cementitious material, *Materials* 13(1) (2019) 64. [10.3390/ma13010064](https://doi.org/10.3390/ma13010064).
- [69] M. V. A. Florea, Z. Ning, H. J. H. Brouwers, Activation of liberated concrete fines and their application in mortars, *Constr. Build. Mater.* 50 (2014) 1-12. [10.1016/j.conbuildmat.2013.09.012](https://doi.org/10.1016/j.conbuildmat.2013.09.012).
- [70] M. Braga, J. de Brito, R. Veiga, Reduction of the cement content in mortars made with fine concrete aggregates, *Mater. Struct.* 47(1) (2014) 171-182. [10.1617/s11527-013-0053-1](https://doi.org/10.1617/s11527-013-0053-1).
- [71] S. C. Angulo, C. Ulsen, V. M. John, H. Kahn, M. A. Cincotto, Chemical–mineralogical characterization of C&D waste recycled aggregates from São Paulo, Brazil, *Waste Manage.* 29 (2) (2009) 721-730. [10.1016/j.wasman.2008.07.009](https://doi.org/10.1016/j.wasman.2008.07.009).
- [72] L. Oksri-Nelfia, P. Y. Mahieux, O. Amiri, P. Turcry, J. Lux, Reuse of recycled crushed concrete fines as mineral addition in cementitious materials, *Mater. Struct.* 49(8) (2016) 3239-3251. [10.1617/s11527-015-0716-1](https://doi.org/10.1617/s11527-015-0716-1).
- [73] Z. Shui, D. Xuan, H. Wan, B. Cao, Rehydration reactivity of recycled mortar from concrete waste experienced to thermal treatment, *Constr. Build. Mater.* 22(8) (2008)1723-1729. [10.1016/j.conbuildmat.2007.05.012](https://doi.org/10.1016/j.conbuildmat.2007.05.012).

- [74] Z. Shui, R. Yu, J. Dong, Activation of fly ash with dehydrated cement paste. *ACI materials Journal*, 108(2) (2011) 204.
- [75] M. V. A. Florea, Secondary materials applied in cement-based products: treatment, modelling and environmental interaction. [Phd Thesis 1 (Research TU/e / Graduation TU/e), Built Environment]. Technische Universiteit Eindhoven. <https://doi.org/10.6100/IR772902>
- [76] V. Corinaldesi, G. Moriconi, Influence of mineral additions on the performance of 100% recycled aggregate concrete, *Constr. Build. Mater.* 23(8) (2009) 2869-2876. 10.1016/j.conbuildmat.2009.02.004
- [77] N. Algourdin, P. Pliya, A. L. Beaucour, A. Noumowé, D. di Coste, Effect of fine and coarse recycled aggregates on high-temperature behaviour and residual properties of concrete. *Constr. Build. Mater.* 341(2022) 127847. <https://doi.org/10.1016/j.conbuildmat.2022.127847>
- [78] R. N. Razafinjato, A. L. Beaucour, R. L. Hebert, B. Ledesert, R. Bodet, A. Noumowe, High temperature behaviour of a wide petrographic range of siliceous and calcareous aggregates for concretes, *Constr. Build. Mater.* 123(2016) 261-273. <https://doi.org/10.1016/j.conbuildmat.2016.06.097>
- [79] Z. Xing, A. L. Beaucour, R. Hebert, A. Noumowe, B. Ledesert, Influence of the nature of aggregates on the behaviour of concrete subjected to elevated temperature, *Cem. Concr. Res.* 41(4)(2011) 392-402. <https://doi.org/10.1016/j.cemconres.2011.01.005>
- [80] P. Hühwohl, I. Brilakis, Detecting healthy concrete surfaces, *Adv. Eng. Inf.* 37 (2018) 150-162, 10.1016/j.aei.2018.05.004.
- [81] T. G. Nijland, J. A. Larbi, Microscopic examination of deteriorated concrete. In *Non-destructive evaluation of reinforced concrete structures*, 137-179, Woodhead Publishing, (2010). 10.1533/9781845699536.2.137
- [82] N. Y. Ho, Y. P. K. Lee, W. F. Lim, T. Zayed, K. C. Chew, G. L. Low, S. K. Ting, Efficient utilization of recycled concrete aggregate in structural concrete, *J. Mater. Civ. Eng.* 25(3) (2013) 318-327. 10.1061/(ASCE)MT.1943-5533.0000587.
- [83] M. Nedeljković, J. Visser, T. G. Nijland, S. Valcke, E. Schlangen, Physical, chemical and mineralogical characterization of Dutch fine recycled concrete aggregates: A comparative study, *Constr. Build. Mater.* 270 (2021) 121475. 10.1016/j.conbuildmat.2020.121475.
- [84] F. Rodrigues, M. T. Carvalho, L. Evangelista, J. De Brito, Physical-chemical and mineralogical characterization of fine aggregates from construction and demolition waste recycling plants, *J. Cleaner Prod.* 52 (2013) 438-445. 10.1016/j.jclepro.2013.02.023.
- [85] S. Beauchemin, B. Fournier, J. Duchesne, Evaluation of the concrete prisms test method for assessing the potential alkali-aggregate reactivity of recycled concrete aggregates, *Cem. Concr. Res.* 104 (2018) 25-36. 10.1016/j.cemconres.2017.10.008
- [86] F. Locati, C. Zega, G. C. dos Santos, S. Marfil, D. Falcone, Petrographic method to semi-quantify the content of particles with reactive components and residual mortar in ASR-affected fine recycled concrete aggregates, *Cem. Concr. Compos.* 119 (2021) 104003. 10.1016/j.cemconcomp.2021.104003
- [87] R. Johnson, M. H. Shehata, The efficacy of accelerated test methods to evaluate alkali silica reactivity of recycled concrete aggregates, *Constr. Build. Mater.* 112 (2016) 518-528. 10.1016/j.conbuildmat.2016.02.155.
- [88] M. H. Shehata, C. Christidis, W. Mikhaiel, C. Rogers, M. Lachemi, Reactivity of reclaimed concrete aggregate produced from concrete affected by alkali-silica reaction, *Cem. Concr. Res.* 40(4) (2010) 575-582. 10.1016/j.cemconres.2009.08.008.
- [89] EN 12620:2002+A1:2008 en, in *Aggregates for concrete*.
- [90] B. A. Bektas, A. Carriquiry, O. Smadi. Using classification trees for predicting national bridge inventory condition ratings, *J. Infrastruct. Syst.* 19(4) (2013) 425-433. 10.1061/(ASCE)IS.1943-555X.0000143
- [91] D. Breyse, J. L. Martínez-Fernández, Assessing concrete strength with rebound hammer: review of key issues and ideas for more reliable conclusions, *Mater. Struct.* 47(9) (2014) 1589-1604. 10.1617/s11527-013-0139-9
- [92] S. K. Choi, N. Tareen, J. Kim, S. Park, I. Park, Real-time strength monitoring for concrete structures using EMI technique incorporating with fuzzy logic, *Applied Sciences* 8(1) (2018) 75. 10.3390/app8010075.
- [93] J. W. Kim, C. Lee, S. Park, K. T. Koh, Real-time strength development monitoring for concrete structures using wired and wireless electro-mechanical impedance techniques, *KSCIE Journal of Civil Engineering*, 17(6) (2013) 1432-1436. 10.1007/s12205-013-0390-1.
- [94] M. Alwash, D. Breyse, Z. M. Sbartaï, K. Szilágyi, A. Borosnyói, Factors affecting the reliability of assessing the concrete strength by rebound hammer and cores, *Constr. Build. Mater.* 140 (2017) 354-363. 10.1016/j.conbuildmat.2017.02.129.
- [95] K. Szilágyi, A. Borosnyói, I. Zsigovics, Extensive statistical analysis of the variability of concrete rebound hardness based on a large database of 60 years experience, *Constr. Build. Mater.* 53 (2014) 333-347. 10.1016/j.conbuildmat.2013.11.113
- [96] N.J. Carino, Nondestructive testing of concrete: History and challenges. In Lee, George C, ed; Chang, K. C, ed. *Proceedings of the International Workshop on Civil Infrastructure Systems: Application of intelligent systems and advanced materials on bridge systems*. Taipei, U.S. National Center for Earthquake Engineering Research (1994) 343-99.
- [97] N. Pereira, X. Romão, Assessment of the concrete strength in existing buildings using a finite population approach, *Constr. Build. Mater.* 110 (2016) 106-116. 10.1016/j.conbuildmat.2016.02.021
- [98] *Recommendations for Testing Concrete by Hardness Methods*, 1984, RILEM.
- [99] EN 13791 Assessment of in-situ compressive strength in structures and precast concrete components. 2019.

- [100] EN 12504-2 Testing concrete in structures - Part 2: Nondestructive testing Determination of rebound number. 2021.
- [101] EN 12504-4 Testing concrete in structures - Part 4: Determination of ultrasonic pulse velocity. 2021.
- [102] D. Breysse, J. P. Balayssac, S. Biondi, D. Corbett, A. Goncalves, M. Grantham, V. A. M. Luprano, A. Masi, A. V. Monteiro, Z. M. Sbartai, Recommendation of RILEM TC249-ISC on non destructive in situ strength assessment of concrete, *Mater. Struct.* 52(4) 2019 1-21. 10.1617/s11527-019-1369-2.
- [103] D. Breysse, J. P. Balayssac, M. Alwash, S. Biondi, L. Chiauzzi, D. Corbett, V. Garnier, A. Gonçalves, M. Grantham, O. Gunes, S. Kenaï, V. A. M. Luprano, A. Masi, A. Moczko, H. Y. Qasrawi, X. Romão, Z. M. Sbartai, A. V. Monteiro, E. Vasanelli, In-Situ Strength Assessment of Concrete: Detailed Guidelines. In *Non-Destructive In Situ Strength Assessment of Concrete* (2021)3-56, Springer, Cham. 10.1007/978-3-030-64900-5_1
- [104] J. Ingham, *Geomaterials under the microscope: a colour guide* (2019) CRC Press.
- [105] W. Mukupa, C. Hancock, G. Roberts, K. Al-Manasir, H. de Ligt, Z. Chen, Visual inspection of fire-damaged concrete based on terrestrial laser scanner data, *Applied Geomatics*9(3) (2017)143-158. 10.1007/s12518-017-0188-9.
- [106] R. H. Courtier, The assessment of ASR-affected structures, *Cem. Concr. Compos.* 12(3) (1990)191-201. 10.1016/0958-9465(90)90020-X.
- [107] G. S. Senesi, R. S. Harmon, R. R. Hark, Field-portable and handheld laser-induced breakdown spectroscopy: Historical review, current status and future prospects, *Spectrochim. Acta, Part B*, 175 (2021) 106013. 10.1016/j.sab.2020.106013.
- [108] EN 196-2:2014 Method of testing cement - Part 2: Chemical analysis of cement.
- [109] M.S. Shackley, *X-ray fluorescence spectrometry (XRF) in geoarchaeology* (2010) Springer, 10.1007/978-1-4419-6886-9.
- [110] G. L. Bosco, Development and application of portable, hand-held X-ray fluorescence spectrometers, *TrAC Trends in Analytical Chemistry* 45 (2013)121-134. 10.1016/j.trac.2013.01.006.
- [111] J. Johnson, Accurate measurements of low Z elements in sediments and archaeological ceramics using portable X-ray fluorescence (PXRF), *J. Archaeol. Method Theory* 21(3) (2014)563-588. 10.1007/s10816-012-9162-3.
- [112] A. M. Hunt, R. J. Speakman, Portable XRF analysis of archaeological sediments and ceramics. *J. Archaeol. Sci.* 53 (2015) 626-638. 10.1016/j.jas.2014.11.031.
- [113] EN-ISO 13196:2015 Soil quality - Screening soils for selected elements by energydispersive X-ray fluorescence spectrometry using a handheld or portable instrument.
- [114] P. Mikysek, T. Trojek, N. Mészárosová, J. Adamovič, M. Slobodník, X-ray fluorescence mapping as a first-hand tool in disseminated ore assessment: sandstone-hosted U-Zr mineralization, *Miner. Eng.* 141(2019) 105840. 10.1016/j.mineng.2019.105840.
- [115] F. F. Mendonça Filho, H. Morillas, H. Derluyn, M. Maguregui, D. Grégoire, In-situ versus laboratory characterization of historical site in marine environment using X-ray fluorescence and Raman spectroscopy, *Microchem. J.*147 (2019) 905-913. 10.1016/j.microc.2019.02.014.
- [116] T. P. Taylor, E. Yurdakul, H. Ceylan, *Concrete Pavement Mixture Design and Analysis (MDA): Application of a Portable X-Ray Fluorescence Technique to Assess Concrete Mix Proportions*, 2012.
- [117] A. L. Washington, W. Narrows, J. H. Christian, L. Msgwood, Quantitative analysis of concrete using portable x-ray fluorescence: Method development and validation (No. SRNL-STI-2017-00493). Savannah River Site (SRS), Aiken, SC (United States) (2017), 10.2172/1373540.
- [118] Y. Zhu, D. C. Weindorf, W. Zhang, Characterizing soils using a portable X-ray fluorescence spectrometer: 1. Soil texture. *Geoderma*, 167(2011) 167-177.10.1016/j.geoderma.2011.08.010.
- [119] B. Yokhin, X-ray fluorescence analyzer, US patent 6041095A, filed February 24, 1998 and issued March 21, 2000, <https://patents.google.com/patent/US6041095A/en>.
- [120] J. Sherman, The theoretical derivation of fluorescent X-ray intensities from mixtures. *Spectrochim. Acta* 7 (1955)283-306. 10.1016/0371-1951(55)80041-0.
- [121] S1 TITAN," [Online]. Available: <https://www.bruker.com/en/products-and-solutions/elemental-analyzers/handheld-xrf-spectrometers/S1-TITAN.html>. [Accessed 1 June 2021].
- [122] "How does XRF work?," [Online]. Available: <https://www.thermofisher.com/nl/en/home/industrial/spectroscopy-elemental-isotope-analysis/spectroscopy-elemental-isotope-analysis-learning-center/elemental-analysis-information/xrf-technology.html>. [Accessed 1 June 2021].
- [123] P. C. Kreijger, The skin of concrete composition and properties, *Matériaux et Construction* 17(4) (1984) 275-283. 10.1007/BF02479083.
- [124] Robert F. Shannon, Jr., Compact collimating device, US patent 8,223,925 B2, filed April 15, 2010 and issued July 17, 2012, <https://patents.google.com/patent/US8223925B2/en>
- [125] W. Kim, J. Jang, Monte Carlo simulation for the analysis of various solid samples using handheld X-ray fluorescence spectrometer and evaluation of the effect by environmental interferences. *Spectrochim. Acta, Part B* 180 (2021) 106203. 10.1016/j.sab.2021.106203.
- [126] A. J. Nazaroff, K. M. Pruffer, B. L. Drake, Assessing the applicability of portable X-ray fluorescence spectrometry for obsidian provenance research in the Maya lowlands. *J. Archaeol. Sci.* 37(4) (2010) 885-895. 10.1016/j.jas.2009.11.019.
- [127] A. Bourke, P. S. Ross, Portable X-ray fluorescence measurements on exploration drill-cores: comparing performance on unprepared cores and powders for 'whole-rock' analysis, *Geochem.: Explor. Environ. Anal.* 16(2) (2016)147-157. 10.1144/geochem2014-326.

- [128] R. Cesareo, A. Castellano, G. Buccolieri, M. Marabelli, A portable apparatus for energy-dispersive X-ray fluorescence analysis of sulfur and chlorine in frescoes and stone monuments, *Nucl. Instrum. Methods Phys. Res. Sect. B* 155(3) (1999)326-330. 10.1016/S0168-583X(99)00256-6.
- [129] M. K. Kim, J. P. P. Thedja, H. L. Chi, D. E. Lee, Automated rebar diameter classification using point cloud data based machine learning, *Autom. Constr.* 122 (2021)103476. 10.1016/j.autcon.2020.103476.
- [130] X. Li, H. Liu, F. Zhou, Z. Chen, I. Giannakis, E. Slob, Deep learning-based nondestructive evaluation of reinforcement bars using ground-penetrating radar and electromagnetic induction data. *Comput.-Aided Civ. Infrastruct. Eng.* (2021),<https://doi.org/10.1111/mice.12798>.
- [131] K. Tešić, A. Baričević, M. Serdar, Non-Destructive Corrosion Inspection of Reinforced Concrete Using Ground-Penetrating Radar: A Review, *Materials*, 14(4) (2021) 975. 10.3390/ma14040975.
- [132] D. Isailović, V. Stojanovic, M. Trapp, R. Richter, R. Hajdin, J. Döllner, Bridge damage: Detection, IFC-based semantic enrichment and visualization, *Autom. Constr.* 112 (2020) 103088, 10.1016/j.autcon.2020.103088.
- [133] I. Bertin, R. Mesnil, J. M. Jaeger, A. Feraille, R. Le Roy, A BIM-based framework and databank for reusing load-bearing structural elements, *Sustainability*, 12(8) (2020)3147. 10.3390/su12083147.



Influence of biomass ash and coconut shell in scrap steel fiber reinforced concrete

Vijayalakshmi Ramalingam^{*1)}, Yogesh Balamurugan¹⁾, Prashant Selvam¹⁾,
Nitish Kanna Kalimuthu¹⁾, Thosi Giri¹⁾

¹⁾ Department of Civil Engineering, Sri Sivasubramaniya Nadar College of Engineering, Kalavakkam Chennai-603110, Tamil Nadu, India

Article history

Received: 22 September 2022

Received in revised form:

08 November 2022

Accepted: 24 November 2022

Available online: 30 March 2023

Keywords

coconut shell concrete;
bagasse ash;
scrap steel fiber;
workability

ABSTRACT

To develop a sustainable concrete solution, the aggregates and cement in the concrete mixture were partially replaced with *Cocos nucifera* endocarp (coconut shell) aggregate and biomass ash (sugarcane bagasse ash) respectively. The fresh and hardened properties were studied for three types of mixes (i) the concrete mix with 10-30% replacement of cement with bagasse ash (BA), (ii) Bagasse ash concrete mix with scrap steel fiber and (iii) Bagasse ash concrete with scrap fiber and 10 - 50% coconut shell aggregate. The fresh property of concrete is positively influenced by the addition of bagasse ash. With the addition of scrap fibers and coconut shell the workability reduces by 47% when compared to the control mix. The slump values recorded for all the mixes were within the permissible limit. The density of concrete decreases with the inclusion of bagasse ash and coconut shell which helps reduce the dead weight of structural elements. The mechanical property of concrete increased by 5%, 6% and 8% in compression, split and flexure modes respectively, for 10% bagasse ash steel fiber reinforced concrete. Replacement of gravel with coconut shell affects the strength properties, but all the values were within the permissible limit for structural concrete application. The SEM image analysis showed that the porosity increased with coconut shell content. From the fresh and hardened concrete test results, it was observed that the coconut shell, bagasse ash and scrap fiber can be effectively used as substitutes for concrete ingredients to develop a sustainable fiber reinforced concrete solution.

1 Introduction

Urbanization results in the rapid depletion of natural resources at high speed and leads to the large amounts of energy consumption. Concrete, being the important material in the construction industry, consumes tons of cement, sand, and gravel. Concrete production per person in developed countries ranges between 1.5 and 3 tonnes per year. At this rate of consumption, it is difficult to meet the resource requirements for our future generation [1]. Therefore, in order to maintain sustainability and reduce the consumption of natural resources at a faster rate, the major ingredients in concrete, namely cement and aggregate are replaced with new sustainable materials. The sustainable materials are either industrial waste byproducts or agricultural waste byproducts which reduce CO₂ emissions, and the dumping waste on open land, thereby reducing environmental pollution without compromising the strength of concrete and concrete composites [2]. Out of the total natural resource consumption, coarse aggregate contributes about 70-80% of the total amount; therefore, more focus is given to alternative aggregate materials such as copper slag, steel slags, sintered fly ash aggregate, and agricultural waste such as palm shell, coconut shell, kernel shell etc. These byproducts

and waste materials are used as replacements for mineral gravel aggregate. Compared to high density industrial waste (slags), agricultural waste has a lesser density, better sound insulation, thermal resistance, cost-effective and is also easily renewable. Out of the different shells available as a substitute for gravel aggregate, coconut shell is the most preferred aggregate due to its hard texture and better volume stability [3]. In addition to natural aggregate replacement, much research is also being carried out to reduce the cement consumption in concrete, in which, cement is replaced with low carbon alternative materials with better pozzolanic property. Recently, the use of biomass ash such as corn cob ash, rice straw ash, bagasse ash, rice husk ash, palm oil fuel ash, etc. has increased because of its renewable nature. Compared to fly ash which has excellent pozzolanic properties and is obtained as the combustion residue of coal (non-renewable), biomass ash is preferred in the construction industry [4]. Using such agro-waste as cement and aggregate replacement in the concrete reduces the cost of construction and also reduces the environmental pollution caused by the disposal of those wastes in open land [5]. Aside from cement replacement and natural coarse aggregate replacement, several studies on the mechanical behaviour and durability characteristics of fiber-reinforced

* Corresponding author:

E-mail address vijayalakshmir@ssn.edu.in

concrete have been conducted over the last two decades. A variety of synthetic fiber and plant fibers such as polyolefin, glass, carbon, polypropylene, banana fiber, sisal fiber, caryota fiber, roselle fiber, jute fiber, and coconut fiber are used as reinforcement in concrete nowadays to improve the mechanical strength and ductility characteristics of both normal and light weight aggregate concrete [6],[7],[8],[9],[10], [11]. Even though synthetic fibers have better thermal resistance, mechanical strength and durability, when compared to natural fibers, plant fibers are much preferred nowadays, due to their low cost and highly renewable nature[12],[13],[14],[15]. Using steel fibers of different aspect ratios and origins helps enhance the mechanical properties of concrete [16]. Recently much research has been carried out using steel fibers as reinforcement in both normal and light-weight concrete to reduce the brittleness of the material and improve its tensile properties [17],[18]. From the knowledge gained, this research paper will mainly focus on using coconut shell (CS) aggregate as the partial replacement for natural gravel aggregate, bagasse ash (BA) as a partial replacement of cement, and lathe industry scrap steel fibers (SrF) as fiber reinforcement.

2 Recent studies on light weight coconut shell concrete

Much research has been carried out using coconut shell as a partial or complete replacement for natural gravel aggregate. Gunasekaran et al. conducted extensive research on the strength properties, structural behaviour, bond characteristics, long-term compressive and bond strengths, plastic shrinkage, and deflection characteristics of coconut shell concrete, proving that the bond property of coconut shell concrete is higher than the values predicted by standard codes, and that the density and compressive strength of concrete increase as the percentage of coconut shell concrete decreases. The plastic shrinkage area decreases but the deflection increases with the amount of coconut shell replacement. Studies on Coconut Shell Concrete (CSC) pipes subjected to hydrostatic pressure showed that the coconut shell can be used as a partial replacement for aggregate in reinforced cement concrete pipes used for various hydrological applications in medium traffic locations. [19],[20],[21],[22],[23]. Results on the durability properties of CSC showed that the water absorption, permeable voids, chloride penetration, and temperature resistance are much more comparable to other light-weight aggregate concrete. The coconut shell aggregate absorbs water which helps in the hydration process and proper curing conditions are to be adopted to achieve better durability characteristics of coconut shell concrete [24]. In addition to the CS aggregate, coconut shell ash when added to concrete at 10 % cement replacement, has a negative effect on the workability of CS concrete. But the splitting and compressive strength of modified CSC with 10% ash and 5% aggregate subjected to elevated temperature showed better performance, when compared to concrete with only 5% coconut shell aggregate [25]. The coconut shell aggregate concrete with different percentage of replacement of fly ash showed higher deflection, which proves that the CS aggregate reduces the brittleness and improves the ductility of concrete [26]. Addition of different percentage of sisal fibers, steel fibers and polypropylene fibers along with coconut shell aggregate improves the mechanical property mainly the tensile strength of lightweight concrete [2]. In addition to coconut shell, the biochar

obtained from the burnt coconut shell is used to reduce the plastic shrinkage cracks in silica fume cement binder concrete [27]. Addition of coconut fiber in CS aggregate concrete also help to improve the tensile strength of coconut shell concrete [28]. Different plant fibers, steel fibers and synthetic fibers are used as the fiber reinforcement in lightweight coconut shell concrete to improve the tensile and flexural strength properties of coconut shell concrete[29],[30]. To reduce cement consumption and carbon-dioxide emission different pozzolanic industrial and agricultural waste such as fly ash, bagasse ash, quarry dust, coconut char, Coconut Ash has been used as partial replacement for cement [31],[32],[33]. Research work carried out using crushed CS and synthetic biomass modified CS aggregate showed that modified biomass CS concrete has excellent thermal resistance, and can be used as an excellent energy saving building material. Recent research on fiber reinforced coconut shell concrete and its research significance is tabulated in Table 1.

3 Research significance

From the literature study, it can be seen that, many new lightweight aggregates are being identified and added to concrete as a substitute for gravel to produce lightweight concrete, and different strength properties are being studied. Coconut shell is used as a substitute for natural gravel aggregate because it is the hardest and most popular light weight aggregate available in most Asian countries. The mechanical properties, bond characteristics, durability properties, plastic shrinkage behaviour and beam deflection characteristics of CSC were studied in detail by many researchers. These properties were tested in different types of concrete mix either by using coconut shell as partial or complete replacement for gravel aggregate. Along with coconut shell aggregate, pozzolanic binder materials such as fly ash, silica fume and coconut char were used as partial replacements for binder. In addition, to the above-mentioned substitution in concrete, some metal fibers, synthetic fibers and natural fibers such as steel fibers, polypropylene fibers, sisal fibers, coconut fibers etc. were used in different percentages of the volume of concrete, to reduce the brittleness in concrete and impart ductility to lightweight fiber reinforced concrete. From the literature study it was identified that the study on bagasse ash and coconut shell aggregate concrete with scrap steel fibers as reinforcement had not been studied so far. Therefore, this research work focuses on the properties of scrap steel fiber reinforced coconut shell concrete with bagasse ash as a partial replacement for cement.

4 Experimental methodology

4.1 Material characterization

The materials used for the preparation of concrete mix include cement, gravel aggregate, coconut shell aggregate, M – Sand, Bagasse Ash (BA), water reducing admixture and portable water. The sugarcane bagasse ash was received from a sugarcane mill located at virudhachalam district, Tamilnadu, India. To obtain the BA, sugarcane fiber was heated in a muffle furnace at 10°C /min. The burnt ash was subjected to a high temperature of 900°C for 2 hours and then the ash trays were allowed to cooled in the open air. After proper cooling, each sample was ground in a ball mill at 66 rpm, until the fineness of the BA sample was within the

Table 1. Recent study on sustainable coconut shell aggregate concrete

Reference	Year	Aggregate replacement	Cement replacement	Fibers	Properties	Parameters	Conclusion
[17]	2022	Coconut shell	Flyash-10%	Steel fiber	Mechanical properties and Flexural strength of beams	Fiber content varied from 0.25-1% volume of concrete	Both flexural toughness and beam ultimate capacity increased with the fiber content
[34]	2022	Coconut shell-5% replacement	Coconut shell ash-10%	-	Cracking pattern, flexural and shear behaviour of beams	Influence of coconut shell particle on the flexure, shear and cracking pattern of the beams	Combination of coconut shell aggregate and coconut shell particle increase the ductility by 8%.
[30]	2022	Coconut shell partial	Bagasse ash 25%	-	Mechanical property, drying shrinkage and structural performance.	Influence of 25% bagasse ash and combination of CS and gravel aggregate in concrete	concrete with 25% ash and 50% CS showed better performance in shrinkage behaviour which is about 18% less than normal concrete.
[1]	2022	Coconut shell & Synthetic bio mass aggregate	-	-	Microstructure of biomass recycled aggregate coconut shells concrete Mechanical strength, shrinkage and thermal conductivity.	Comparative study on the effect of crushed coconut shell and biomass recycled aggregate in concrete	Energy saving potential and thermal resistance was better in coconut shell and synthetic biomass aggregate concrete compared to normal concrete.
[35]	2021	Coconut shell	Fly ash-10%	Sisal fiber	Mechanical strength and impact resistance	sisal fiber percentage varied from 1-4%	With 3% fiber addition the mechanical strength of concrete increased.
[27]	2020	Gravel	Biochar from coconut	-	Mechanical property and permeability characteristics of biochar replaced cement mortar.	5% wt. of cement and 33 % wt. of silica fumes replaced with biochar. Influence of biochar on the strength and durability properties of mortar.	Autogenous and drying shrinkage reduced by 61% and 23% for the addition of biochar and silica fume in cement mortar.
[36]	2020	Coconut shell	Flyash-10%	Steel fiber	Fresh properties and mechanical property of CS concrete	Fiber content varied from 0.25-1% volume of concrete.	39% increase in compressive strength and 17% increase in MOE were observed.
[37]	2019	Coconut shell	Flyash-10%	Polypropylene fiber	Fresh properties and mechanical property of CS concrete	The volume fractions of polypropylene fibres were 0.25%, 0.5%, 0.75% and 1.0%.	Increased volume fractions of polypropylene fibres reduce the compressive strength
[28]	2019	Coconut shell	-	Coconut fiber	Water absorption, sorptivity, void characteristics, rapid chloride penetration and temperature resistance	Fiber Volume fraction of 3%; Three different curing conditions.	Durability properties were better in full water immersion condition for CS concrete.

range of cement (2750 cm²/g). The pictures of sugarcane crushed fibers, burnt fiber and sieved bagasse ash is shown in Figure 1(a-c). The elemental composition of cement and bagasse ash showed silica contents of 23.86% and 56.37%, respectively. The calcium oxide of the cement binder is about 50.76%, while the Loss on Ignition (LOI) for cement and bagasse ash is around 6-10%. The elemental composition of bagasse ash is within the limit specified by ASTM standards for pozzolana. The detailed chemical composition of cement and BA is listed in Table 2. The XRD of BA ash showed a high range of reactive silicas and oxides, as shown in Figure 2. The coconut shells were procured from the coconut mandi located at Thiruporur, Kanchipuram district, Tamilnadu. The dry coconut shell was crushed using a crusher in such a way that the gradation of the broken coconut shell ranges from

4.75 mm to 12 mm aggregate size to achieve high packing density. The coconut shells collected from the coconut mandi and the broken coconut shell of size 4.75 mm to 12 mm are shown in Figure 3. To improve the strength of CSC, scrap steel fiber (Figure 4), stored as waste in the manufacturing laboratory was collected and used as fiber reinforcement. The length of the fibers was cut to 20-40 mm and the diameter of the scrap steel fibers varies from 0.5 -0.7 mm. The physical properties of coconut shell gravel and scrap steel fiber are listed in Table 3. The Scanning Electron Microscope (SEM) image showing the uniform crystalline structure of cement particles and image of bagasse ash with spherical, cuboidal and polygonal particles along with porous structure of coconut shell are shown in Figure 5 (a-c).



Figure 1. (a) Sugarcane fiber (b) burnt bagasse ash (c) sieved bagasse ash

Table 2. Chemical properties of cement and bagasse ash

Material	SiO ₂	Al ₂ O ₃	Fe ₂ O ₃	CaO	P ₂ O ₅	Na ₂ O	K ₂ O	MgO	LOI
Cement	23.86	5.77	2.19	50.76	0.12	0.91	0.92	1.36	6.97
Bagasse Ash (BA)	56.37	14.61	5.04	2.36	0.85	1.57	3.29	1.43	10.53

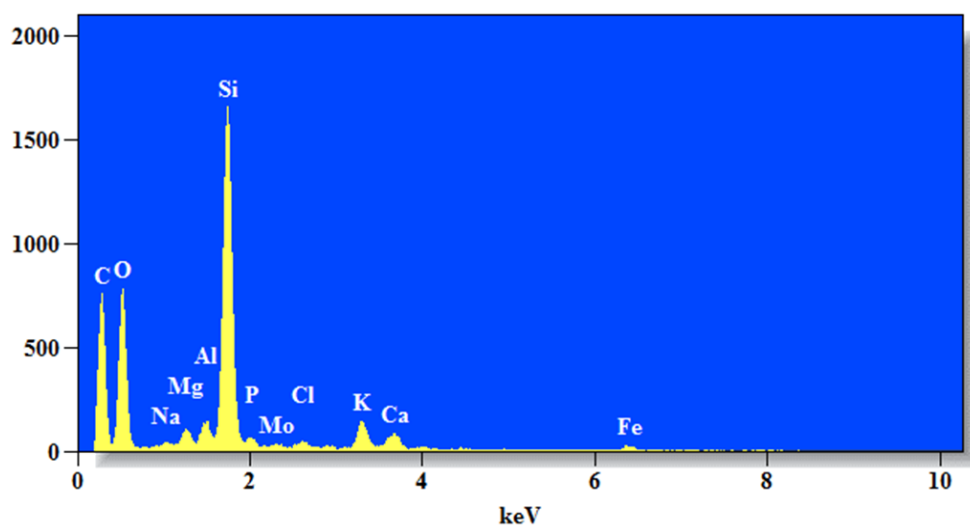


Figure 2. Elemental composition of bagasse ash

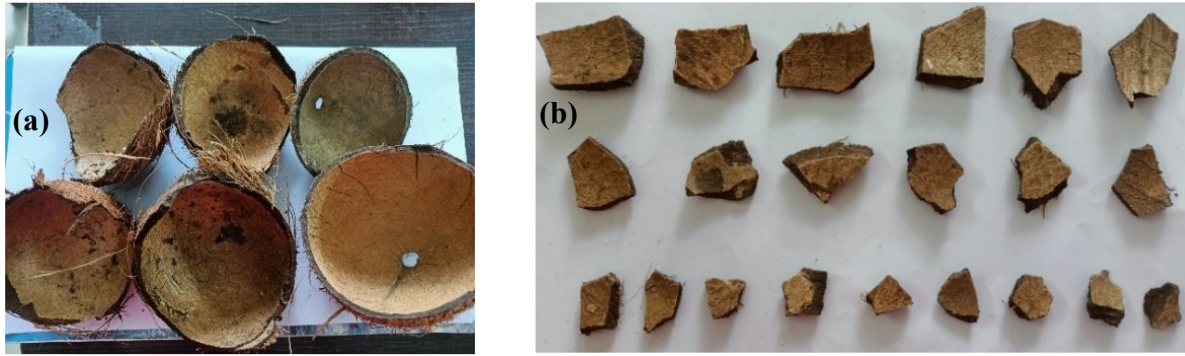


Figure 3. (a) Coconut shells (b) broken shells of 4.75-12 mm sizes



Figure 4. Scrap steel fiber

Table 3. Physical property of coconut shell and scrap steel fiber

Physical Properties	Specific Gravity	Crushing Value (%)	Impact Value (%)	Water Absorption (%)	Fineness Modulus	Bulk Density (kg/m ³)	Abrasion value (%)	Crushing value (%)
Gravel	2.85	20.2	18.6	0.66	6.79	1.68	10.5	20.5
Coconut shell	1.20	2.58	8.15	24	6.26	550	1.8	2.67
Physical Properties of scrap steel fiber	Cross-section	Diameter (mm)	Length (mm)	Unit Weight (kg/m ³)	Elasticity modulus (N/mm ²)	Tensile strength (N/mm ²)	Aspect ratio (%)	Elongation (%)
	deformed and straight	0.3 – 0.75	5 – 20	7850	2x10 ⁵	500 – 3000	45 – 100	5 – 35

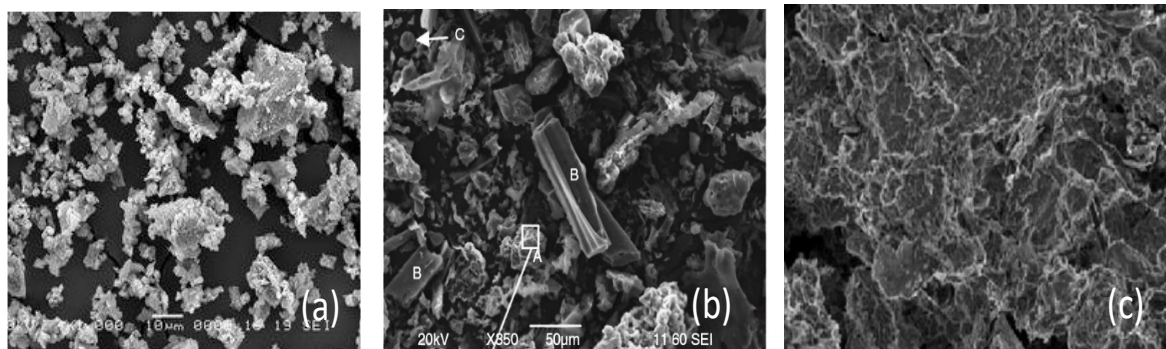


Figure 5. SEM image of (a) cement; (b) bagasse Ash with polygonal (A), cuboidal (B) and spherical (C) shaped particles; (c) coconut shell

4.2 Mix proportions and specimen ID

Before the preparation of the concrete mix, the broken shell was immersed in a water tub for 48 hours, to prevent the absorption of water by coconut shell from the wet concrete mix. The control mix's ingredients, namely cement, sand, coarse aggregate, water, and plasticizer, were mixed in the following proportions: 1:1.64:1.72: 0.32: 0.01. River sand of specific gravity of 2.37 and a fine modulus of 2.9 was used as fine aggregate. Totally, ten mixes were prepared, the first mix is the control mix without any mineral admixtures and 100% cement (CM). The second set of mixes was the bagasse ash replaced concrete mix, in which the bagasse ash was replaced at 10-30 % by weight of cement and designated as CM-10BA, CM-20BA, CM-30BA for 10%, 20 % and 30% of replacement of cement respectively. From the second set of mix the optimum percentage of BA replacement was determined and the same percentage of replacement of BA was maintained for the third set of concrete mixes. For the third set, a total of six mixes were prepared, starting with a concrete mix with 10% BA, 3% scrap steel fiber and 100% gravel aggregate (CM-BA-SrF). In the remaining mixes, the coarse aggregate was replaced at a percentage of 10-50% with coconut shells. Along with the coconut shell addition, 10% of BA and 3% steel fiber were

maintained constant throughout all the mixes. The mixes were identified as CS1-BA-SrF for 10 % coconut shell replacement, 10% BA and 3% scrap fiber. Similarly, the other mixes were identified accordingly. The mix proportions are listed in Table 4.

4.3 Testing of specimens

The workability of control and coconut shell concrete was determined by conducting a slump cone test. The slump values were noted for each mix and only one trial was done for the slump cone test. The fresh density and hardened density of each mix were calculated by measuring the weight of the specimen in the fresh state, hardened state and after oven drying. The strength properties of concrete specimens were assessed by conducting compressive strength tests on a cube of 150 mm size, splitting tensile strength test on cylinder specimens of dimensions 150 mm × 300 mm, flexural strength tests on a 100 mm × 100 mm × 500 mm beam, and modulus of elasticity tests on a 150 mm × 300 mm cylinder. The test set used to measure the strength properties is shown in Figure 6 (a-e). For the hardened concrete test, three specimen readings were noted and the average value of the strength properties were calculated and tabulated in Table 5.

Table 4. Mix proportions

Specimen ID	Cement (kg/m ³)	Bagasse Ash (kg/m ³)	Sand (kg/m ³)	Coarse Aggregate (kg/m ³)	Coconut shell (kg/m ³)	Scrap steel fiber (kg/m ³)	Water content (kg/m ³)	Super plasticizer (kg/m ³)
CM-1	500	-	970	1010	-	-	160	5
CM -10 BA	450	50	970	1010	-	-	160	5
CM -20 BA	400	100	970	1010	-	-	160	5
CM -30 BA	350	150	970	1010	-	-	160	5
CM-BA-SrF	450	50	970	1010	-	15	160	5
CS1-BA- SrF	450	50	970	924	37	15	160	5
CS2-BA- SrF	450	50	970	838	74	15	160	5
CS3-BA- SrF	450	50	970	752	111	15	160	5
CS4-BA- SrF	450	50	970	666	148	15	160	5
CS5-BA- SrF	450	50	970	580	185	15	160	5



Figure 6. Fresh and hardened concrete test setup

Table 5. Density and workability properties of control and coconut shell concrete

Specimen ID	Wet density (kg/m ³)	Demolded density (kg/m ³)	Air dried density (kg/m ³)	Oven dried density (kg/m ³)	Slump
CM	2708	2631	2625	2560	85
CM -10 BA	2645	2504	2489	2433	78
CM -20 BA	2610	2480	2425	2390	76
CM -30 BA	2590	2455	2394	2350	75
CM-BA-SrF	2693	2593	2581	2530	73
CS1-BA-SrF	2563	2323	2311	2255	65
CS2-BA-SrF	2347	2299	2290	2228	61
CS3-BA-SrF	2240	2246	2222	2160	56
CS4-BA-SrF	2169	2169	2160	2100	52
CS5-BA-SrF	2010	2107	2077	1995	45

5 Results and Discussion

An experimental study was done to understand the fresh and hardened properties of coconut shell scrap steel fiber reinforced concrete. The fresh density, hardened density and slump values were measure for all the mixes and tabulated. Similarly, the hardened concrete test such as compressive, split, modulus of elasticity and flexural properties were measured and tabulated.

5.1 Density of scrap steel fiber reinforced CS concrete

For each mix, the fresh weight of the concrete specimen, the weight of the demolded specimen, weight of the specimen following 24 hours of air drying, and the final weight of the specimen following 24 hours of oven drying at 120°C were measured. The fresh density, air-dried density, and oven-dried density were determined and summarised in Table 5. Normally the density of light weight aggregate concrete varies between the range of 1600-2000kg/m³, but in the present study the gravel aggregate was partially replaced with CS, and therefore the oven dry density of coconut shell concrete varied from 2255-1995kg/m³, in

which, the CS5-BA-SrF mix with 50% replacement of CS falls under the category of light weight concrete. For the control mix (CM) the density of concrete was around 2560 kg/m³, as the cement content was partially replaced with 10-30% BA, the dry density decreased from 2433kg/m³ to 2350kg/m³. This is because, specific gravity of BA ranges is lesser when compared to cement. Therefore when cement is replaced with BA, a higher volume of concrete will result in a lesser density [38]. For 10%, 20% and 30% replacement of cement with BA, the density reduction is approximately around 5%, 7% and 8% respectively. The addition of SrF to BA replaced concrete (CM-BA-SrF) slightly increased the density from 2433 kg/m³ to 2530 kg/m³, due to the addition of steel fiber. For the third set of mixes namely the coconut shell concrete, the density decreases with the increased percentage of CS. For 10% replacement of CS the wet density and dry density were around 2563 kg/m³ and 2255 kg/m³ respectively. As the replacement percentage increases to 50%, the wet density and dry density decrease to 2010 kg/m³ and 1995 kg/m³. The variation of density for the control mix (CM) and BA concrete mix with BA(CM-BA) and coconut shell BA concrete with scrap steel fiber (CS-BA-SrF)) is shown in Figure 7.

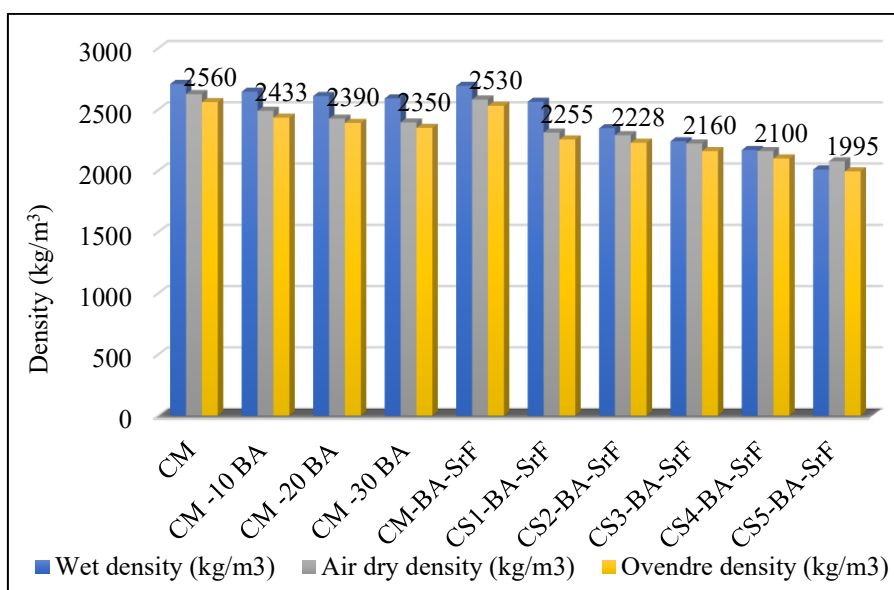


Figure 7. Wet density, air dried density and oven dried density of CS-SrF reinforced concrete

The linear empirical equations that relate the percentage of coconut shell content to the density of concrete are given by equation (1). It can be observed that a very high coefficient of determination (0.96) was obtained. The linear regression plot to correlate density with the compressive strength is shown in Figure 8 and the developed equation with a high regression value ($R^2 = 0.91$) is given by equation (2).

$$D = -64.8 CS\% + 2342 \quad (1)$$

$$D = 298.59\sqrt{fc'} + 549.47 \quad (2)$$

5.2 Workability of scrap steel fiber reinforced CS concrete

The slump test is very frequently used to measure the flowability of concrete. The slump values determine the ease with which the concrete flows and is placed in the mould. The slump value recorded for the present work is listed in Table 5. The variation of slump for the control mix, concrete mix with BA and coconut shell concrete mix with scrap steel fiber is shown in Figure 9. Previous research work suggested that the slump of conventional concrete varies from 100-125 mm, while that of lightweight aggregate concrete ranges from 50 mm to 75 mm [40]. In the present study, the slump value of coconut shell concrete ranged between 65 mm and 45 mm. The slump value recorded for the control mix was 85 mm, which increased with the amount of bagasse ash in concrete. With the addition of 10%, 20% and 30% of BA the slump

value increases to 89 mm, 90 mm, 92 mm respectively. The reason for this increase in the workability is that, the bulk density of BA which is less than cement, fills small pores in the cement matrix, occupies more volume in the concrete mix making it less permeable and more flowable. Therefore, the addition of mineral admixtures up to 5-20% increases the workability of concrete [38]. The addition of steel fibers hinders the movement of aggregate and thereby reduces the workability of fresh concrete. The workability of CM-BA-SrF concrete reduces from 89 mm to 73 mm with the addition of 3% of scrap steel fiber. The workability of coconut shell scrap steel fibre reinforced concrete is further reduced to 65 mm, 61 mm, 56 mm, 52 mm, and 45 mm for 10%, 20%, 30%, 40%, and 50% coarse aggregate replacement, respectively. The irregular shape of coconut shell and the flaky nature of coconut shell tend to reduce the workability of concrete. The correlation between the slump and CS percentage for all the concrete mixes is shown in Figure 10. The correlation equation relating the slump (S) with the percentage of replacement of coconut shell (CS%) is given by equation (3). The correlation equation predicted by other researchers, for CS concrete with steel fiber [36]; CS concrete with sisal fiber [2] is given by equations (4) and (5) respectively.

$$S = -0.6971CS\% + 78.095 \quad (3)$$

$$S = -48 SF + 74 \quad (4)$$

$$S = -8.5 SiF + 72 \quad (5)$$

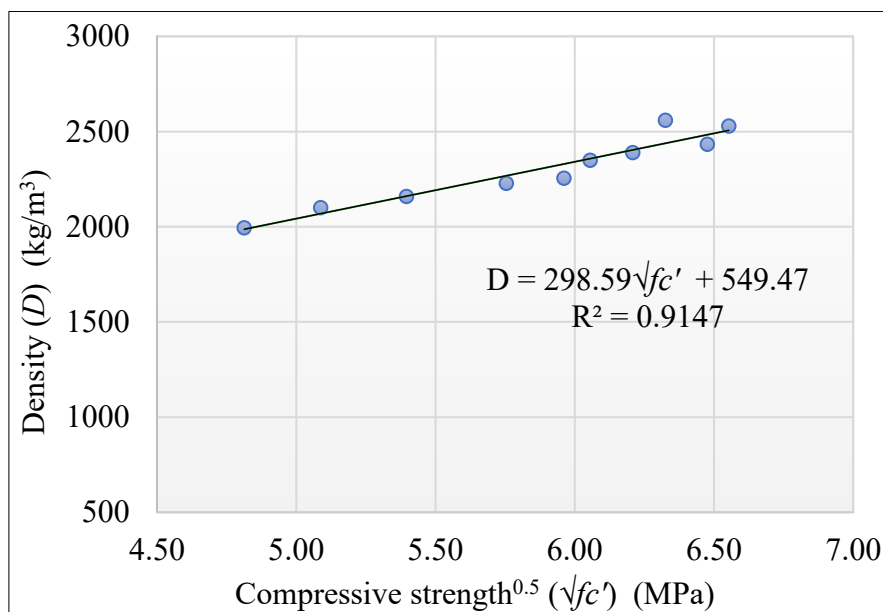


Figure 8. Correlation of density with compressive strength^{0.5}

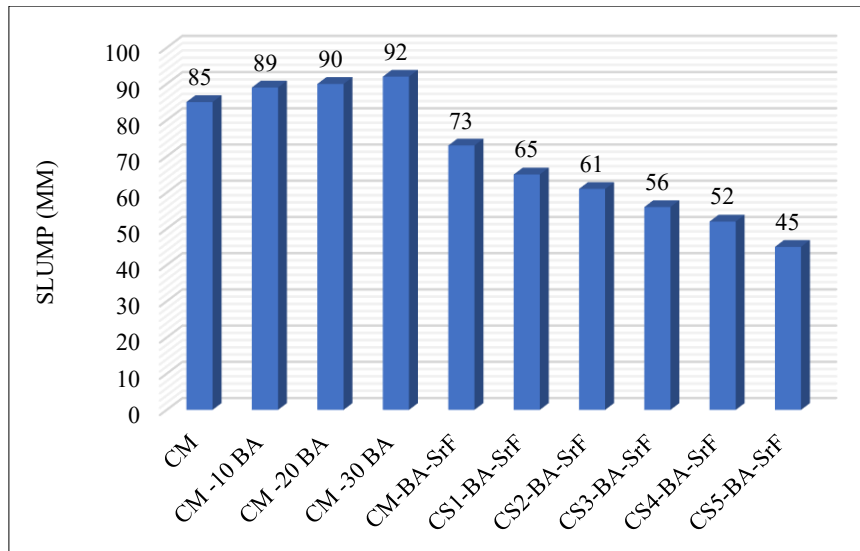


Figure 9. Variation of slump for control and coconut shell concrete

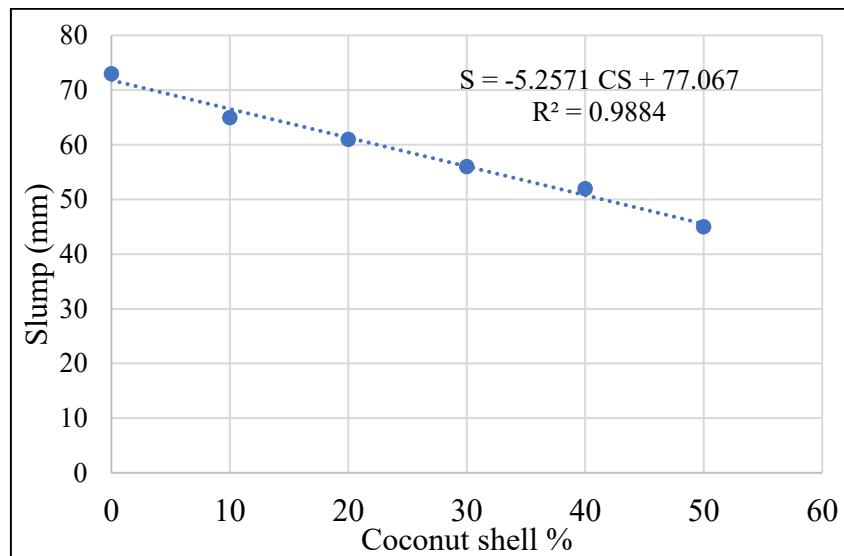


Figure 10. Correlation relation of slump with the percentage replacement of CS

5.3 Compressive Strength

The hardened concrete test was done after 28 days of water curing, and the values are listed in Table 6. The variation of compressive strength of concrete for control mix, bagasse ash concrete mix and fiber reinforced coconut shell concrete mix is shown in Figure 11. In the current study, 10% cement replacement with BA increases compressive strength from 40.01 MPa to 41.94 MPa, which is about 4% higher than the control mix. Previous research on bagasse ash concrete, proved that the strength of concrete, increased with a 5-10% substitution of cement with BA. Beyond 10% the strength is slightly affected [38]. The increase in strength properties is due to the high silica content of BA which is obtained during the burning process of sugarcane fiber at 800°C in control chamber. The silica content in BA has excellent pozzolanic property which helps to improve the strength of concrete [30]. Also the lower bulk density of BA occupies small pores in the concrete mix which reduces the permeability and also increases the compressive strength [4]. From the tabulated values it can be concluded that, out

of three types of cement replaced bagasse ash concrete mix, the concrete mix with 10% BA showed increase in compressive strength. Our present result matches well with the previous research findings on BA replaced concrete. Therefore, 10% replacement of cement with BA was adopted as standard for other mixes with coconut shell and scrap steel fibers. The fibre in the fiber-reinforced BA concrete mix holds the aggregates and cement matrix together and effectively distributes the crack, delaying the formation of a major crack plane and increasing load carrying capacity. The compressive strength of fiber reinforced BA concrete (CM-BA-SrF) showed up to 2% increase in strength compared to unreinforced mix (CM-10BA). It was proven from the authors previous research work that, up to 3% of fiber addition will help to improve the strength of fiber reinforced concrete [8]. Therefore 3% of steel fibers added were maintained for the remaining concrete mixes with coconut shell. The Scanning Electron Microscope (SEM) image of 20% and 30% CS concrete along with the failed specimen is shown in Figure 12 (a-d).

Table 6. Strength properties of control and coconut shell steel fiber reinforced concrete

Specimen ID	Compressive Strength (N/mm ²)	Splitting Tensile Strength (N/mm ²)	Flexural Strength (N/mm ²)	Modulus of Elasticity (GPa)
CM	40.01	3.76	4.43	27.39
CM -10 BA	41.94	3.89	4.62	28.04
CM -20 BA	38.54	3.65	4.35	26.88
CM -30 BA	36.67	3.54	4.29	26.22
CM-BA-SrF	42.95	3.98	4.78	29.23
CS1-BA-SrF	35.54	3.56	4.47	27.10
CS2-BA- SrF	33.11	3.31	4.23	25.40
CS3-BA- SrF	29.11	3.11	4.18	24.23
CS4-BA- SrF	25.88	2.97	4.01	23.11
CS5-BA- SrF	23.17	2.87	3.91	21.20

For the coconut shell fiber reinforced concrete, the compressive strength decreases with the increase in coconut shell percentage. When coarse aggregate is replaced with coconut shell, the strength decreases from 42.95 MPa to 35.54 MPa, 33.11 MPa to 29.11 MPa, and 25.88 MPa to 23.17 MPa. According to previous research findings, the compressive strength of steel fibre coconut shell concrete was approximately 35.6 MPa [36], and the compressive strength of polypropylene fibre reinforced coconut shell

concrete was approximately 36.8 MPa [37]. Without fiber reinforcement, Gunasekaran et al [19] were able to achieve a compressive strength of 26.7 MPa. Therefore, the present research finding is well within the acceptable range of previous research findings. The compressive strength values of all the CS-BA-SrF reinforced concrete satisfied the minimum requirement of structural lightweight concrete (20MPa) for all percentages of replacement of CS.

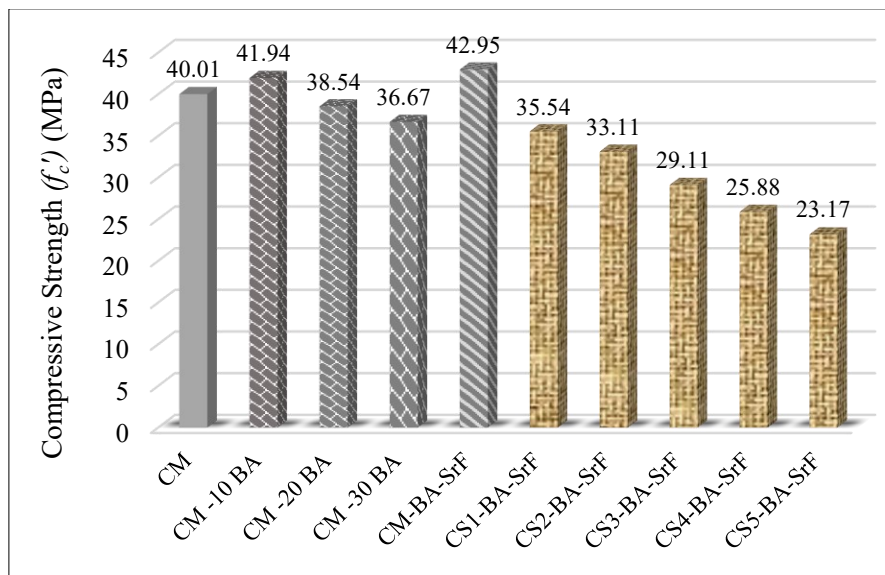


Figure 11. Compressive strength of control, BA concrete and coconut shell scrap steel fiber concrete

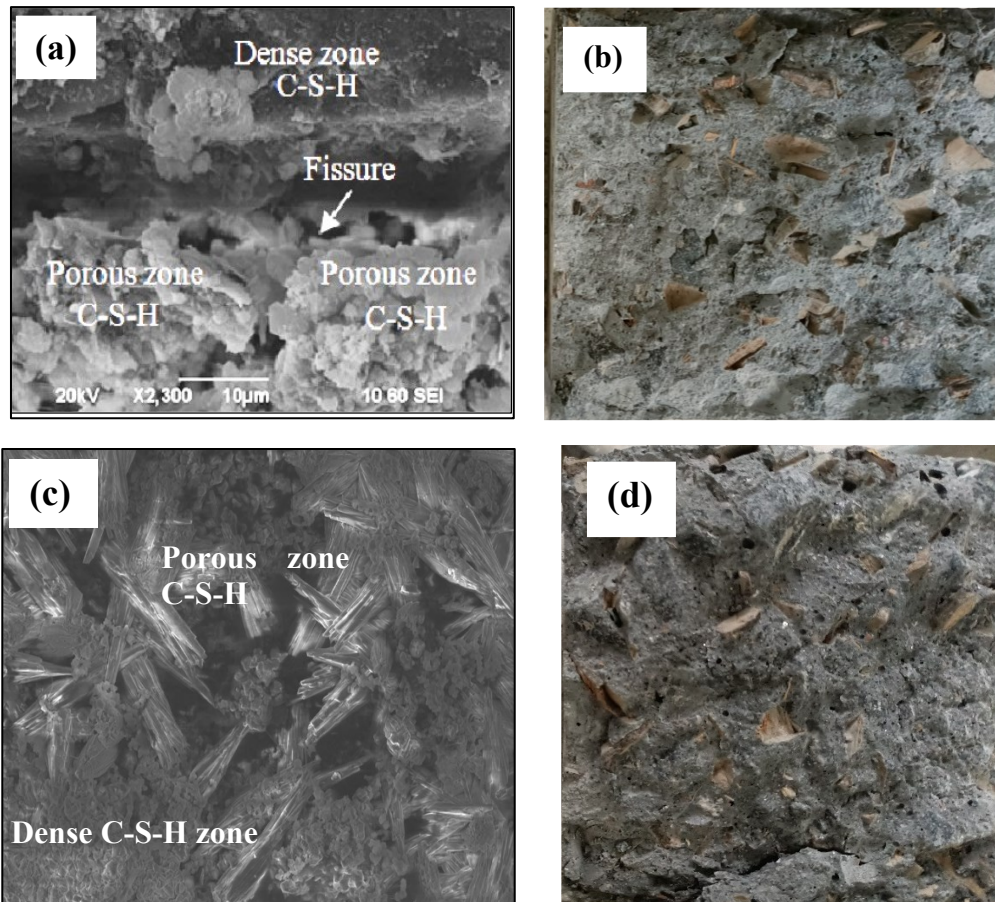


Figure 12. (a & c) SEM image of CS concrete showing the dense and porous Calcium-Silicat-Hydrate (C-S-H) region; (b & d) tested CS cube specimen

5.4 Split tensile strength

The splitting tensile strength values of all the concrete mixes are listed in Table 6. The variation of splitting tensile strength for all the mixes is shown in Figure 13. The splitting tensile strength of the control mix was 3.76 Mpa, which increased by 3.5% with the addition of 10% BA. Similar to compressive strength, the tensile strength also showed an increase in the splitting tensile strength for 10% of BA, beyond which the splitting tensile strength decreases. For the fiber reinforced mix, the addition of 3% scrap steel fiber increases the tensile strength from 3.89 to 3.98 MPa. As the steel fibers have a higher tensile strength, the fiber binds the aggregate and the cement matrix together, preventing propagation of cracks and helping to improve the tensile strength. For fiber reinforced coconut shell concrete, the tensile strength decreases with an increase in the percentage of coconut shell. The density of CS aggregate, the orientation of the aggregate, the bond between the aggregate and the cement matrix, or the thin shape of coconut shell aggregate all contribute to a reduction in strength properties [30]. Fracture of CS aggregate was not identified in any of the tested specimens, which proves that the brittle nature of CS does not affect the strength of concrete when used as replacement for conventional aggregate [19]. Figure 14(a-f) depicts the tested specimen with the irregular orientation of CS aggregate and uncrushed CS aggregate after loading. For 10%, 20%, 30%, 40% and 50% CS aggregate scrap steel fiber reinforced concrete the

splitting strength was 3.56 MPa, 3.31 MPa, 3.11 MPa, 2.97 MPa and 2.87 MPa. Despite the fact that the strength decreases as the percentage of CS replaced increases, the splitting tensile strength recorded for all of the coconut shell scrap fibre mixes was well within the minimum splitting tensile strength requirement (2 MPa) for structural light weight concrete. In the previous research work, the Splitting tensile strength values of coconut shell brick aggregate concrete with 0%, 5%, 10% and 15% of CS were about 2.75, 2.87, 2.25 and 2.09 MPa, respectively [41]. Prakash et al [37] reported that inclusion of polypropylene fibres showed a split tensile strength of 3.12 Mpa and 3.65 MPa for full and partial replacement of coconut shell. The addition of steel fibers showed improved splitting tensile strength of 4.25 Mpa for partially replaced coconut shell concrete [36].

Figure 15 depicts the linear regression plot used to develop a correlation between compressive strength and splitting tensile strength. The empirical equation developed, to correlate splitting tensile strength with compressive strength with a high regression value ($R^2 = 0.98$) is given by equation (6). The previous research equations correlating splitting tensile strength with the compressive strength of coconut shell concrete with sisal fiber, polypropylene fiber and steel fiber reinforcement are given by equations (7), (8) and (9) respectively. The developed relation matches well with the previous researchers' equations.

$$f_{t(SrF)} = 0.65\sqrt{f_c}$$

$$(6) \quad f_{t(PPF)} = 0.66\sqrt{f_c} \quad (8)$$

$$f_{t(SiF)} = 0.531\sqrt{f_c}$$

$$(7) \quad f_{t(SF)} = 0.82\sqrt{f_c} \quad (9)$$

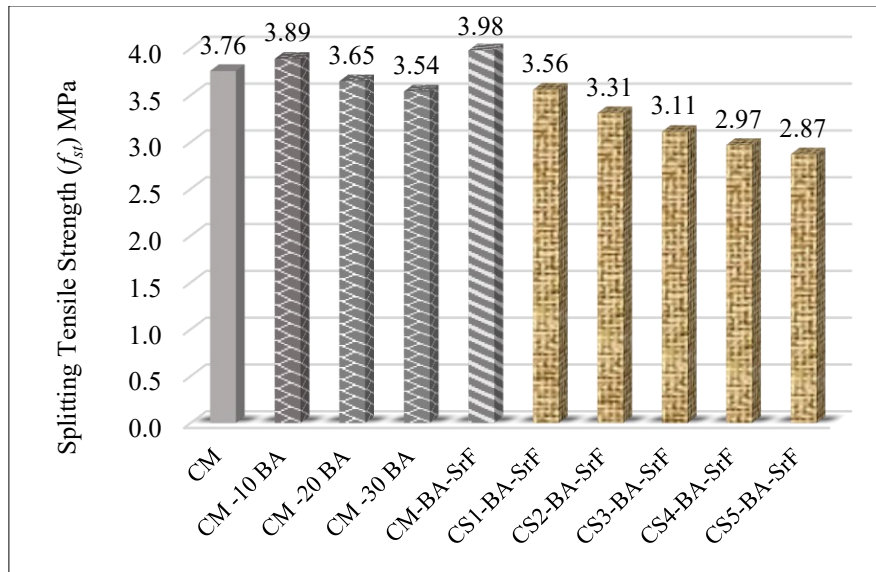


Figure 13. Splitting tensile strength of control, BA concrete and fiber reinforced coconut shell concrete

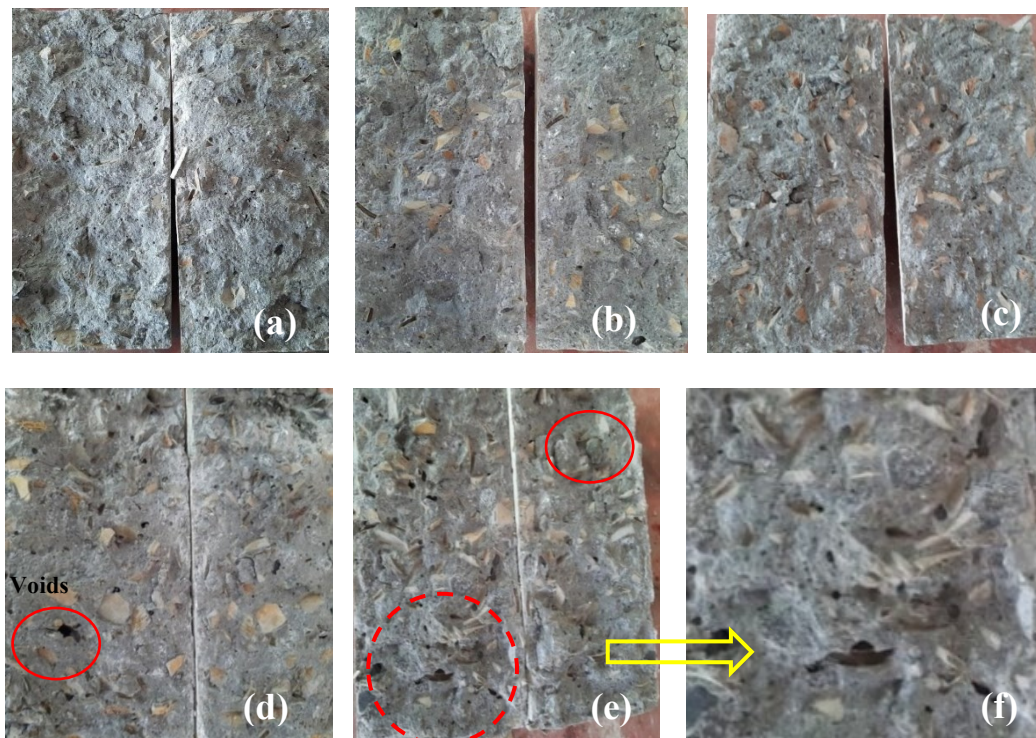


Figure 14. (a-e) Failed specimen of 10%,20%,30%,40% and 50 % CS concrete; (f) increase in voids with CS%

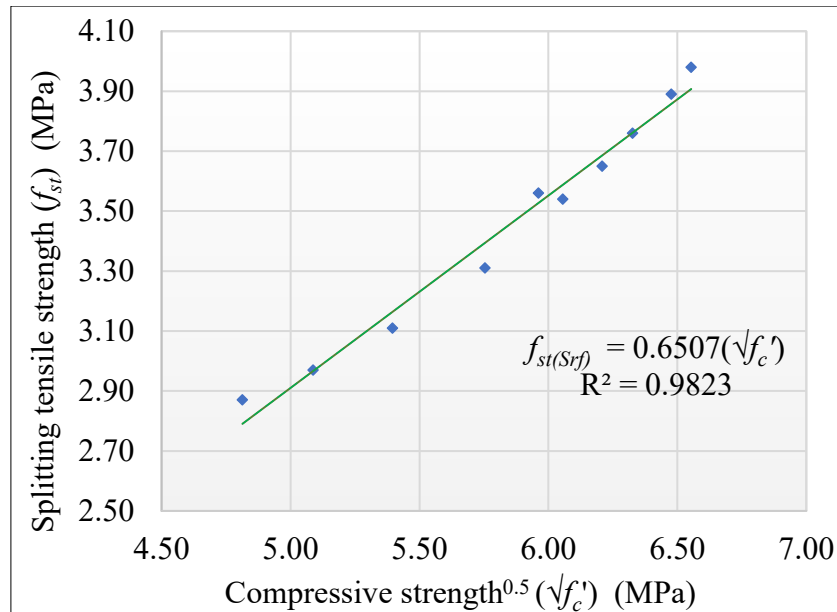


Figure 15. Regression plot of splitting tensile strength and compressive strength

5.5 Flexural Strength

The flexural strengths of normal and coconut shell fiber reinforced concrete are given in Table 5. The flexural strength of control specimen was 4.9 MPa which increased by 8.5% for a 10% replacement of cement with BA. Similar to compression and splitting tensile strength, the flexural strength also increases with the addition of 10% of BA, beyond which the strength reduces. For the fiber reinforced mix the strength increased by 16 % with the addition of 3% scrap steel fiber when compared to control mix (CM). The post-peak toughness of the beam under flexural load is increased by the addition of fiber. All the fibers embedded in the concrete matrix are involved in the stress transfer, which continues until the failure of the specimen, which occurs after the ultimate capacity of the fibers is reached. The failure pattern of the beam and the fiber involved in the bridging of cracks is shown in Figure 16. For the coconut shell fiber reinforced mix, the flexural strength values vary from 5.32 MPa, 5.21 MPa, 5.11 MPa, 4.98 MPa and 4.78 MPa for 10%, 20%, 30%, 40% and 50% CS fiber reinforced concrete respectively. The variation of flexural strength is shown in Figure 17. In the previous work, the addition of sisal fiber showed a flexural strength of 5.7 MPa, which corresponds to 22% increase in the flexural strength for a 4% addition of sisal fiber [43]. Similarly, Gunasekaran et al reported a flexural strength of 4.78 Mpa without any fiber reinforcement [19]. The present flexural strength values agree well with the previous research findings. The linear regression plot to develop a correlation between the compressive strength and flexural strength with a high regression value ($R^2 = 0.91$) is shown in Figure 18. The developed equation relating flexural and compressive strengths is given by equation (10). The

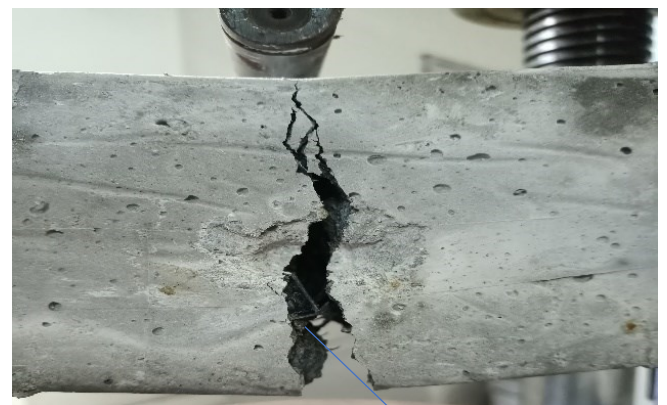
previous research equation correlating flexural strength with the compressive strength of coconut shell concrete with sisal fiber, polypropylene fiber and steel fiber reinforcement are given by equations (11), (12), and (13), respectively. The developed relation matches well with the previous researchers' equations.

$$f_{r(SrF)} = 0.416\sqrt{f_c} \tag{10}$$

$$f_{r(SiF)} = 0.495f_c^{2/3} \tag{11}$$

$$f_{r(PPF)} = 0.562f_c^{2/3} \tag{12}$$

$$f_{r(SF)} = 0.58f_c^{2/3} \tag{13}$$



Fibers involved in crack arresting process

Figure 16. Fibers involved in the crack arresting process

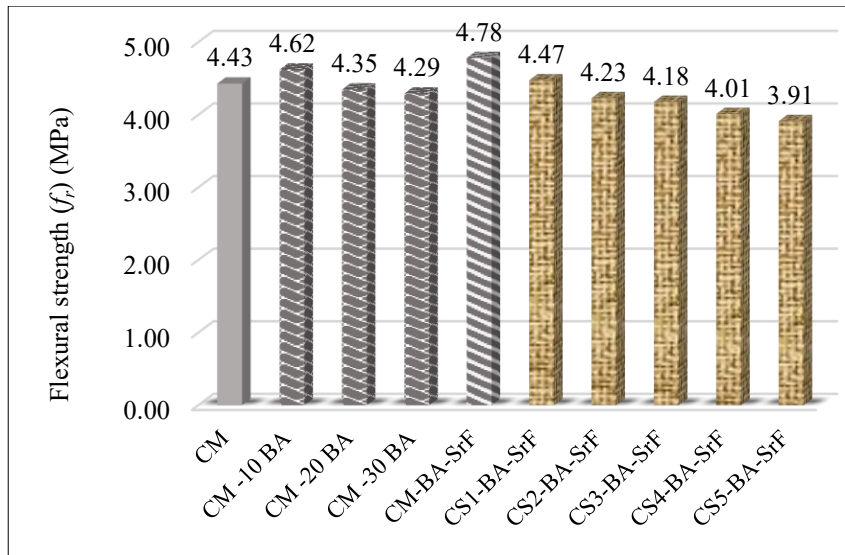


Figure 17. Flexural strength of control, BA concrete and coconut shell scrap steel fiber concrete

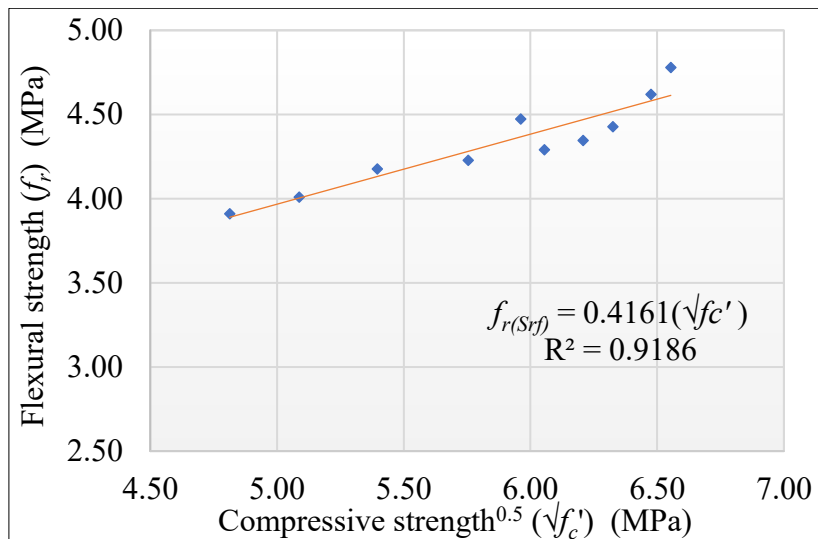


Figure 18. Regression plot of flexural strength Vs compressive strength

5.6 Modulus of Elasticity

Within the elastic region, the ratio of stress and corresponding strain measures the value of the modulus of elasticity (MoE) of concrete. Since concrete is a brittle material, the addition of steel fibers helps to improve the strength properties, mainly the compression, tension, and flexural strengths, thereby increasing the modulus of elasticity value. The variation of MoE for coconut shell BA fiber reinforced concrete is shown in Figure 19. For the control specimen the MoE was 27.3 GPa which slightly increased to 28.04 GPa with the addition of 10% BA. The silica content in BA helps to improve the paste's strength by forming a dense Calcium-Silicate-Hydrate (C-S-H) region. For the increase in BA content beyond the MoE decreases, which is similar to the compression, tension and flexural strength value. For the addition of fibers, the MoE increase to 29.23 GPa which is about a 7% increase when compared to control mix. The MOE decreased with increasing percentage of gravel replacement with coconut shell for the third series of specimens, namely the fiber-reinforced CS

concrete specimens. For the third series of specimen namely the, fiber reinforced CS concrete specimens, the MoE decrease with the increase in the percentage of replacement of gravel with coconut shell. For 10%, 20%, 30%, 40% and 50% CS fiber reinforced concrete the MoE value was 27.1 GPa, 25.4 GPa, 24.2 GPa, 23.1 GPa and 21.2 GPa respectively. The voids in the concrete mix increase with the amount of CS, which also reduces the strength of the concrete and thereby the MoE value. The previous research on coconut shell concrete with polypropylene fibers reported an increase in MoE of 8% for 50% addition of fiber volume. Which matched well with the present result. Coconut shell concrete with GGBS slag as cement replacement reached a MoE of 8 GPa [44], low value of MoE was due to the absence of fiber reinforcement. Similarly CS concrete with sisal fiber showed a MoE of 16 GPa for 3% addition of sisal fiber [45]. Therefore, it can be concluded that, addition of BA and scrap steel fibers helps to reduce the strain in the concrete for the applied compression load, thereby increasing the Modulus of

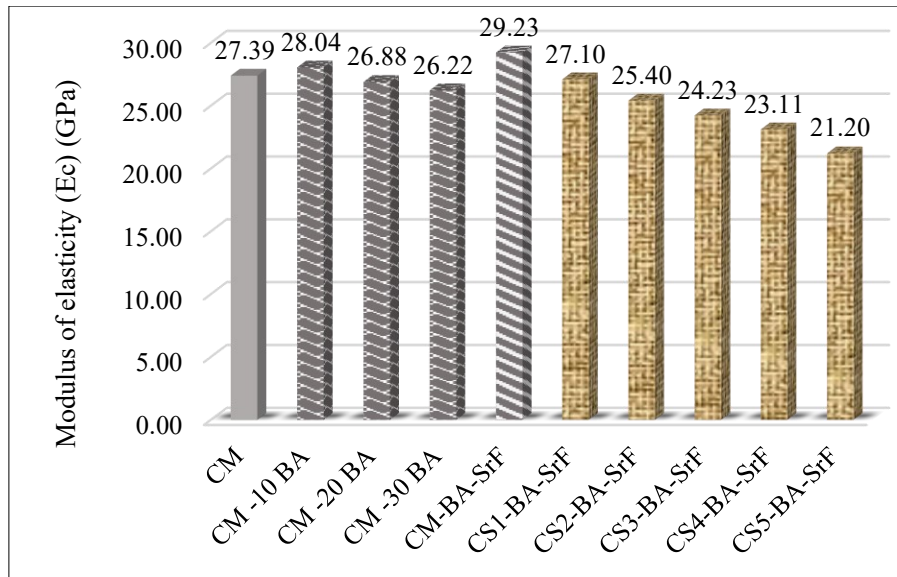


Figure 19. Modulus of elasticity of control, BA concrete and coconut shell scrap steel fiber concrete

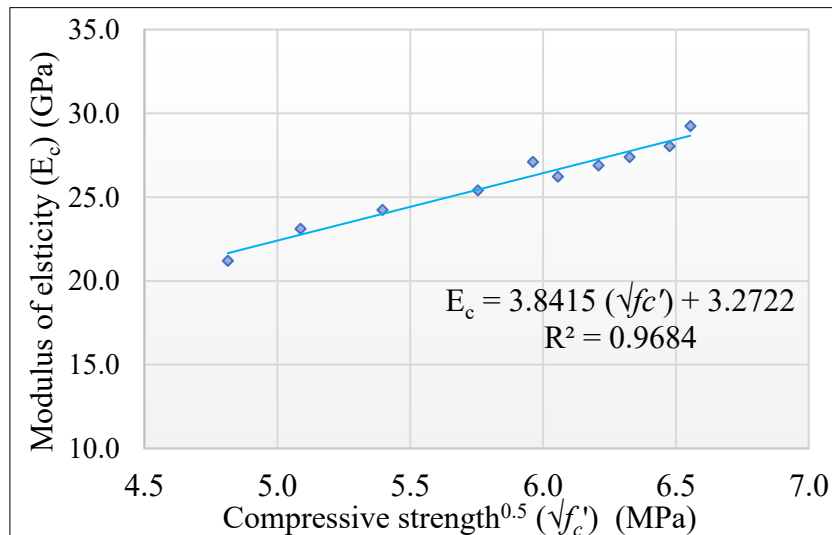


Figure 20. Regression plot of Modulus of elasticity Vs compressive strength

Elasticity. The linear regression plot to develop a correlation between the compressive strength and modulus of elasticity with high regression value ($R^2 = 0.96$) is shown in Figure 20. The developed equation relating modulus of elasticity and compressive strength is given by equation (14). The previous research equation correlating modulus of elasticity with the compressive strength of sisal fiber reinforced coconut shell concrete[43] is given by equation (15) and the equation predicted by Concrete Structural Design Standard Specification (CSDS) is given by equation (16) respectively. The established relationship corresponds well to the previous researchers' and standard specifications.

$$E_{c(SrF)} = 0.384f_c^{0.5} \quad (14)$$

$$E_{c(SIF)} = 0.0307w^{1.5}f_c^{0.5} \quad (15)$$

$$E_{c(CSDS)} = 0.77w^{1.5}f_c^{1/3} \quad (16)$$

6 Conclusion

The following conclusions can be drawn from the experimental investigation into the fresh and mechanical properties of coconut shell bagasse ash scrap steel fibre reinforced concrete:

- The density of concrete in the control mix (CM) was around 2560 kg/m³, which decreases by 5%, 7%, and 8% for 10%, 20%, and 30% replacement of cement with BA, respectively. Therefore, bagasse ash concrete mix helps to reduce the self-weight of structural concrete. The oven-dry density of coconut shell concrete mixes ranged from 2255 to 1995 kg/m³, with the CS5-BA-SrF mix with 50% CS replacement falling under the category of light weight concrete.

- The slump value recorded for the control mix was 85 mm, which increased with the increase in the percentage of bagasse ash. With the replacement of 10%, 20% and 30% of BA the slump value increases to 89 mm, 90 mm, 92 mm

respectively. The slump value of coconut shell concrete ranged between 73 mm and 45 mm which is due to the irregular shape of CS aggregate.

- The compressive strength of scrap fiber reinforced BA concrete (CM-BA-SrF) showed up to a 2% increase in strength compared to unreinforced mix (CM-10BA). For the coconut shell fiber reinforced concrete, the compressive strength decreases with the increase in coconut shell percentage.

- The splitting tensile strength, flexural strength, and modulus of elasticity values increase with the addition of 10% BA and scrap fiber. For fiber reinforced coconut shell concrete, the strength properties decrease with an increase in the percentage of coconut shell. The reduction in strength properties with the increase in the percentage of coconut shell is due to the density of CS aggregate, the orientation of the aggregate, bond between the aggregate and cement matrix or the thin shape of coconut shell aggregate.

- Fracture of coconut shell aggregate was not identified in any of the tested specimens, which proves that brittle CS aggregate when used as a replacement for conventional aggregate does not have any limitations. Therefore, it can be concluded that, bagasse ash, scrap fiber and coconut shell can be effectively used as replacement materials in concrete to produce a sustainable concrete solution.

- The control mix with up to 10% replacement of cement with bagasse ash helps to develop sustainable concrete with a minor loss in strength. Similarly, coconut shell concrete with up to 30% aggregate replacement can be used effectively for structural applications. Beyond 30% replacement, the strength criteria fall below the minimum strength requirement for structural concrete, and such lightweight concrete can be used for non-load-bearing structural applications.

References

- [1] H. Liu, Q. Li, and S. Ni, "Assessment of the engineering properties of biomass recycled aggregate concrete developed from coconut shells," *Constr. Build. Mater.*, vol. 342, no. PA, p. 128015, 2022, doi: 10.1016/j.conbuildmat.2022.128015.
- [2] R. Prakash, S. N. Raman, C. Subramanian, and N. Divyah, *Eco-friendly fiber-reinforced concretes*. 2021.
- [3] R. Kabir Ahmad, S. Anwar Sulaiman, S. Yusup, S. Sham Dol, M. Inayat, and H. Aminu Umar, "Exploring the potential of coconut shell biomass for charcoal production," *Ain Shams Eng. J.*, vol. 13, no. 1, p. 101499, 2022, doi: 10.1016/j.asej.2021.05.013.
- [4] G. Athira and A. Bahurudeen, "Rheological properties of cement paste blended with sugarcane bagasse ash and rice straw ash," *Constr. Build. Mater.*, vol. 332, no. April, p. 127377, 2022, doi: 10.1016/j.conbuildmat.2022.127377.
- [5] R. Vijayalakshmi, "Influence of Sphaericus Bacteria on Mechanical Properties of Bagasse-Ash Replaced Concrete," vol. 3, no. 12, pp. 25–29, 2017.
- [6] R. Vijayalakshmi and S. Ramanagopal, "Experimental Investigation Into Banana Fibre Reinforced Lightweight Concrete Masonry Prism Sandwiched with GFRP Sheet," *Civ. Environ. Eng. Reports*, vol. 30, no. 2, pp. 15–31, 2020, doi: 10.2478/ceer-2020-0017.
- [7] R. Prakash, S. N. Raman, N. Divyah, C. Subramanian, C. Vijayaprabha, and S. Praveenkumar, "Fresh and mechanical characteristics of roselle fibre reinforced self-compacting concrete incorporating fly ash and metakaolin," *Constr. Build. Mater.*, vol. 290, p. 123209, 2021, doi: 10.1016/j.conbuildmat.2021.123209.
- [8] R. Sathia and R. Vijayalakshmi, "Fresh and mechanical property of caryota-urens fiber reinforced flowable concrete," *J. Mater. Res. Technol.*, vol. 15, pp. 3647–3662, 2021, doi: 10.1016/j.jmrt.2021.09.126.
- [9] I. O. Oladele, S. O. Adelani, B. A. Makinde-Isola, and T. F. Omotosho, "Coconut/coir fibers, their composites and applications," *Plant Fibers, their Compos. Appl.*, pp. 181–208, 2022, doi: 10.1016/b978-0-12-824528-6.00004-7.
- [10] V. Ramalingam, K. Ramesh, M. Arumugam, and V. Muralidharan, "Effect of natural fish tail palm fiber on the workability and mechanical properties of fiber reinforced concrete," *Gradjevinski Mater. i Konstr.*, vol. 65, no. 1, pp. 7–22, 2022, doi: 10.5937/grmk2201007r.
- [11] Ganesh Babu L, "Investigation on the Mechanical and Morphological Characteristics of Caryota Urens Spadix Fibre Reinforced With Polyester Composites," *J. Balk. Tribol. Assoc.*, vol. 26, no. 8, pp. 128–169, 2020.
- [12] A. Karimipour, M. Ghalehnovi, J. De Brito, and M. Attari, "The effect of polypropylene fibres on the compressive strength, impact and heat resistance of self-compacting concrete," *Structures*, vol. 25, no. December 2019, pp. 72–87, 2020, doi: 10.1016/j.istruc.2020.02.022.
- [13] M. Karamloo, O. Afzali-naniz, and A. Doostmohamadi, "Impact of using different amounts of polyolefin macro fibers on fracture behavior, size effect, and mechanical properties of self-compacting lightweight concrete," *Constr. Build. Mater.*, vol. 250, p. 118856, 2020, doi: 10.1016/j.conbuildmat.2020.118856.
- [14] L. Huang, P. Yin, L. Yan, and B. Kasal, "Behavior of hybrid GFRP-perforated-steel tube-encased concrete column under uniaxial compression," *Composite Structures*, vol. 142, pp. 313–324, 2016, doi: 10.1016/j.compstruct.2016.02.016.
- [15] R. Vijayalakshmi and S. Ramanagopal, "Compression Behaviour of Polypropylene Fibre Reinforced Cellular Light Weight Concrete Masonry Prism," *Civ. Environ. Eng. Reports*, vol. 30, no. 1, pp. 145–160, 2020, doi: 10.2478/ceer-2020-0011.
- [16] T. F. Yuan, J. Y. Lee, K. H. Min, and Y. S. Yoon, "Experimental investigation on mechanical properties of hybrid steel and polyethylene fiber-reinforced no-slump high-strength concrete," *Int. J. Polym. Sci.*, vol. 2019, 2019, doi: 10.1155/2019/4737384.
- [17] R. Prakash, N. Divyah, S. Srividhya, S. Avudaiappan, and M. Amran, "Effect of Steel Fiber on the Strength and Flexural Characteristics of Coconut Shell Concrete Partially Blended with Fly Ash," pp. 1–22, 2022.
- [18] S. Mahdi, M. S. M. Ali, A. H. Sheikh, M. Elchalakani, and T. Xie, "An investigation into the feasibility of normal and fibre-reinforced ultra-high performance concrete multi-cell and composite sandwich panels," *J. Build. Eng.*, vol. 41, no. October 2020, p. 102728, 2021, doi: 10.1016/j.jobbe.2021.102728.
- [19] K. Gunasekaran, P. S. Kumar, and M. Lakshmiopathy, "Mechanical and bond properties of coconut shell concrete," *Constr. Build. Mater.*, vol. 25, no. 1, pp. 92–98, 2011, doi: 10.1016/j.conbuildmat.2010.06.053.
- [20] K. Gunasekaran, R. Annadurai, and P. S. Kumar, "Long term study on compressive and bond strength of coconut shell aggregate concrete," *Constr. Build. Mater.*, vol. 28, no. 1, pp. 208–215, 2012, doi: 10.1016/j.conbuildmat.2011.08.072.

- [21] K. Gunasekaran, R. Annadurai, and P. S. Kumar, "Plastic shrinkage and deflection characteristics of coconut shell concrete slab," *Constr. Build. Mater.*, vol. 43, pp. 203–207, 2013, doi: 10.1016/j.conbuildmat.2013.02.019.
- [22] K. Gunasekaran, R. Annadurai, and P. S. Kumar, "Study on reinforced lightweight coconut shell concrete beam behavior under shear," *Mater. Des.*, vol. 50, no. May, pp. 293–301, 2013, doi: 10.1016/j.matdes.2013.03.022.
- [23] K. Gunasekaran, R. Annadurai, S. P. Chandar, and S. Anandh, "Study for the relevance of coconut shell aggregate concrete non-pressure pipe," *Ain Shams Eng. J.*, vol. 8, no. 4, pp. 523–530, 2017, doi: 10.1016/j.asej.2016.02.011.
- [24] K. Gunasekaran, R. Annadurai, and P. S. Kumar, "A study on some durability properties of coconut shell aggregate concrete," *Mater. Struct. Constr.*, vol. 48, no. 5, pp. 1253–1264, 2015, doi: 10.1617/s11527-013-0230-2.
- [25] T. C. Herring, J. N. Thuo, and T. Nyomboi, "Engineering and Durability Properties of Modified Coconut Shell Concrete," *Civ. Eng. J.*, vol. 8, no. 2, pp. 362–381, 2022, doi: 10.28991/CEJ-2022-08-02-013.
- [26] S. N. R. R. Prakash, R. Thenmozhi, "Mechanical characterisation and flexural performance of eco-friendly concrete produced with fly ash as cement replacement and coconut shell coarse aggregate," *Int. J. Environ. Sustain. Dev.*, vol. 18, no. 2, 2019.
- [27] S. Gupta, P. Krishnan, A. Kashani, and H. W. Kua, "Application of biochar from coconut and wood waste to reduce shrinkage and improve physical properties of silica fume-cement mortar," *Constr. Build. Mater.*, vol. 262, p. 120688, 2020, doi: 10.1016/j.conbuildmat.2020.120688.
- [28] A. Sekar and G. Kandasamy, "Study on durability properties of coconut shell concrete with coconut fiber," *Buildings*, vol. 9, no. 5, 2019, doi: 10.3390/buildings9050107.
- [29] A. Kanojia and S. K. Jain, "Performance of coconut shell as coarse aggregate in concrete," *Constr. Build. Mater.*, vol. 140, pp. 150–156, 2017, doi: 10.1016/j.conbuildmat.2017.02.066.
- [30] W. Aziz *et al.*, "Mechanical properties, drying shrinkage and structural performance of coconut shell lightweight concrete," *Structures*, vol. 35, no. February 2021, pp. 26–35, 2022, doi: 10.1016/j.istruc.2021.10.092.
- [31] O. M. Ikumapayi, E. T. Akinlabi, J. D. Majumdar, and S. A. Akinlabi, *Applications of coconut shell ash/particles in modern manufacturing: a case study of friction stir processing*. LTD, 2020.
- [32] E. O. Momoh and A. I. Osofero, "Behaviour of oil palm broom fibres (OPBF) reinforced concrete," *Constr. Build. Mater.*, vol. 221, pp. 745–761, 2019, doi: 10.1016/j.conbuildmat.2019.06.118.
- [33] O. Joshua *et al.*, "Data on the pozzolanic activity in coconut shell ash (CSA) for use in sustainable construction," *Data Br.*, vol. 18, pp. 1142–1145, 2018, doi: 10.1016/j.dib.2018.03.125.
- [34] T. C. Herring, T. Nyomboi, and J. N. Thuo, "Ductility and cracking behavior of reinforced coconut shell concrete beams incorporated with coconut shell ash," *Results Eng.*, vol. 14, no. February, p. 100401, 2022, doi: 10.1016/j.rineng.2022.100401.
- [35] R. Prakash, R. Thenmozhi, S. N. Raman, C. Subramanian, and N. Divyah, "Mechanical characterisation of sustainable fibre-reinforced lightweight concrete incorporating waste coconut shell as coarse aggregate and sisal fibre," *Int. J. Environ. Sci. Technol.*, vol. 18, no. 6, pp. 1579–1590, 2021, doi: 10.1007/s13762-020-02900-z.
- [36] R. Prakash, R. Thenmozhi, S. N. Raman, and C. Subramanian, "Characterization of eco-friendly steel fiber-reinforced concrete containing waste coconut shell as coarse aggregates and fly ash as partial cement replacement," *Struct. Concr.*, vol. 21, no. 1, pp. 437–447, 2020, doi: 10.1002/suco.201800355.
- [37] R. Prakash, R. Thenmozhi, S. N. Raman, and C. Subramanian, "Fibre reinforced concrete containing waste coconut shell aggregate, fly ash and polypropylene fibre," *Rev. Fac. Ing. Univ. Antioquia*, no. 94, pp. 33–42, 2019, doi: 10.17533/10.17533/udea.redin.20190403.
- [38] M. Jahanzaib Khalil, M. Aslam, and S. Ahmad, "Utilization of sugarcane bagasse ash as cement replacement for the production of sustainable concrete – A review," *Constr. Build. Mater.*, vol. 270, p. 121371, 2021, doi: 10.1016/j.conbuildmat.2020.121371.
- [39] H. Bari, M. Safiuddin, and M. A. Salam, "Microstructure of structural lightweight concrete incorporating coconut shell as a partial replacement of brick aggregate and its influence on compressive strength," *Sustain.*, vol. 13, no. 13, 2021, doi: 10.3390/su13137157.
- [40] V. R. P. Kumar, K. Gunasekaran, and T. Shyamala, "Characterization study on coconut shell concrete with partial replacement of cement by GGBS," *J. Build. Eng.*, vol. 26, no. June, p. 100830, 2019, doi: 10.1016/j.jobbe.2019.100830.
- [41] H. Bari, M. A. Salam, and M. Safiuddin, "Fresh and hardened properties of brick aggregate concrete including coconut shell as a partial replacement of coarse aggregate," *Constr. Build. Mater.*, vol. 297, p. 123745, 2021, doi: 10.1016/j.conbuildmat.2021.123745.
- [42] S. Prakash Chandar, K. Gunasekaran, K. S. Satyanarayanan, and R. Annadurai, "Study on some durability properties of coconut shell concrete with quarry dust," *Eur. J. Environ. Civ. Eng.*, vol. 24, no. 6, pp. 709–723, 2020, doi: 10.1080/19648189.2017.1418435.
- [43] R. Prakash, R. Thenmozhi, S. N. Raman, C. Subramanian, and N. Divyah, "Mechanical characterisation of sustainable fibre-reinforced lightweight concrete incorporating waste coconut shell as coarse aggregate and sisal fibre," *Int. J. Environ. Sci. Technol.*, 2020, doi: 10.1007/s13762-020-02900-z.
- [44] A. Jaya Prithika and S. K. Sekar, "Mechanical and fracture characteristics of Eco-friendly concrete produced using coconut shell, ground granulated blast furnace slag and manufactured sand," *Constr. Build. Mater.*, vol. 103, pp. 1–7, 2016, doi: 10.1016/j.conbuildmat.2015.11.035.
- [45] R. Prakash, R. Thenmozhi, S. N. Raman, C. Subramanian, and N. Divyah, "Mechanical characterisation of sustainable fibre-reinforced lightweight concrete incorporating waste coconut shell as coarse aggregate and sisal fibre," *Int. J. Environ. Sci. Technol.*, pp. 1–16, 2020, doi: 10.1007/s13762-020-02900-z.



Technical paper

Numerical thermal performance analysis of light steel insulated walls under fire

Mohammed Hassoune^{*1)}, Abdelhak Kada²⁾, Belkacem Menadi³⁾, Belkacem Lamri⁴⁾¹⁾ Laboratory of Geo-Materials and Civil Engineering, Department of Civil Engineering, University of Blida1, P.O.Box 270 Soumaa Road, Blida, Algeria¹⁾ Laboratory Fire Safety Engineering of Constructions and Protection of their Environment LISICPE, Department of Civil Engineering, Hassiba Benbouali University of Chlef, B.P 78C N19 Road Ouled Fares, Chlef, Algeria²⁾ Laboratory of Geo-Materials and Civil Engineering, Department of Civil Engineering, University of Blida1, P.O.Box 270 Soumaa Road, Blida, Algeria³⁾ Laboratory Fire Safety Engineering of Constructions and Protection of their Environment LISICPE, Department of Civil Engineering, Hassiba Benbouali University of Chlef, B.P 78C N19 Road Ouled Fares, Chlef, Algeria

Article history

Received: 05 November 2022

Received in revised form:

07 February 2023

Accepted: 14 February 2023

Available online: 30 March 2023

Keywords

Light Steel Walls,
Cavity Insulations,
Cold Formed Section,
Fire ISO 834,
Numerical Simulations,
Thermal Performance

ABSTRACT

Light-gauge steel-framed (LSF) walls are being adopted by the Algerian construction industry as a new alternative to the traditional infilled frames due to the advantages they provide. The strength-to-weight ratio of Cold Formed Section (CFS) leads to lighter structures and a decrease in the building cost. However, in the case of fire, the high shape factor combined with the loss of material properties of the unprotected, slender CFS can result in structural failure. Because of their conductivity, elevated temperatures have an effect on the thermal performance of panels, necessitating the use of appropriate insulation. The purpose of this paper is to perform a numerical analysis of the thermal behavior of LSF walls protected by plasterboard or magnesium oxide board, as well as cavity insulations. Numerical models are developed, using ANSYS software to simulate the thermal performance of LSF walls under ISO 834 fire. Thermal simulations are done to predict temperature profiles, maximum temperatures, and the estimated fire resistance level (FRL). This research has produced results to better evaluate the influence of different systems of protection and insulation used for the CFS under fire.

1 Introduction

Nowadays, the use of a Light Gauge Steel Framed (LSF) wall system as a new type of structural element is benefiting the rapid expansion of building construction in Algeria. The ease of transportation and rapidity of execution have made it possible to adopt it as a new alternative building solution, especially in seismic regions, to reduce the weight of the structure. These wall systems consist of two elements of cold-formed steel (CFS), namely stud and track sections characterized by very thin sections which may restrict the use of the LSF for a non-load-bearing wall. These slender sections have better durability and a higher strength-to-weight ratio compared to hot rolled steel [1], due to the different fabrication processes that have a significant influence on mechanical material properties [2]. In a fire situation, steel material having a high thermal conductivity is vulnerable due to the loss of its mechanical properties [3, 4]. Therefore, a fire safety must be ensured as one of the important requirements that a building has to include according to contemporary technical rules on structural engineering [5]. To study the collapse of structures under elevated temperatures, most research has been done on

unprotected hot-rolled structural elements [6-10] or protected structural elements [11-13]. The structural behaviour of CFS structures under fire is complex and requires substantial, dedicated research on isolated element frames as well as on complete walls and panels. Some studies have proposed various parameters that have a significant influence on the behavior of LSF walls in terms of improving fire resistance by incorporating some protective materials [14]. Different single or double layers of wallboard can be used on both sides of the LSF wall, such as plasterboard, magnesium oxide board (MGO) and Cork [15-19]. Furthermore, using rockwool and glass fiber to form a new composite innovative panel, cavity insulation, or external insulation sandwiched between two layers of protection wallboards, could be achieved [20, 21]. Previous research has been conducted to investigate the thermal performance of LSF walls when subjected to fire, including experimental studies and numerical simulation. According to experimental studies done by Kolarkar and Mahendran [22] and Baleshan and Mahendran [23], the measured temperatures across the composite wall panel show a higher fire performance than the conventionally built non-load-bearing wall models. Keerthan and Mahendran [24], developed a numerical model of a composite LSF wall

^{*} Corresponding author:E-mail address: hassoune.mohammed@etu.univ-blida.dz

panel, protected by double layers of plasterboard and externally insulated under various thicknesses and densities using Eurocode design fire curves [25]. They concluded that using rockwool improved fire resistance significantly more than other insulation, particularly when sandwiched between double plasterboard. Ariyanayagam and Mahendran [26] also conducted an experimental study to investigate the effect of calcium silicate boards and plasterboard on non-load-bearing LSF walls exposed to fire. The results show that both wallboards provided nearly the same thermal response. Ariyanayagam and Mahendran [27] investigated, experimentally and numerically, the influence of cavity insulation on the fire resistance of non-load-bearing and load-bearing LSF walls. Their results allow for the conclusion that the FRL of cavity insulated non-load bearing LSF walls increases by more than 10 minutes, whereas it is significantly reduced for the other walls. Khetata et al. [28] performed full-scale standard fire tests, followed by a thermal modelling of composite non-load-bearing LSF, using different configurations for several protection materials and insulations. It was concluded that the increase in the number of studs and the thickness of the protection layers will enhance the fire performance, and the use of super-wool insulation provides a higher fire resistance than rockwool. Rajanayagam et al. [29] have conducted a numerical analysis to investigate the thermal performance of LSF walls and study the effect of novel thermal insulation materials. Rahnavard et al. [30] presented a 2D numerical model of heat transfer analysis with the aim of providing a new analytical formulation for the prediction of the temperature evolution within the concrete-filled cold-formed steel section (CF-CFS) when subjected to fire. It is worth mentioning that extensive research has tackled the problem of the behaviour of CFS at ambient temperature, and there is a need for more studies and investigations at elevated temperatures to enhance their fire safety. Most studies that investigated the behaviour of LSF in a fire situation, have been carried out using plasterboard as layer protection, however, the MGO layer protection, recently introduced in Algeria, requires investigation under fire conditions. Besides, there is a need for more research on the fire performance of LSF wall systems built with such layer protection and added cavity insulation within the panels. To understand the thermal response, finite element heat transfer models for different configurations of LSF wall systems exposed to ISO 834 fire have been developed. The results obtained aim to identify

the LSF wall system with improved fire resistance. Four configurations of composite non-load-bearing light steel-framed walls are considered, depending on the type of protection layers and insulations and their position within the steel frame when subjected to elevated temperatures due to fire. The configuration cases are studied for a vertical panel from a compartment of an industrial building in Chlef designed by the FRAMEMETAL group, Figure 1.

Finite element models, using ANSYS APDL, are produced to predict the temperature profiles, maximum temperatures, and the estimated fire resistance level (FRL), taking into account the critical temperature as specified by EN 1993-1-2 [25] for members with Class 4 cross-sections. The influence of different systems of protection and insulation used for the CFS under fire conditions is evaluated.

2 LSF walls and configurations

LSF walls are made from two tracks and seven studs, evenly spaced by 630 mm, with a steel grade of G345, a density of 7850 kg/m³. The geometry details of CFS Lipped Channel (LC) members and dimensions of the frame are presented in Figure 2 and Table 1.

The LSF is protected with 10 mm of different types of external protection and insulation in four configurations, with the aim of studying the influence of the layers of protection. Table 2 lists nine models of wall protection systems under consideration, and technical information about the adopted LSF system is described in the CNERIB document [31]. The first configuration considers three thermal protection models of LSF walls to be analyzed for each type, plasterboard, MGO, and cork with no insulation. The second configuration includes two models that incorporate MGO protection as well as cavity insulation of rockwool and glass fiber within the panel. The third configuration is taken on the basis of the second, with insulations positioned on both sides against LSF wall panels, forming a new composite system. The fourth configuration, considering two models, consists of an external insulation on the exposed side placed between MGO and plasterboard protections. Single plasterboard is used on the unexposed side. In this study, all configurations of LSF wall models are subjected to standard fire testing according to ISO 834.



Figure 1. Structure of light gauge steel panels (ONAPH building Chlef, Algeria)

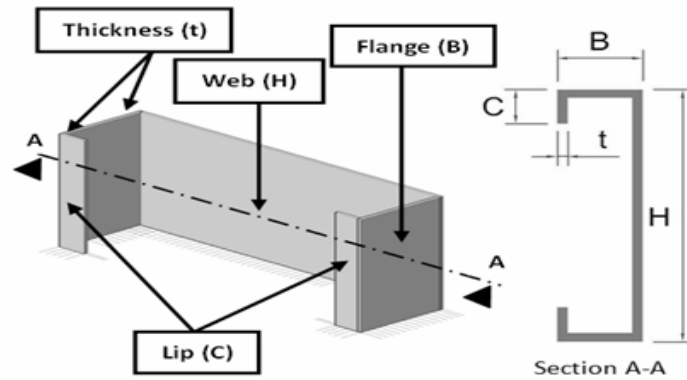
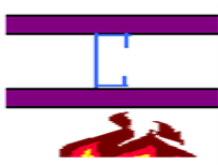





Figure 2. Geometry details of CFS members (LC H x B x C x t)

Table 1. Dimensions of CFS elements of the frame

Profiles	Dimensions				
	H (mm)	B (mm)	C (mm)	t (mm)	L (m)
Truck	152.4	50.8	No lips	1.37	4
Stud	152.4	41.15	12.7	1.37	3.7

Table 2. Details of configurations and models of protection

Configuration	Model	Type of Protection	Insulation
	1	Plasterboard	No Insulation
	2	MGO	
	3	Cork	
	4	MGO	Glass fibre (Cavity - 152.4 mm)
	5		Rockwool (Cavity - 152.4 mm)
	6	MGO	Glass fibre (Sandwiched -75 mm)
	7		Rockwool (Sandwiched-75 mm)
	8	MGO & Plasterboard (In exposed side)	Glass fibre (Sandwiched - 75 mm)
	9	Plasterboard (In unexposed side)	Rockwool (Sandwiched - 75 mm)

3 Thermal properties and heat transfer action on partition LSF walls

3.1 Thermal properties

Thermal properties, conductivity, and specific heat of CFS, as provided by EN 1993-1-2 [25], are illustrated in Figure 3.

The LSF is protected with 10 mm of different types of external protection and insulation in four configurations, considering nine models of protection of wall systems. Thermal properties of the external protection, plasterboard (Figure 4(a)), magnesium oxide board (MGO) Figure 4(b) and cork (Figure 4(c)) are taken from studies developed by Sultan [32], Rusthi et al. [33], and Piloto et al. [34], respectively.

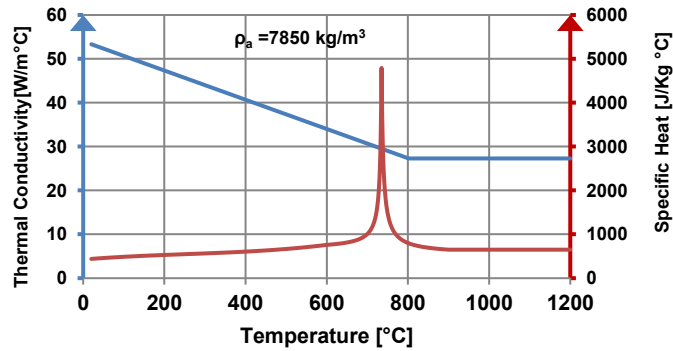


Figure 3. Steel conductivity & specific heat versus temperature

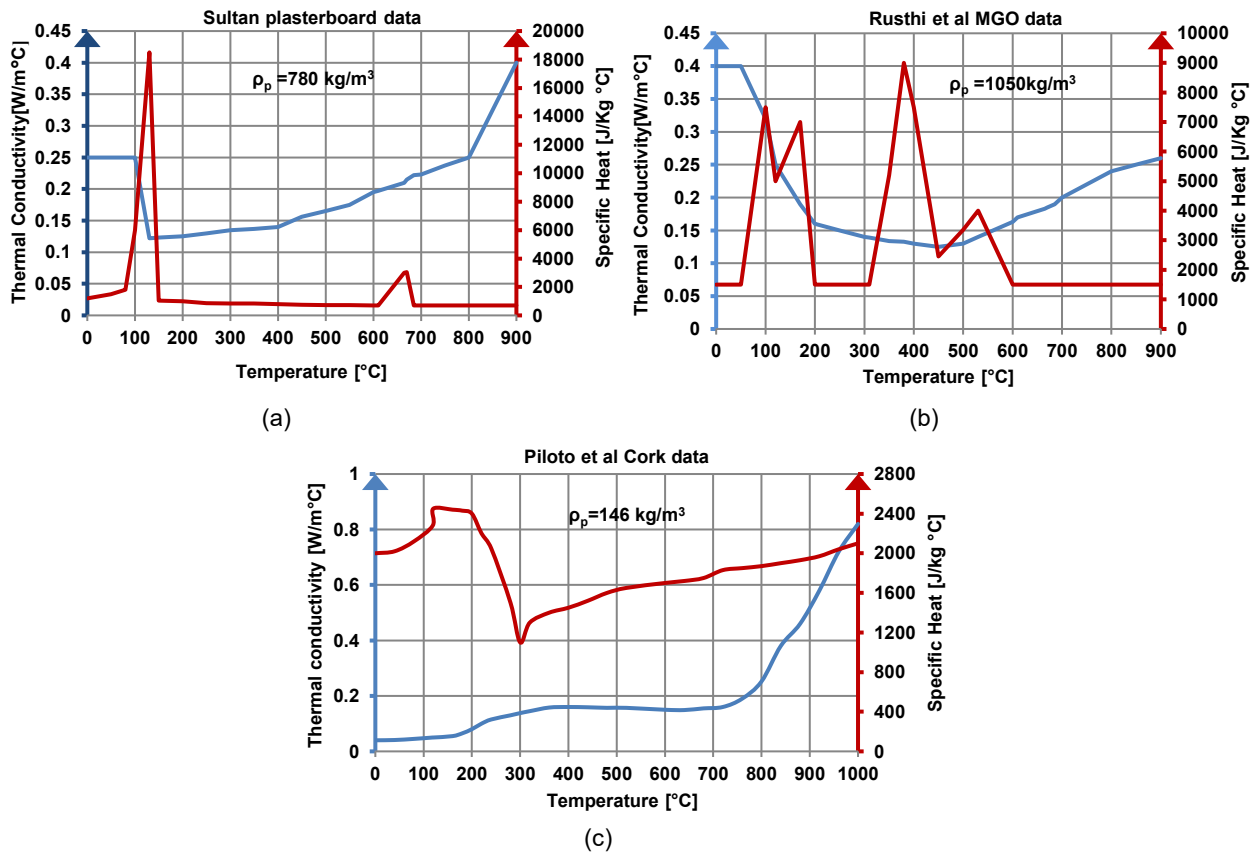


Figure 4. Thermal properties of external protection, (a) Plasterboard, (b) MGO, (c) Cork

The rockwool and glass fibre materials are used as cavity and external insulations. Their properties were obtained from

the study of Lundberg [35] Figure 5(a), and Keerthan and Mahendran [24] Figure 5(b), respectively.

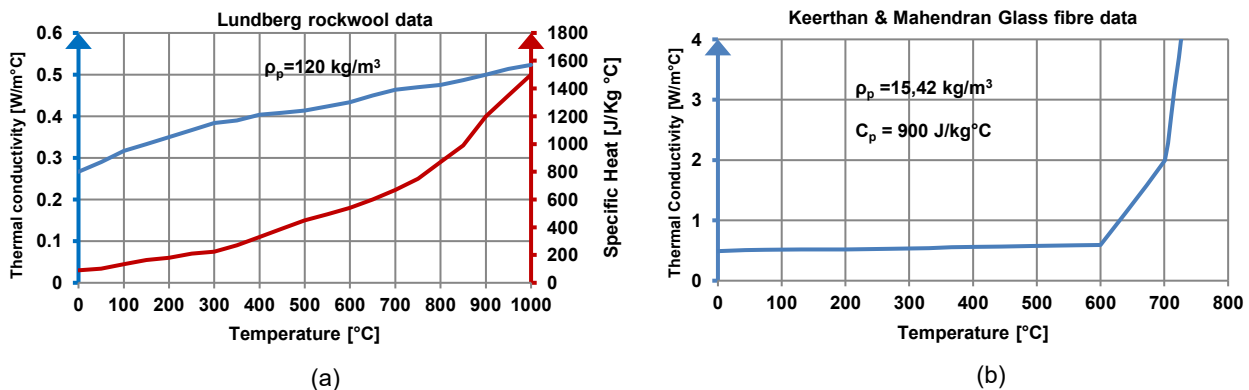


Figure 5. Thermal properties of cavity insulation, (a) Rockwool, (b) Glass fibre

3.2 Heat transfer action on partition LSF walls

The temperature profiles for LSF members are obtained from the nonlinear thermal analysis performed on ANSYS® [36] as a solution of conduction within the steel section governed by the Fourier equation [37], equation (1), using convection and radiation as boundary conditions.

$$\frac{\partial}{\partial x} \left(\lambda_a \frac{\partial \theta}{\partial x} \right) + \frac{\partial}{\partial y} \left(\lambda_a \frac{\partial \theta}{\partial y} \right) + \dot{Q} = \rho_a c_a \frac{\partial \theta}{\partial t} \quad (1)$$

Where λ_a is the thermal conductivity, c_a is the specific heat of steel, ρ_a is the density of steel and \dot{Q} is the energy source equal to zero in the case of a non-combustible element. The fire action is applied in the exposed faces of the materials of protection using ISO 834 equation (2), given in EN1993-1-2 [25].

$$\theta_g = 20 + 345 \log_{10} (8t + 1) \quad (2)$$

Where θ_g is the gas temperature [°C] and t is the time [minutes].

The second solution for the non-linear equation (1) is the simplified method from EN1993-1-2 [25], considering an equivalent uniform temperature during a time interval Δt defined by equation (3a) and equation (3b) for unprotected and protected members, respectively.

$$\Delta\theta_{a,t} = k_{sh} \cdot (A_m / V) \cdot \dot{h}_{net,d} \Delta t / (c_a \cdot \rho_a) \quad (3a)$$

$$\Delta\theta_{a,t} = \frac{\lambda_p \cdot A_p / V \cdot (\theta_g - \theta_m)}{d_p \cdot c_a \cdot \rho_a (1 + \phi/3)} \Delta t - (e^{\phi/3} - 1) \cdot \Delta\theta_{g,t} \quad (3b)$$

Where k_{sh} is the correction factor for the shadow effect, A_m/V and A_p/V are the section factors for unprotected steel members and those insulated by fire protection material, respectively, λ_p , c_p , ρ_p and d_p are the thermal conductivity, specific heat, density, and thickness of the fire protection material, respectively, $\dot{h}_{net,d}$ is the design value of the net heat flux due to convection and radiation per unit area evaluated according to equation (4).

$$\dot{h}_{net,d} = \alpha_c (\theta_g - \theta_m) + \phi \varepsilon_r \sigma [(\theta_g + 273)^4 - (\theta_m + 273)^4] \quad (4)$$

Where α_c is the convection heat transfer coefficient, $\varepsilon_r = \varepsilon_f \varepsilon_m$ with ε_r the emissivity coefficient of the surface of the element equal to 0.7 and ε_f equal to 1 in case of fire, σ is constant of Stefan–Boltzmann ($\sigma = 5.67 \times 10^{-8} \text{ W/m}^2 \cdot \text{K}^4$), θ_m is the surface element temperature, and θ_g is the gas temperature, ϕ is the configuration factor equal to 1 for

unprotected members and obtained according to equation (5) for protected members.

$$\phi = \frac{c_p \cdot \rho_p \cdot d_p \cdot A_p / V}{c_a \cdot \rho_a} \quad (5)$$

4 Thermal analysis models

This part describes the thermal finite element models used for all simulations performed for LSF walls in order to investigate their thermal response and predict their temperature profiles, maximum temperatures, and fire resistance level (FRL). Appropriate mesh is adopted, and thermal boundary conditions of convection and radiation are applied for CFS elements and protection materials.

4.1 Thermal FE models

Finite element analyses were conducted under transient and nonlinear thermal analyses, based on SHELL131 and SOLID70 elements for CFS members and external protections and insulations, respectively. The contact between solids and shells is considered perfect. Figure 6 shows the geometry and the topology of these finite elements. The latter are used with linear interpolating functions and full integration methods from ANSYS® [36]. SHELL 131 has four nodes with up to 32 degrees of freedom at each node. It is a three-dimensional layered shell element with in-plane and through-thickness thermal conduction capability that is suitable for transient thermal analysis. SOLID 70 has eight nodes and a single degree of freedom, temperature, at each node applicable to a 3-D, steady-state, or transient thermal analysis.

4.2 Mesh and boundary conditions

The thermal model is meshed by shell and solid finite elements with size of 20 × 50 mm for the web and flanges, and a size of 20 × 20 mm around the circular hole region, with the lip being one single element as shown in Figure 7.

The ISO834 is applied as bulk temperature on the exposed side of the wall according to EN-1991-1-2 [38], with heat transfer by convection having a coefficient of 25 W/m²K. The unexposed side is considered ambient with an applied boundary condition of convection and a film coefficient of 9 W/m²K which include the radiation effect. For the models without cavity insulation, the same boundary conditions are applied, but according to Gunalan [39] an extra radiation is applied to an empty cavity with an emissivity coefficient equal to 0.9 at the cavity surface.

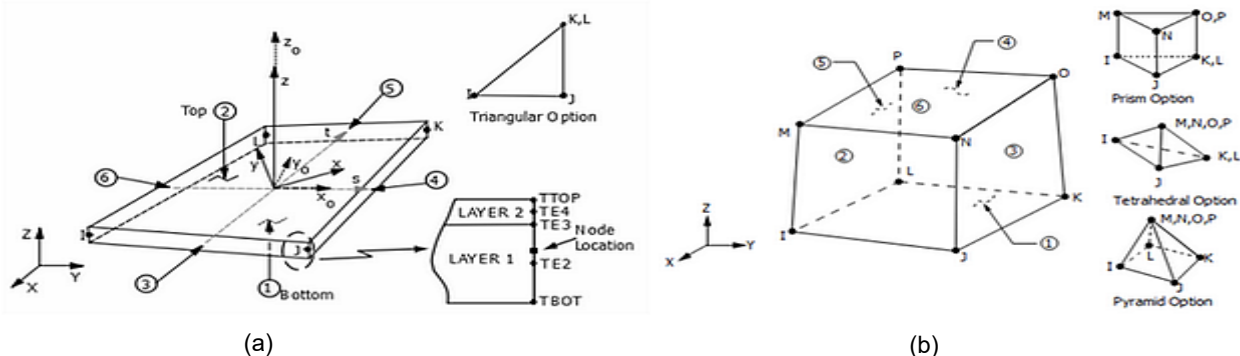


Figure 6. Geometry & topology of finite element models, (a) SHELL131, (b) SOLID70 [36]

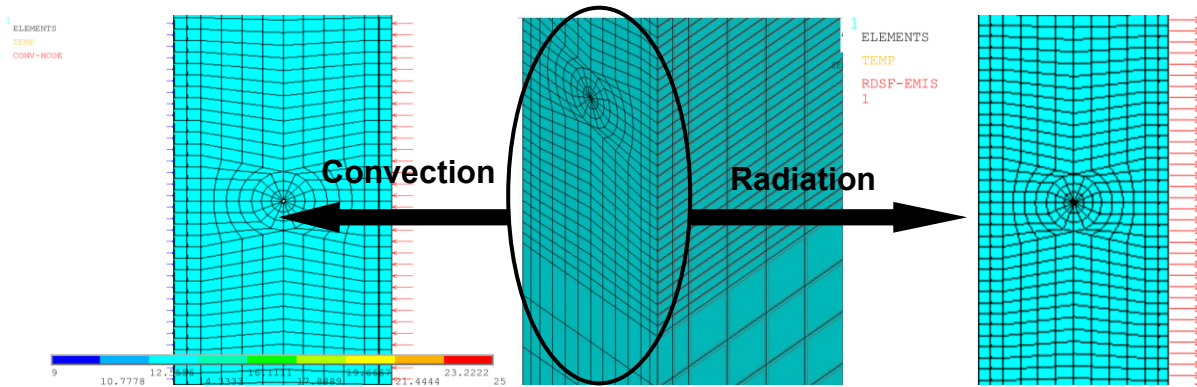


Figure 7. Meshing of the model and Boundary conditions

4.3 Model validation

In this section, a validation of thermal FE models is presented and compared with the fire test result obtained by Rusthi, et al. [33] for the LSF wall system. The test was conducted with 3.15 m × 3.15 m LSF panel of six stiffened channel studs (LC 92 × 35 × 15 × 1.15 mm) equally spaced by 600 mm, and fixed between two tracks at the top and the bottom, and then lined with 10 mm thick of MGO. Figure 8 shows the thermocouples position during the test from which average temperature curves for stud flanges were extracted.

The average temperature evolution of the hot flange (HF) and the cold flange (CF) are presented in Figure 9. The latter shows the comparison between the results of the experimental study and the numerical simulation obtained from the numerical model and highlights a good agreement in temperature profiles within the sections.

5 Results and discussion

Results from simulations produce temperature contours, time-temperature evolution, and fire resistance levels for all configurations in order to investigate the thermal response of the LSF wall and study the effect of different protection materials. The temperature is extracted at the mid-height of the flanges of the middle stud, which are highly exposed to heat on both sides. The temperature evolution for the first configuration is presented for the three thermal models in Figure 10.

It can be observed that a maximum temperature of 564 °C in HF and 458 °C in CF can be reached for model 2 based on the MGO board, which is much lower than those of models 1 and 3. While the model 2 with the MGO board had a slow rise in temperature, the model 3 with the cork lined panel had a rapid rise in temperature. For the later model, the highest temperature in HF is reached for at a maximum

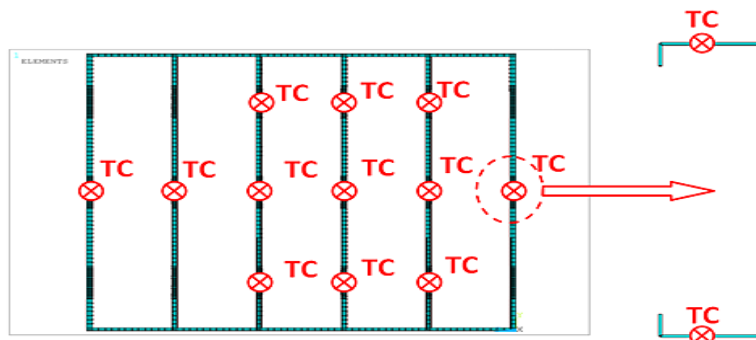


Figure 8. Thermocouple locations on studs [33]

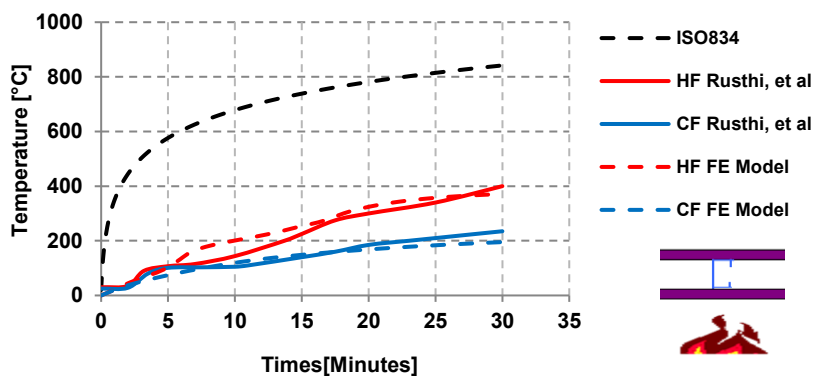


Figure 9. Average temperature evolution of LSF wall from tests and thermal FE analyses

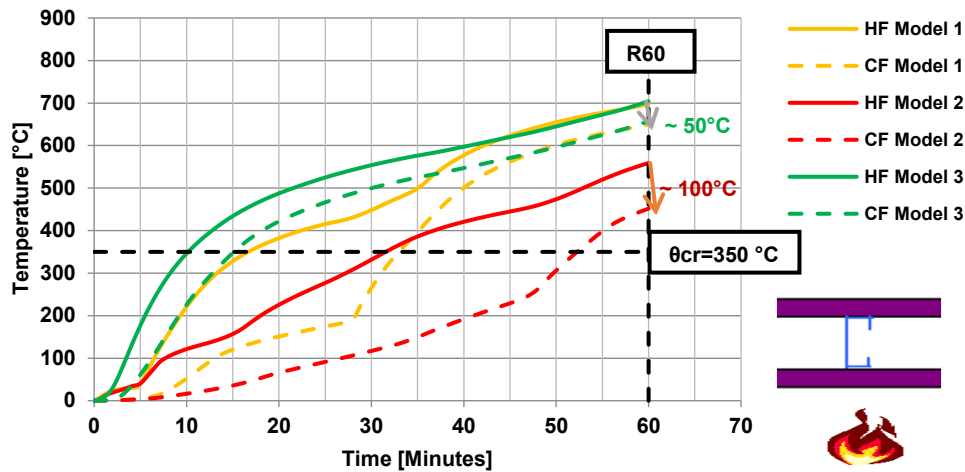


Figure 10. Temperature evolution at mid-height stud of LSF wall (Configuration 1)

of 707 °C, with a temperature difference of 50°C between HF and CF after 60 minutes. Figure 11 shows the temperature contours of the thermal model 2 at 60 minutes.

The second configuration, which comprises thermal models 4 and 5, aims to investigate the effect of the position of cavity insulations within the panel on improving the fire resistance. The temperature evolution shown in Figure 12 shows that the thermal model 4 based on glass fibre insulation has reached a maximum temperature of 732 °C and 188 °C in stud HF and CF, respectively, at 60 minutes.

These temperatures are higher compared to those provided by model 5 based on rockwool insulation, and the temperature difference between HF and CF for models 4 and 5 is 544°C and 620 °C, respectively. Therefore, the presence of the cavity insulation within the panel reduces the heat transfer through the stud cold flange, and leads to a rapid increase in temperature in the stud hot flange. It can be seen that temperatures in HF are higher than the critical temperature, resulting in the failure of studs in the case of a load-bearing wall.

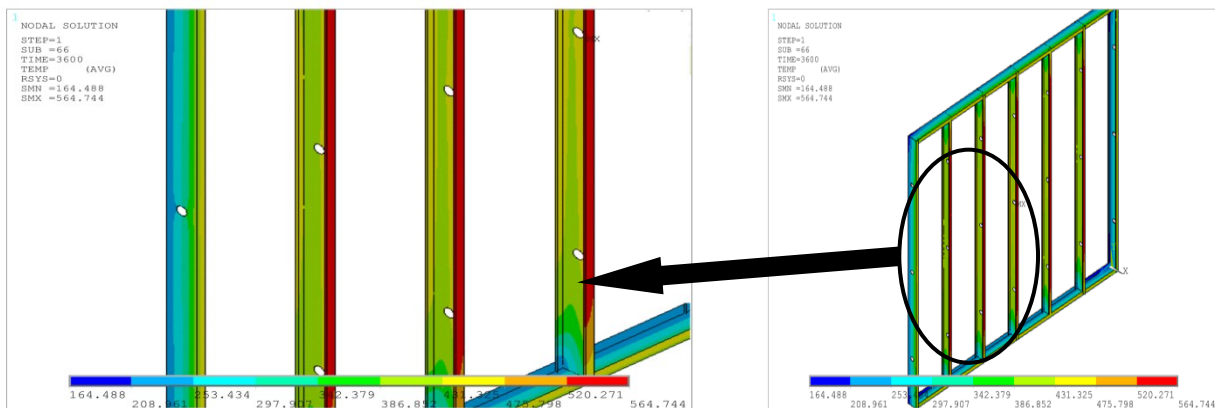


Figure 11. Temperature contours of model 2 at 60 minutes

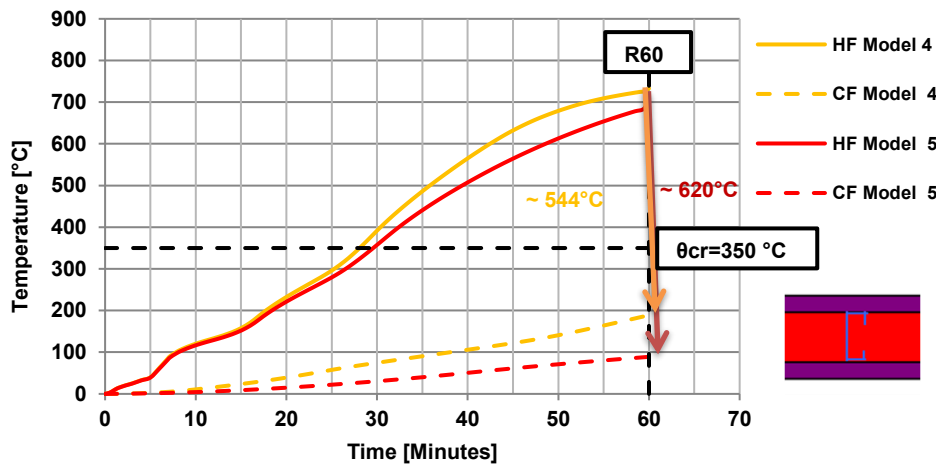


Figure 12. Temperature evolution at mid-height stud of composite LSF (Configuration 2)

Figure 13 shows temperature contours of the thermal model 5 at 60 minutes.

Figure 14 presents the temperature evolution for the third configuration, including the thermal models 6 and 7, which comprise the new composite LSF wall. Temperature progress is slow, with small temperature differences of 64 °C and 22 °C between the studs HF and CF for models 6 and 7, respectively. The maximum temperature does not exceed 120 °C at 60 minutes. The new composite wall system provides better fire performance compared to the traditional LSF wall, either with or without cavity insulation, used in configurations 1 and 2.

Figure 15 shows temperature contours of the thermal model 7 at 60 minutes.

Figure 16 presents results for the temperature evolution of the fourth configuration of models 8 and 9. The temperature difference between HF and CF, the maximum temperature, and the temperature evolution are comparable to those of the third configuration, with slight differences in results.

Figure 17 shows temperature contours of the model 9 at 60 minutes.

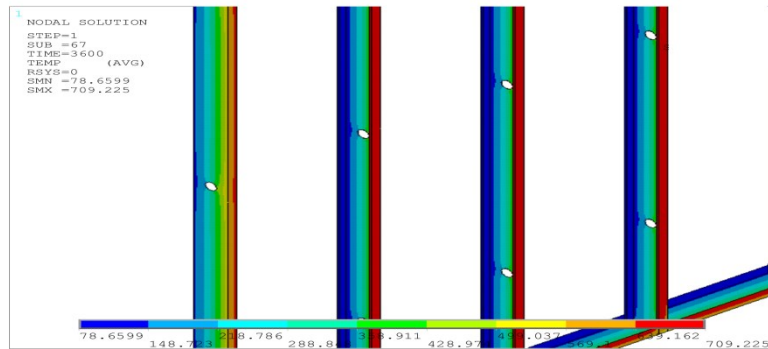


Figure 13. Temperature contours of model 5 at 60 minutes

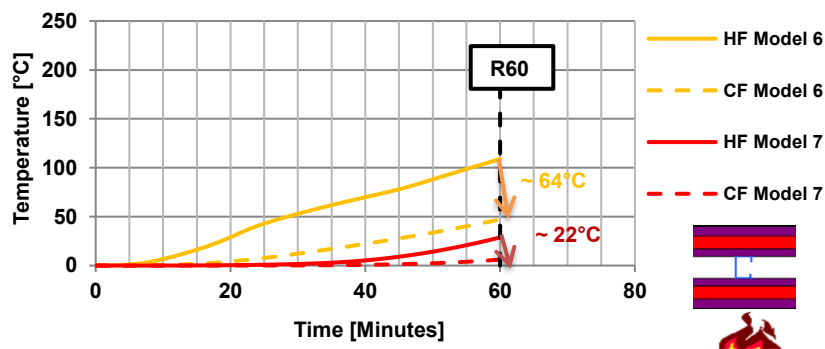


Figure 14. Temperature evolution at mid-height stud of new composite LSF wall (Configuration 3)

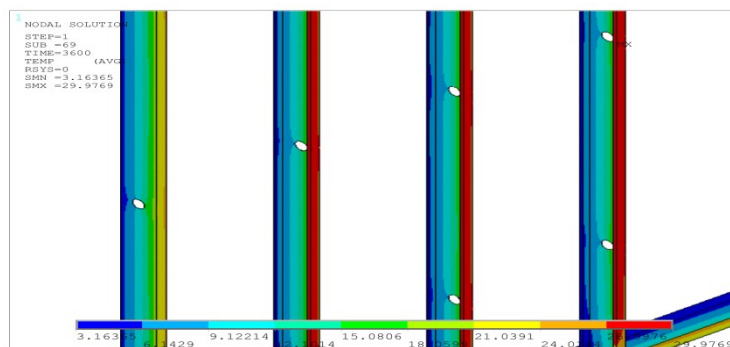


Figure 15. Temperature contours of model 7 at 60 minutes

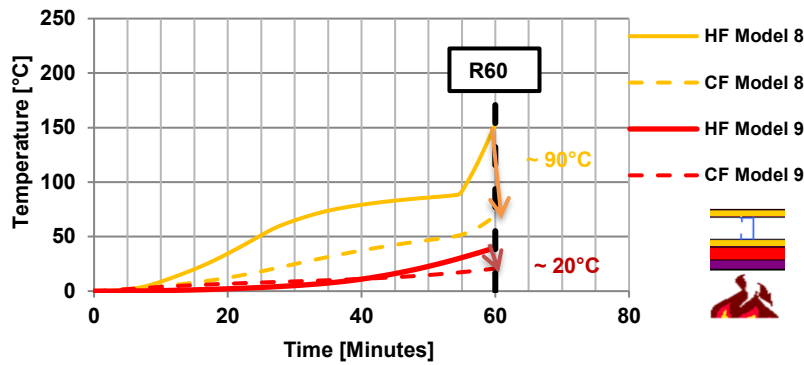


Figure 16. Temperature evolution at mid-height stud of proposed LSF (Configuration 4)

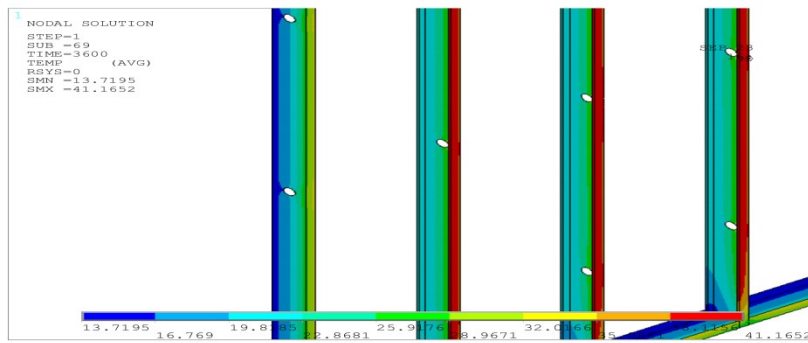


Figure 17. Temperature contours of model 9 at 60 minutes

Table 3 summarizes all the results obtained for all configurations for maximum temperatures, at mid-height of the flanges HF and CF of the most exposed stud at 60 minute.

Table 4 shows the failure time for all thermal models at the critical temperature of 350 °C as specified in EN 1993-1-2 [25], to obtain the fire resistance level (FRL) for each model.

Table 4 shows that the model 2 based on MGO board achieved the highest FRL with a failure time of 31 minutes, which is significantly better than the FRL from models of configuration 1, with failure time differences of 15 minutes for

plasterboard and 20 minutes for cork. The position of cavity insulation within the panel produces approximately the same FRL as obtained from Model 2. In the presence of rockwool and glass fiber insulation, the temperature in HF rapidly rises above the critical temperature. It is observed that the failure time has not been reached for configurations 3 and 4. The FRL could be improved by using insulation externally sandwiched between two layers of protection. The temperature contours of the most exposed middle stud of all panels lined with MGO at the failure time are presented in Figure 18.

Table 3. Maximum temperatures at mid-height of the middle stud

Configuration	Model	Temperature [°C] (at 60 minutes)	
		CF	HF
1	1	650	699
	2	458	564
	3	655	707
2	4	188	732
	5	88	709
3	6	47	111
	7	7	29
4	8	70	159
	9	21	41

Table 4. Fire resistance level (FRL) of non-load bearing LSF walls

Configuration	Model	Fire resistance level (FRL) [Min] (Critical temperature of 350°C, EC3-1-2)
1	1	16
	2	31
	3	10
2	4	28
	5	29
3	6	>60
	7	>60
4	8	>60
	9	>60

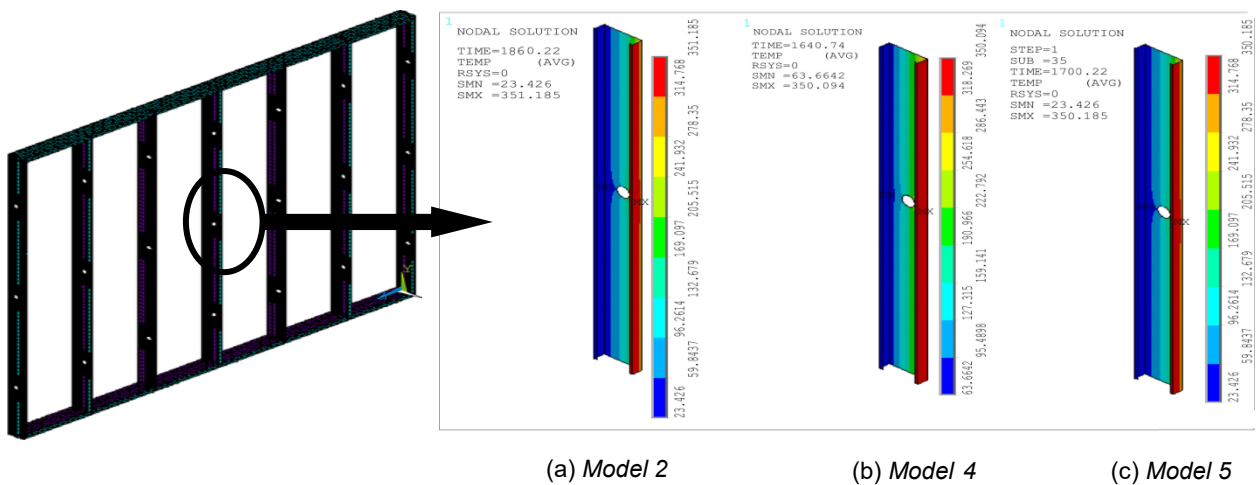


Figure 18. Temperature contours at the failure time of panels lined with MGO

6 Conclusions

A numerical investigation based on the validated finite element model of the thermal response of the LSF wall system under fire, ISO 834, is presented, considering the effect of different protections. The thermal transient analysis with the full option solution method was performed using ANSYS APDL. The numerical heat transfer results of the LSF wall configurations include a time–temperature curve and temperature contours, which are used to study the influence of different systems of protection and insulation on improving the fire resistance. The analysis shows predicted temperatures and fire resistance levels for different configurations, and the following conclusions are drawn:

- In configuration 1, the temperature of 564 °C obtained from stud HF of the protected panel by magnesium oxide board is lower than those of plasterboard and cork, which are 699 °C and 707 °C, respectively.
- Considering the critical temperature of 350 °C specified by EC3, the MGO board leads to an increase in the failure time in comparison with the other two protections by providing a fire resistance level (FRL) of 31 minutes which is much better than the FRLs of plasterboard and cork of 16 minutes and 10 minutes, respectively.
- The presence of cavity insulation within the panel reduces the heat transfer across the stud cold flange, and leads to a rapid increase in temperature in the stud hot flange. This may cause the early failure of the overall panel in the case of a load-bearing wall.

- The failure time of configuration 2 (panels protected by MGO with an insulation cavity) is about the same as configuration 1 (panels protected by MGO without an insulation cavity) at 29 minutes.
- The use of external insulation between two layers of protection forming a composite panel, (configuration 3), presents a higher thermal performance compared to the traditional LSF with/without cavity insulation with more than 60 minutes of FRL.
- The temperatures were very similar in both cases of LSF wall configurations 3 and 4. As a result, configuration 4, with a single sheet of plasterboard on the exposed side and insulation between MGO and plasterboard on the unexposed side, offers a more cost-effective solution for the same thermal performance. Therefore, configuration 4 with a reduced protection system leads to a gain in work time and makes the structure lighter.

Acknowledgments

The authors would like to acknowledge the support of the Directorate General for Scientific Research and Technological Development, DGRSDT, and Ministry of Higher Education and Scientific Research, MESRS, of Algeria. Also, the authors are thankful to FRAMEMETAL SPA for providing the necessary information on the site and documents to conduct this research.

List of symbols

t	Time, [minutes]
C_a, λ_a, ρ_a	Specific heat [J/kg°C], thermal conductivity [W/m°C] and density [kg/m ³] of steel, respectively.
$C_p, \lambda_p, \rho_p, d_p$	Specific heat [J/kg°C], thermal conductivity [W/m°C], density [kg/m ³] and thickness of protection materials [mm], respectively.
k_{sh}	Correction factor for shadow effect
E	Modulus of elasticity, N/mm ²
f_y	Yield strength, N/mm ²
$\dot{h}_{net,d}$	Design value of the net heat flux, w/m ²
\dot{Q}	Energy source
θ_g	Gas temperature in the fire compartment, °C
θ_m	Temperature of the member surface, °C
α_c	Convection heat transfer coefficient, W/m ² K
$\varepsilon_f \varepsilon_m$	Emissivity coefficient,
ϕ	Configuration factor,
σ	Constant of Stefan–Boltzmann, W/m ² ·K ⁴
ν	Poisson's ratio

Subscripts

CFS	Cold Formed Section
LSF	Light gauge Steel Framed
MGO	Magnesium Oxide board
HF	Hot Flange
CF	Cold Flange
TC	Thermocouple

References

- [1] Liang, H., Roy, K., Fang, Z., and Lim, J. B., A critical review on optimization of cold-formed steel members for better structural and thermal performances, Buildings, vol. 12,(2022), 12-34. <https://doi.org/10.3390/buildings12010034>
- [2] Jakovljević, I., Dobrić, J., and Marković, Z., Flexural buckling of hot-finished and cold-formed elliptical hollow section columns: Numerical comparative analysis, Građevinski materijali i konstrukcije, vol. 62,(2019), 15-32. <https://doi.org/10.5937/GRMK1902015J>
- [3] Kada, A., Lamri, B., Mesquita, L., and Bouchair, A., Finite element analysis of steel beams with web apertures under fire condition, Asian Journal Of Civil Engineering (Building And Housing), vol. 17,(2016), 1035-1054.
- [4] Laím, L., Rodrigues, J. P. C., and da Silva, L. S., Experimental analysis on cold-formed steel beams subjected to fire, Thin-Walled Structures, vol. 74,(2014), 104-117. <https://doi.org/10.1016/j.tws.2013.09.006>
- [5] Laban, M. Đ., Radonjanin, V. S., Malešev, M. M., and Radeka, M. M., Construction products performances and basic requirements for fire safety of facades in energy rehabilitation of buildings, Tehnika, vol. 70,(2015), 759-766. <https://doi.org/10.5937/tehnika1505759L>
- [6] Benyettou Oribi, S., Kada, A., Lamri, B., and Mesquita, L. M., Investigation of residual stresses on the fire resistance of unrestrained cellular beams, ce/papers, vol. 4,(2021), 1386-1394. <https://doi.org/10.1002/cepa.1436>
- [7] Kada, A. and Lamri, B., Numerical analysis of non-restrained long-span steel beams at high temperatures due to fire, Asian Journal of Civil Engineering, vol. 20,(2019), 261-267. <https://doi.org/10.1007/s42107-018-0103-7>
- [8] Merouani, M. R., Lamri, B., Kada, A., and Piloto, P., Mechanical analysis of a portal steel frame when subjected to a post-earthquake fire, Fire Research, vol. 3,(2019), 38-43. <https://doi.org/10.4081/fire.2019.76>
- [9] Mesquita, L., Piloto, P., Vaz, M., and Vila Real, P., Experimental and numerical research on the critical temperature of laterally unrestrained steel I beams, Journal of Constructional Steel Research, vol. 61,(2005), 1435-1446. <https://doi.org/10.1016/j.jcsr.2005.04.003>
- [10] Nadjai, A., Petrou, K., Han, S., and Ali, F., Performance of unprotected and protected cellular beams in fire conditions, Construction and Building Materials, vol. 105,(2016), 579-588. <https://doi.org/10.1016/j.conbuildmat.2015.12.150>
- [11] Bailey, C., Indicative fire tests to investigate the behaviour of cellular beams protected with intumescent coatings, Fire safety journal, vol. 39,(2004), 689-709. <https://doi.org/10.1016/j.firesaf.2004.06.007>
- [12] Lamri, B., Mesquita, L., Abdelhak, K., and Piloto, P., Behavior of cellular beams protected with intumescent coatings, Fire Research, vol. 1,(2016), 27-32. <https://doi.org/10.4081/fire.2017.27>
- [13] Mesquita, L., Gonçalves, J., Gonçalves, G., Piloto, P., and Kada, A. Intumescente fire protection of cellular beams, X Congresso de Construção Metálica e Mista, Coimbra, Portugal,(2015).
- [14] Chen, W., Jiang, J., Ye, J., Zhao, Q., Liu, K., and Xu, C., Thermal behavior of external-insulated cold-formed steel non-load-bearing walls exposed to different fire conditions, Structures, vol. 25,(2020), 631-645. <https://doi.org/10.1016/j.istruc.2020.03.044>
- [15] Ariyanayagam, A., Poologanathan, K., and Mahendran, M., Thermal modelling of load bearing cold-formed steel frame walls under realistic design fire conditions, Advanced Steel Construction, vol. 13,(2017), 160-189. <https://doi.org/10.18057/ijasc.2017.13.2.5>
- [16] Balachandren, B., Numerical and experimental studies of cold-formed steel floor systems under standard fire conditions, PhD Thesis, Queensland University of Technology, (2012).
- [17] Piloto, A. G. P., Khetata, S. M., and Gavilán, B. R. A., Fire performance of non-loadbearing light steel framing walls – numerical and simple calculation methods, MATTER: International Journal of Science and Technology, vol. 3,(2017), 13-23. <https://doi.org/10.20319/mijst.2017.32.1323>
- [18] Piloto, P. Light steel framed walls made with composite panels under fire conditions, 6th Conference on Urban Fire Safety and 1st Civil Protection Conference, Universidade de Coimbra- Portugal (2018).
- [19] Rusthi, M. I., Experimental and finite element studies of light-gauge steel frame wall systems under fire conditions, PhD Thesis, Science and Engineering Faculty, Queensland University of Technology, (2017).
- [20] Chen, W., Ye, J., and Zhao, Q., Thermal performance of non-load-bearing cold-formed steel walls under different design fire conditions, Thin-Walled Structures, vol. 143,(2019), 106-242. <https://doi.org/10.1016/j.tws.2019.106242>

- [21] Kolarkar, P. N., Structural and thermal performance of cold-formed steel stud wall systems under fire conditions, PhD Thesis, School of urban development, Queensland University of Technology, Australia, (2010).
- [22] Kolarkar, P. and Mahendran, M., Experimental studies of non-load bearing steel wall systems under fire conditions, *Fire safety journal*, vol. 53,(2012), 85-104. <https://doi.org/10.1016/j.firesaf.2012.06.009>
- [23] Baleshan, B. and Mahendran, M., Numerical study of high strength LSF floor systems in fire, *Thin-Walled Structures*, vol. 101,(2016), 85-99. <https://doi.org/10.1016/j.tws.2015.12.018>
- [24] Keerthan, P. and Mahendran, M., Thermal performance of composite panels under fire conditions using numerical studies: plasterboards, rockwool, glass fibre and cellulose insulations, *Fire Technology*, vol. 49,(2013), 329-356. <https://doi.org/10.1007/s10694-012-0269-6>
- [25] EN1993-1-2, Eurocode 3: Design of steel structures - Part 1-2: General rules - Structural fire design [Authority: The European Union Per Regulation 305/2011, Directive 98/34/EC, Directive 2004/18/EC], (2005), 78.
- [26] Ariyanayagam, A. D. and Mahendran, M., Fire tests of non-load bearing light gauge steel frame walls lined with calcium silicate boards and gypsum plasterboards, *Thin-Walled Structures*, vol. 115,(2017), 86-99. <https://doi.org/10.1016/j.tws.2017.02.005>
- [27] Ariyanayagam, A. D. and Mahendran, M., Influence of cavity insulation on the fire resistance of light gauge steel framed walls, *Construction and Building Materials*, vol. 203,(2019), 687-710. <https://doi.org/10.1016/j.conbuildmat.2019.01.076>
- [28] Khetata, S. M., Piloto, P. A., and Gavilán, A. B., Fire resistance of composite non-load bearing light steel framing walls, *Journal of Fire Sciences*, vol. 38,(2020), 136-155. <https://doi.org/10.1177/0734904119900931>
- [29] Rajanayagam, H., Upasiri, I., Poologanathan, K., Gatheeshgar, P., Sherlock, P., Konthesingha, C., Nagaratnam, B., and Perera, D., Thermal Performance of LSF Wall Systems with Vacuum Insulation Panels, *Buildings*, vol. 11,(2021), 621. <https://doi.org/10.3390/buildings11120621>
- [30] Rahnavard, R., Craveiro, H. D., Simões, R. A., and Santiago, A., Equivalent temperature prediction for concrete-filled cold-formed steel (CF-CFS) built-up column sections (part A), *Case Studies in Thermal Engineering*, vol. 33,(2022), 101928. <https://doi.org/10.1016/j.csite.2022.101928>
- [31] C.N.E.R.I.B, Avis sur système constructif LIGHT GAUGE STEEL, FRAMEMETAL, *Avis Technique 2*, 2016.
- [32] Sultan, M. A., A model for predicting heat transfer through noninsulated unloaded steel-stud gypsum board wall assemblies exposed to fire, *Fire Technology*, vol. 32,(1996), 239-259. <https://doi.org/10.1007/BF01040217>
- [33] Rusthi, M., Ariyanayagam, A., Mahendran, M., and Keerthan, P., Fire tests of Magnesium Oxide board lined light gauge steel frame wall systems, *Fire safety journal*, vol. 90,(2017), 15-27. <https://doi.org/10.1016/j.firesaf.2017.03.004>
- [34] Piloto, P., Khetata, M., and Gavilán, A. B. Fire resistance of non-loadbearing LSF walls, 2nd Conference on Testing and Experimentations in Civil Engineering, Porto, Portugal,(2019).
- [35] Lundberg, S., *Material Aspects of Fire Design, TALAT Lectures* 2502,(1994). <https://www.slideshare.net/corematerials/talat-lecture-2502-material-aspects-of-fire-design> (accessed 17 July 2021).
- [36] ANSYS®, Academic Research, Release 16.2: ANSYS, Canonsburg, PA, USA, 2015.
- [37] Franssen, J.-M. and Vila Real, P., *Fire Design of Steel Structures: Eurocode 1: Actions on structures; Part 1-2: General actions--Actions on structures exposed to fire; Eurocode 3: Design of steel structures; Part 1-2: General rules--Structural fire design* John Wiley & Sons,2012.
- [38] EN-1991-1-2, Eurocode 1: Actions on structures—Part 1-2: General actions—Actions on structures exposed to fire [Authority: The European Union Per Regulation 305/2011, Directive 98/34/EC, Directive 2004/18/EC], British Standards, 2002), 58.
- [39] Gunalan, S., Structural behaviour and design of cold-formed steel wall systems under fire conditions, PhD thesis, Faculty of built environment and engineering, Queensland University of Technology, (2011).



Evaluation of models of the flexural response of rectangular reinforced concrete columns in the post-capping region

Milena Tomić^{*1)}, Anže Babič¹⁾, Tatjana Isaković¹⁾

¹⁾ University of Ljubljana, Faculty of Civil and Geodetic Engineering, Ljubljana, Slovenia

Article history

Received: 05 December 2022

Received in revised form:
30 January 2023

Accepted: 06 February 2023

Available online: 30 March 2023

Keywords

lumped plasticity model;
near-collapse rotation;
trilinear moment–rotation backbone;
quadrilinear moment–rotation backbone;
post-capping stiffness

ABSTRACT

Simulating the seismic behaviour of a structure up to the point of collapse is an established approach to assessing structural safety during strong earthquakes. In the case of reinforced concrete columns with a predominantly flexural response, a lumped plasticity model with a predefined backbone and Takeda hysteresis rules is often used for this purpose. The present study investigates different moment–rotation backbone models to identify procedures that adequately predict the post-capping part of the backbone. In the first part of the paper, Eurocode 8 procedures for estimating the rotation in the near collapse limit state are reviewed and used to calculate the near collapse rotation of two experimentally tested columns with different levels of confinement. The procedure that agrees best with the experiments is used in the second part of the study, where several options for modelling the post-capping part of the moment–rotation backbone are studied. The results suggest that a quadrilinear moment–rotation backbone with a bilinear post-capping region combined with anearcollapse rotation determined according to the empirical procedure from the current version of Eurocode 8/3 can predict the cyclic response of both poorly and well-confined columns.

1 Introduction

The lumped plasticity modelling approach is commonly used to study the seismic performance of reinforced concrete structures. The Giberson lumped plasticity model is often used for reinforced concrete columns with a predominantly flexural response. In this model, the plastic hinge is defined as a rotational spring having an approximate moment–rotation relationship, defined by the backbone and hysteresis rules, such as the Takeda hysteresis rules [1]. This well-established approach has been used for decades to assess the nonlinear response of reinforced concrete structures (e.g. [2, 3, 4, 5]) and is still relevant today, as researchers are looking for simple and effective models to be used in seismic risk assessment studies (e.g. [6, 7, 8]).

Different models for estimating the moment–rotation backbone have been used previously. The parameters defining the response up to the capping point have been successfully estimated, as this part of the backbone has been well studied (e.g. [9, 10]). However, the response after the capping point, characterised by stiffness and strength degradation, is less well studied. This part of the backbone is important in risk assessment studies, where the seismic behaviour of the structure is simulated up to the point of collapse (e.g. [11, 12, 13]). In the recent literature, researchers have suggested modifications to existing backbone models to better describe the post-capping region (e.g. [6, 14, 15]). These models are often consistent with the

backbone as defined in the ASCE/SEI 41 standard [16]. However, the number of studies developing a backbone model consistent with the requirements of the Eurocode standards is more limited.

In the Eurocode 8 standard, the post-capping region is defined by the near collapse (NC) limit state, which is when the flexural strength drops by 20%. Consistent with the code, some studies have defined the moment–rotation backbone in the post-capping region as the NC moment and rotation combined with the assumed post-capping stiffness [17, 18]. The ability to predict the nonlinear response of reinforced concrete elements up to the NC limit state has also been confirmed by the results of pseudodynamic tests (e.g. [19]). However, such a modelling approach is not straightforward, as several different procedures for calculating the NC limit state rotation are included in Eurocode 8. In addition, there are no guidelines for defining the post-capping part of the backbone based on the NC rotation. Several modelling strategies have been proposed. Although most studies predict constant post-capping stiffness [17, 20, 21, 22], some recommend that this part of the backbone should be modelled as bilinear (e.g. [14, 23, 24]).

The present study addresses the lack of guidelines for defining the post-capping part of the moment–rotation backbone consistently with the Eurocode standards. In particular, the aim of the study is to identify a reliable

* Corresponding author:

E-mail address: Milena.Tomic@fgg.uni-lj.si

Eurocode-conforming backbone model that could be used to simulate the post-capping response of rectangular reinforced concrete columns with a predominantly flexural response up to the point of collapse, regardless of the column design level. In the first part of the paper, Eurocode 8 procedures for assessing the NC limit state rotation are reviewed (Section 2) and evaluated against the results of experiments on two rectangular reinforced concrete columns with different levels of confinement (Section 3). The procedure that agreed best with the experiments on both columns is used in the second part of the study (Section 4), where several different models of the moment–rotation backbone are studied and compared to the experimentally obtained cyclic response.

2 Estimation of the NC limit state according to Eurocode 8

Eurocode 8 defines the onset of limit states of reinforced concrete columns by their chord rotations. The chord rotation corresponding to the NC limit state is referred to as the "ultimate chord rotation" in Eurocode 8 (in this paper, the "NC rotation") and can be determined using different procedures. These procedures are first briefly summarised in Subsection 2.1 and then presented in more detail in Subsections 2.2, 2.3 and 2.4. In Subsection 2.2, the material parameters for section analysis are summarised, Subsection 2.3 covers the estimation of the plastic hinge length, and Subsection 2.4 covers the NC rotation calculation.

2.1 Summary of Eurocode 8 procedures

This study considered five Eurocode 8 procedures for assessing the NC rotation of reinforced concrete columns (Table 1). The procedures included in Eurocode 8/3 [25], Eurocode 8/2 [26], and Eurocode 8/1 [27] were considered.

Two procedures in the current Eurocode 8/3 (denoted as EC8/3a&EC2 and EC8/3a) are categorised as analytical, requiring the assessment of the ultimate curvature using section analysis, while the third procedure (denoted as EC8/3b) is semi-empirical; section analysis is not needed. The EC8/3a&EC2 procedures follow the requirements of Eurocode 2 [28] when performing section analysis, while EC8/3a follows the rules included in Eurocode 8/3. The analytical and empirical procedures differ regarding the required data. The analytical procedures require an advanced definition of the materials and an estimate of the plastic hinge length. These data are not needed in the empirical approach.

The procedure included in Eurocode 8/2 (denoted as EC8/2) is also analytical. It is similar to the analytical procedures from Eurocode 8/3 but uses different assumptions for section analysis and plastic hinge length.

The procedure from the draft of the new Eurocode 8/1 (denoted as prEC8/1) combines the analytical and empirical approaches. The yield rotation is estimated by performing section analysis, while the ultimate (NC) rotation is estimated using a semi-empirical approach. This procedure is specified only for rectangular cross-sections. For other types of cross-sections not investigated in this study, the new Eurocode 8/1 prescribes an analytical approach.

2.2 Material parameters and section analysis

The analytical approaches require the estimation of yield and ultimate curvatures as input data for calculating the NC rotation (Table 1). They are defined by section analysis. Section analysis is typically performed by discretizing the cross-section into fibres associated with the corresponding materials: unconfined concrete cover, confined concrete core, and longitudinal reinforcement steel. While the constitutive law of unconfined concrete is the same for all procedures considered in this study, the constitutive law of confined concrete varies from procedure to procedure (Table 2). The constitutive laws for longitudinal reinforcement steel (Table 3) also differ, mainly regarding the value of the ultimate strain considered.

In general, procedure prEC8/1 requires section analysis only to determine the yield curvature (for yield rotation calculation), because the post-yield response is determined empirically. Moreover, the new Eurocode 8/1 distinguishes between two cases: failure of the section before and after the concrete cover spalling.

In order to determine which case governs the response, the section analysis should be initially performed assuming that the section failure occurs after the spalling of the concrete cover. The flexural resistance of the concrete core, defined as the moment corresponding to the ultimate strain in the confined core or longitudinal reinforcement, should then be compared to the total flexural resistance. The latter is determined as the maximum moment that developed before the spalling of the concrete cover. If the flexural resistance of the concrete core is higher than 80 % of the total flexural resistance, the assumption that the section fails after the spalling is confirmed. Otherwise, the section analysis should be repeated with different ultimate strains, as defined by Eqs. (15) and (20).

Table 1. Requirements of the Eurocode 8 procedures for NC rotation calculation

Procedure	Approach	Section analysis	Advanced material definition ($f_{cc}, \epsilon_{cc}, \epsilon_{uc}, \epsilon_{sw}, \dots$)	Plastic hinge length estimation
EC8/3a&EC2	Analytical	Yes	Yes	Yes
EC8/3a	Analytical	Yes	Yes	Yes
EC8/3b	Empirical	No	No	No
EC8/2	Analytical	Yes	Yes	Yes
prEC8/1	Combined	Yes	Yes	No

Table 2. Summarised Eurocode procedures for the definition of the confined concrete constitutive laws

Procedure	Equations
EC8/3a&EC2	$f_{cm,c} = \begin{cases} f_{cm} \cdot \left(1 + 5 \frac{\sigma_2}{f_{cm}}\right), & \text{if } \sigma_2 \leq 0.05 f_{cm} \\ f_{cm} \cdot \left(1.125 + 2.5 \frac{\sigma_2}{f_{cm}}\right), & \text{if } \sigma_2 > 0.05 f_{cm} \end{cases} \quad (1)$
	$\varepsilon_{c2,c} = \varepsilon_{c2} \left(\frac{f_{cm,c}}{f_{cm}}\right)^2 \quad (2)$
	$\varepsilon_{cu2,c} = \varepsilon_{cu2} + 0.2 \frac{\sigma_2}{f_{cm}} \quad (3)$
	$\sigma_2 = \alpha \cdot \rho_{sx} \cdot f_{yw} \quad (4)$
EC8/3a	$f_{cm,c} = f_{cm} \cdot \left(1 + 0.37 \left(\frac{\sigma_2}{f_{cm}}\right)^{0.86}\right) \quad (5)$
	$\varepsilon_{c2,c} = \varepsilon_{c2} \left(1 + 5 \left(\frac{f_{cm,c}}{f_{cm}} - 1\right)\right) \quad (6)$
	$\varepsilon_{cu2,c} = 0.004 + 0.5 \frac{\sigma_2}{f_{cm,c}} \quad (7)$
	$\sigma_2 = \alpha \cdot (\min(\rho_{wy}; \rho_{wz})) \cdot f_{yw} \quad (8)$
EC8/2	$f_{cm,c} = f_{cm} \cdot \left(2.254 \sqrt{1 + 7.94 \frac{\sigma_2}{f_{cm}}} - 2 \frac{\sigma_c}{f_{cm}} - 1.254\right) \quad (9)$
	$\varepsilon_{c2,c} = 0.002 \left(1 + 5 \left(\frac{f_{cm,c}}{f_{cm}} - 1\right)\right) \quad (10)$
	$\varepsilon_{cu2,c} = 0.004 + 2.8 \frac{\sqrt{\rho_{wy} \cdot \rho_{wz}} f_{ym} \varepsilon_{su}}{f_{cm,c}} \quad (11)$
	$\sigma_2 = \alpha \cdot \sqrt{\rho_{wy} \cdot \rho_{wz}} \cdot f_{yw} \quad (12)$
prEC8/1	$f_{cm,c} = \begin{cases} f_{cm} + \alpha \cdot 4\sigma_2, & \text{if } \sigma_2 \leq 0.6 f_{cm} \\ f_{cm} + \alpha \cdot 3.5 \sigma_2^{\frac{3}{4}} f_{cm}^{\frac{1}{4}}, & \text{if } \sigma_2 > 0.6 f_{cm} \end{cases} \quad (13)$
	$\varepsilon_{c2,c} = 0.002 \left(1 + 5 \frac{f_{cm,c}}{f_{cm}}\right) \quad (14)$
	$\varepsilon_{cu2,c} = \begin{cases} \left(\frac{18.5}{h_0(mm)}\right)^2 + 0.04 \sqrt{\frac{\alpha \cdot (\rho_{wy} + \rho_{wz}) \cdot f_{yw}}{f_{cm}}}, & \text{if } M_{Rd,0} > 0.8 M_{Rd} \\ \min(0.01; \max(0.0035; \left(\frac{18.5}{h(mm)}\right)^2)), & \text{if } M_{Rd,0} \leq 0.8 M_{Rd} \end{cases} \quad (15)$
	$\sigma_2 = \min(\rho_{wy} \cdot f_{yw}; \rho_{wz} \cdot f_{yw}) \quad (16)$

$f_{cm}, f_{cm,c}$ – Compressive strength of unconfined and confined concrete

σ_2 – Confining stress

α – Confinement effectiveness factor

$\varepsilon_{c2}, \varepsilon_{c2,c}$ – Strain at maximum stress for unconfined and confined concrete

$\varepsilon_{cu2}, \varepsilon_{cu2,c}$ – Ultimate strain of unconfined and confined concrete

$\rho_{wz}, \rho_{wy}, \rho_{sx}$ – Ratio of lateral reinforcement in z- and y-directions and the direction of loading

f_{yw} – Transverse reinforcement strength

$M_{Rd}, M_{Rd,0}$ – Flexural resistance of the entire cross-section and flexural resistance of concrete core

Table 3. Eurocode limits of the ultimate strain in the longitudinal reinforcement

Procedure	Longitudinal reinforcement ultimate strain limitation
EC8/3a&EC2	$\varepsilon_{su} = \begin{cases} \min(\varepsilon_{su,exp}, 2.5\%), & \text{for ductility class A} \\ \min(\varepsilon_{su,exp}, 5.0\%), & \text{for ductility class B} \\ \min(\varepsilon_{su,exp}, 6.0\%), & \text{for ductility class C} \end{cases} \quad (17)$
EC8/3a	$\varepsilon_{su} = \begin{cases} \min(\varepsilon_{su,exp}, 2.5\%), & \text{for ductility class A} \\ \min(\varepsilon_{su,exp}, 5.0\%), & \text{for ductility class B} \\ \min(\varepsilon_{su,exp}, 6.0\%), & \text{for ductility class C} \end{cases} \quad (18)$
EC8/2	$\varepsilon_{su} = \begin{cases} \min(\varepsilon_{su,exp}, 2.5\%), & \text{for ductility class A} \\ \min(\varepsilon_{su,exp}, 5.0\%), & \text{for ductility class B} \\ \min(\varepsilon_{su,exp}, 7.5\%), & \text{for ductility class C} \end{cases} \quad (19)$
prEC8/1	$\varepsilon_{su} = \begin{cases} 0.4\varepsilon_{su,exp}, & \text{if } M_{Rd,0} > 0.8M_{Rd} \\ \frac{4}{15}\varepsilon_{su,exp} \left(1 + 3\frac{d_{bl}}{s}\right) (1 - 0.75e^{-0.4N_{b,compr}}), & \text{if } M_{Rd,0} \leq 0.8M_{Rd} \end{cases} \quad (20)$

$\varepsilon_{su,exp}, \varepsilon_{su}$ – Experimentally obtained and prescribed ultimate strain of longitudinal reinforcement
 d_{bl} – Diameter of longitudinal reinforcement bars
 s – Distance between stirrups
 $N_{b,compr}$ – Number of longitudinal reinforcement bars in compression
 $M_{Rd}, M_{Rd,0}$ – Flexural resistance of entire cross-section and flexural resistance of concrete core

2.3 Plastic hinge length

Damage to structural elements is typically limited to the end regions of elements subjected to the largest moments. This region is denoted as the plastic hinge.

The length of the plastic hinge, required in the analytical procedures for estimating the NC rotation, is assessed with the equations given in Table 4. They differ mainly regarding the assumed distribution of plastic deformations along the column.

The selection of a procedure for calculating the plastic hinge length should be consistent with the procedure used for section analysis. Different approaches cannot be combined because they have been calibrated to generate the appropriate ultimate chord rotations.

The equation from prEC8/1 is presented only for comparison and does not apply to columns with rectangular cross-sections, such as those considered in this study.

Table 4. Plastic hinge length estimation

Procedure	Plastic hinge length
EC8/3a&EC2	$L_{pl} = 0,1L_V + 0,17h + 0,24 d_{bl}f_{yl}/\sqrt{f_c} \quad (21)$
EC8/3a	$L_{pl} = L_V/30 + 0,2h + 0,11 d_{bl}f_{yl}/\sqrt{f_c} \quad (22)$
EC8/2	$L_{pl} = 0,1L_V + 0,015d_{bl}f_{yl} \quad (23)$
prEC8/1	$L_{pl} = (1 - 0.45\min(0,7; \nu)) \left(1 + 0,4\min\left(9; \frac{L_V}{h}\right)\right) \cdot \left(1 - \frac{1}{3}\sqrt{\min\left(2,5; \max\left(0,05; \frac{b}{h}\right)\right)}\right) 0,3h \quad (24)$

L_{pl} – Plastic hinge length

L_V – Shear span

h, b – Cross-section height and width of the compression zone, respectively

d_{bl} – Diameter of the longitudinal reinforcement bars

f_{yl}, f_c – Longitudinal reinforcement and concrete strength, respectively

ν – Axial load level

* not applicable to rectangular cross-sections

2.4 Near collapse rotation

The Eurocode 8 procedures considered in this study use different equations to calculate the NC rotation based on the parameters assessed in previous steps (Table 5). The analytical approaches (EC8/3a & EC2, EC8/3a & EC8/2) estimate the NC chord rotation, θ_{um} , summing the yield rotation, θ_y , and the post-yielding part of the chord rotation corresponding to the yield and ultimate curvatures (see Section 2.2).

The post-yielding part of the NC chord rotation is calculated by assuming a constant post-yield curvature distribution along the entire length of the plastic hinge.

The calculation of the NC chord rotation according to the empirical approach (EC8/3b) is conceptually different. The chord rotation is estimated based on the material, geometrical properties, and axial load ratio of the column.

Last, prEC8/1 combines the analytical and empirical approaches to estimate the yield chord rotation and the post-yielding part of the NC chord rotation, respectively.

Table 5. Summarised Eurocode procedures for calculating the ultimate (NC) rotation

Procedure	Equations
EC8/3a&EC2	$\theta_y = \varphi_y (L_V + \alpha_V z) / 3 + 0,0014 \left(1 + 1,5 \frac{h}{L_V} \right) + \frac{\varepsilon_y}{d - d'} \frac{d_{bl} f_{yl}}{6 \sqrt{f_c}} \quad (25)$
	$\theta_{um} = \theta_y + (\varphi_u - \varphi_y) L_{pl} \left(1 - \frac{0,5 L_{pl}}{L_V} \right) \quad (26)$
EC8/3a	$\theta_y = \varphi_y (L_V + \alpha_V z) / 3 + 0,0014 \left(1 + 1,5 \frac{h}{L_V} \right) + \frac{\varepsilon_y}{d - d'} \frac{d_{bl} f_{yl}}{6 \sqrt{f_c}} \quad (27)$
	$\theta_{um} = \theta_y + (\varphi_u - \varphi_y) L_{pl} \left(1 - \frac{0,5 L_{pl}}{L_V} \right) \quad (28)$
EC8/3b	$\theta_{um} = 0,016(0,3^v) \left[\frac{\max(0,01; \omega')}{\max(0,01; \omega)} f_c \right]^{0,225} \left(\min \left(9; \frac{L_V}{h} \right) \right)^{0,35} 25^{(\alpha_{\rho_{sx}} \frac{f_{yw}}{f_c})} 1,25^{100 \rho_d} \quad (29)$
EC8/2	$\theta_y = \varphi_y L_V / 3 \quad (30)$
	$\theta_{um} = \theta_y + (\varphi_u - \varphi_y) L_{pl} \left(1 - \frac{0,5 L_{pl}}{L_V} \right) \quad (31)$
prEC8/1	$\theta_y = \varphi_y (L_V + (d - d')) / 3 + \varphi_y \frac{f_{yl} d_{bl}}{8 \sqrt{f_c}} + 0,0019 \left(1 + \frac{h}{1,6 L_V} \right) \quad (32)$
	$\theta_{um} = \theta_y + K \cdot 0,016(0,2^v) \left[\frac{\max(0,01; \omega')}{\max(0,01; \omega)} \right]^{0,25} \left(\min \left(2; \frac{f_c}{25} \right) \right)^{0,1} \quad (33)$ $\left(\frac{1}{25} \min \left(9; \frac{L_V}{h} \right) \right)^{0,35} 24^{(\alpha_{\rho_{sx}} \frac{f_{yw}}{f_c})} 0,039$

θ_y, θ_{um} – Yield and ultimate (NC) rotations

L_{pl} – Plastic hinge length

φ_y, φ_u – Yield and ultimate curvatures

L_V – Shear span

$\alpha_V z = d - d'$ – Tension shift in moment diagram, if the shear cracking happens before the flexural yielding

h – cross-section height

ε_y – Longitudinal reinforcement yield strain

f_{yl}, f_{yw}, f_c – Flexural and transverse reinforcement steel and concrete strength

v – Axial load level

ω, ω' – Mechanical reinforcement ratio of the tension and compression flexural reinforcements

α – Confinement effectiveness factor

$\rho_{sw}, \rho_{sx}, \rho_d$ – Ratio of lateral reinforcement in the direction of loading, mean in both directions, and diagonal reinforcement

K – Correction factor considering the ductility class (1.0 for DC3, 0.9 for DC2, 0.8 for DC1)

3 Evaluation of Eurocode procedures against experiments

The Eurocode 8 procedures were used to calculate the NC rotations of two experimentally studied cantilever-reinforced concrete columns. The experiments were conducted at the Slovenian National Building and Civil Engineering Institute in cooperation with the University of Ljubljana [23]. By comparing the analysis and experimental data, the best way to estimate how they will respond was found.

The columns considered in this study are described in Subsection 3.1. Analysis and comparison with the experiments are presented in Subsections 3.2, 3.3, and 3.4.

3.1 Description of the columns

Anžlin [23] conducted a series of 1:2 scale cyclic tests on rectangular reinforced concrete columns with varying lateral reinforcement amounts and detailing. The shear span of the columns was 1.8 m, and the axial load level was about 10 % of the designed strength of the concrete section (common for bridge columns). The cross-section height and width were 30 and 40 cm, respectively, while the longitudinal reinforcement ratio was 1%. The concrete grade was C30/37, while the grade of the longitudinal reinforcement steel was S500, and the ductility class was C.

The cyclic horizontal displacement was imposed at the top of the columns in the weaker direction with gradually increasing cycle amplitudes. At each level of amplitude, two cycles were applied in a row while the axial load stayed the same.

One column had standard reinforcement (labeled STD/135) and the other had substandard reinforcement (labeled SUB/90). These two columns were chosen to test the methods described in Section 2. (Fig. 1). Column SUB/90 and STD/135 had a lateral reinforcement ratio of 0.25 % and 0.55 % and stirrups' hook angle of 90° and 135°, respectively.

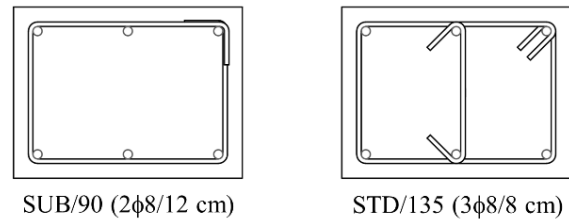


Figure 1. The cross-sections of columns

3.2 Material parameters and section analysis

The section analysis was performed in all cases using OpenSees [29] with a *ZeroLength* fibre section. The section was divided into concrete and steel fibres. Unconfined cover and confined core concrete were considered. They were created with the Concrete04 material. Confined concrete properties were defined according to the procedures presented in Table 2.

The stress–strain relationships for concrete defined according to different procedures are presented in Fig. 2 for columns SUB/90 and SUB/135. All of the procedures result in a similar strength for the confined concrete. However, the ultimate deformations of the confined concrete differ significantly. For both columns, the highest ultimate deformations were obtained using the EC8/2 procedure, while the lowest ultimate deformations resulted from the EC8/3a&EC2 procedure. The ratio between the highest and lowest ultimate deformations is more than 2.

Steel02 was used to model the longitudinal reinforcement. This material does not limit the maximum strain (Table 3). Therefore, it was considered in the post processing stage. Fig 3. shows the longitudinal reinforcement stress–strain relationships for the two columns, together with the limitations of the ultimate strain obtained with different procedures (Table 3). The experimentally obtained ultimate strain is also presented; however, this was obtained under monotonic loading. Thus, it exceeded almost all analytical values.

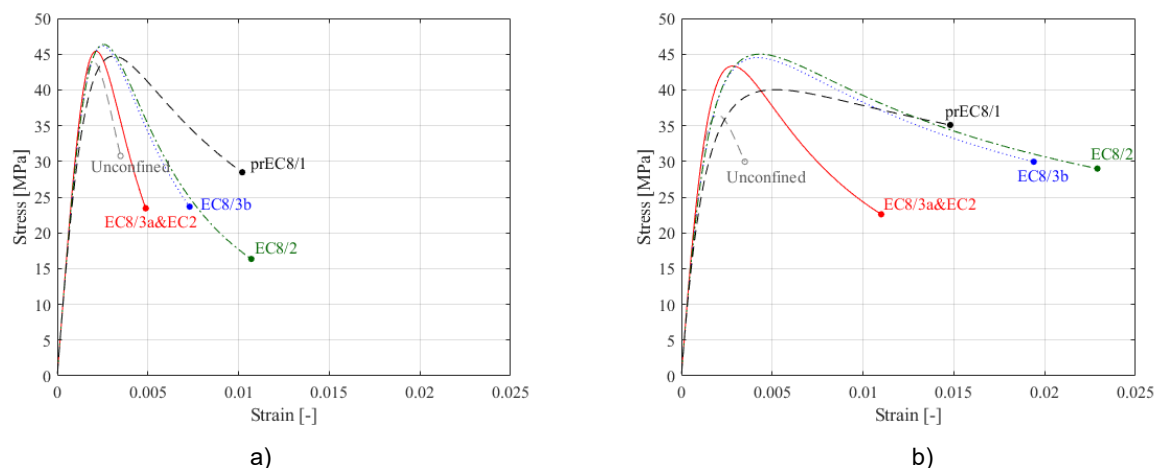


Figure 2. Concrete stress–strain relationships assigned in OpenSees for columns a) SUB/90 and b) STD/135 (compression is positive)

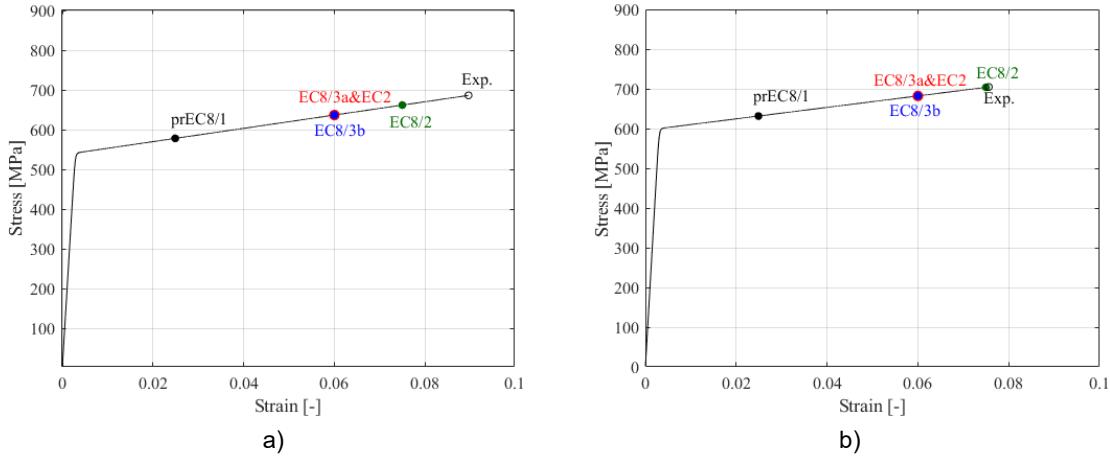


Figure 3. Longitudinal reinforcement stress–strain relationships assigned in OpenSees, Eurocode 8 limitations of the ultimate strain and the experimentally obtained ultimate strain for columns a) SUB/90 and b) STD/135

The moment–curvature relationships were idealised as elastoplastic. Idealisation was performed by assuming the pre-yield stiffness is the secant stiffness at the point where the first yielding of the longitudinal reinforcement occurs, considering the equal surface rule and equalising the areas under the actual and idealised curves.

It was assumed that the ultimate curvature was reached when the ultimate strain was attained either in the confined concrete or in the longitudinal reinforcement. The idealisation of the moment–curvature relationship is illustrated in Fig. 4 for the example of the prEC8/1 procedure for column SUB/90. In this case, the reinforcement failure was identified as critical.

The idealised moment–curvature relationships were determined for both columns and all procedures that use section analysis (Fig. 5). While the strengths were similar in all cases, the maximum curvatures obtained with the considered procedures differed significantly. According to all procedures except for prEC8/1, the ultimate curvature of column SUB/90 was governed by the ultimate strain of the confined concrete. In column STD/135, only the

EC8/3a&EC2 procedure predicted that the concrete failure was critical.

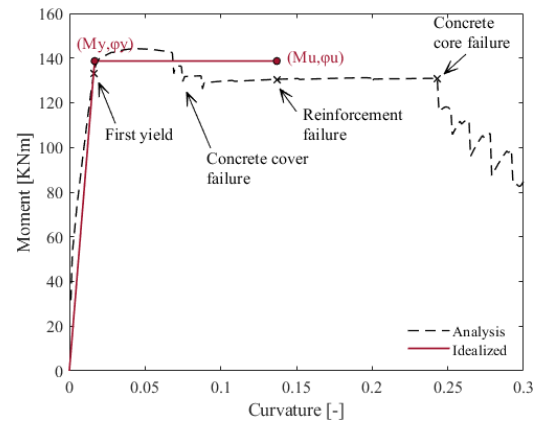


Figure 4: An example of the idealisation of the moment–curvature relationship

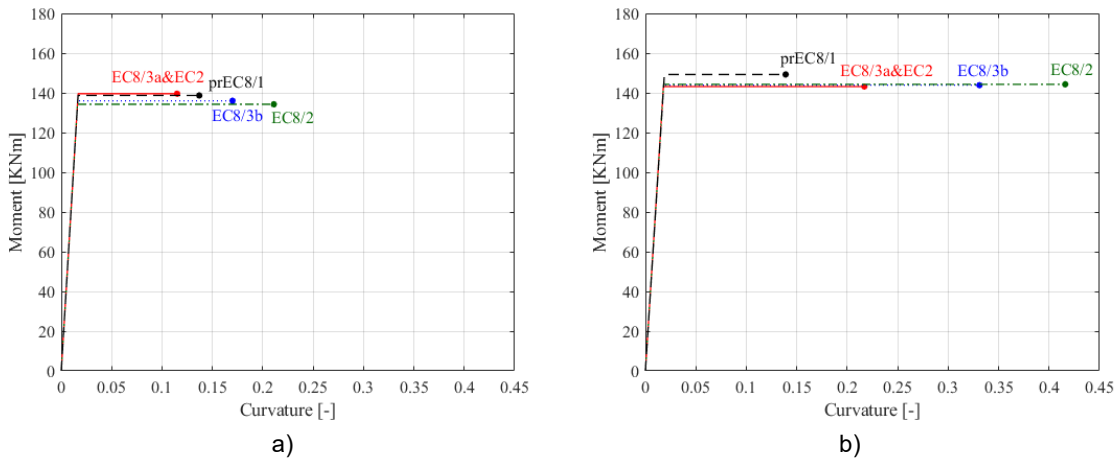


Figure 5. The idealised moment–curvature relationships for columns a) SUB/90 and b) STD/135

3.3 Plastic hinge length

Another parameter that influences the ultimate chord rotation is the plastic hinge length. Plastic hinge lengths of two considered columns obtained with different procedures (see Table 4) are summarised in Fig. 6. The results are presented only for the analytical approaches. The largest values were obtained with procedure EC8/3a&EC2, which amounted to about twice the height of the cross-section. According to the other two theoretical procedures, the plastic hinge length was about two times smaller.

3.4 Near collapse rotation – comparison with experiments

The NC rotations were calculated using the equations in Table 5 and compared to the experimental results. Figs. 7 and 8 compare columns SUB/90 and STD/135, respectively.

In SUB/90, the measured NC collapse rotation (corresponding to a 20 percent loss of flexural strength) was

5.5 percent. All the procedures, except EC8/3&EC2, matched the experimental data very well.

In column STD/135, the measured NC chord rotation was 7.5 %. The analytical procedures (EC8/3a and EC8/2) that predicted the NC rotation of the poorly confined column SUB/90 significantly overestimated the NC rotation. The NC rotation predicted by the empirical procedure EC8/3b was slightly lower than the measured one. The analytical procedure EC8/3a&EC2 and the combined procedure prEC8/1 were the most conservative.

The comparison of NC rotations obtained with Eurocode 8 procedures showed that the empirical procedure in the current version of Eurocode 8/3 could adequately estimate the NC rotation for both poorly and well-confined columns. Therefore, this procedure was considered in the second part of this study (Section 4), where different approaches for modelling the entire post-capping flexural response were analysed.

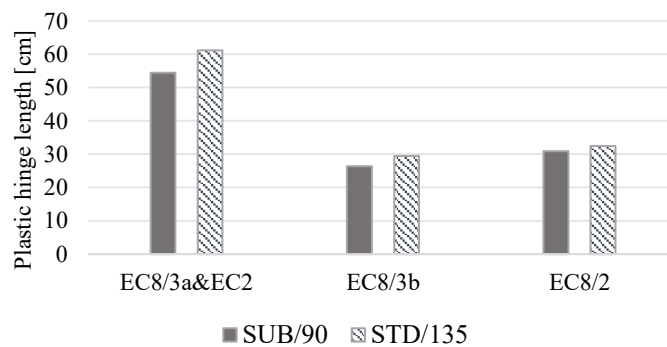


Figure 6. The estimated plastic hinge lengths for the analysed columns

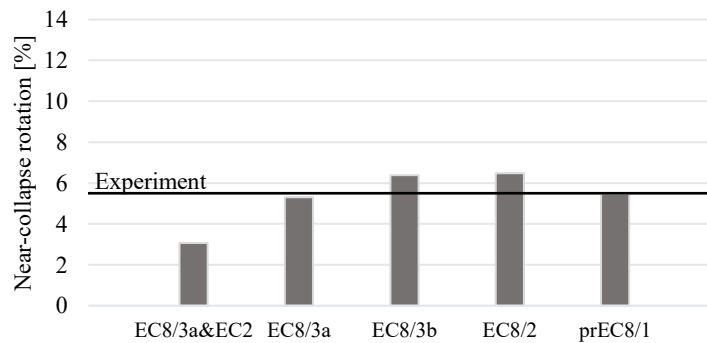


Figure 7. Comparison of predicted NC rotations with experimentally determined value for column SUB/90

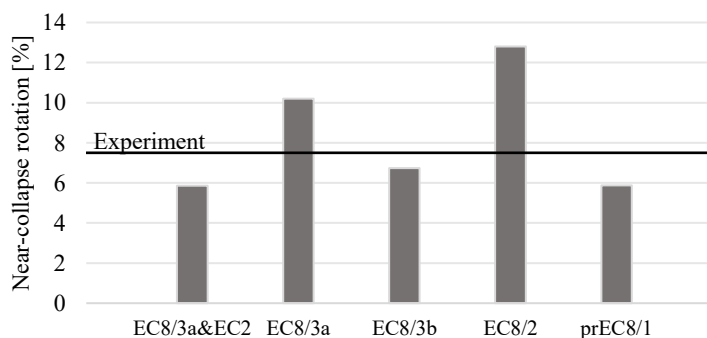


Figure 8. Comparison of the predicted NC rotations with experimentally determined value for column STD/135

4 Moment–rotation relationship for lumped plasticity models

The moment–rotation backbone of plastic hinges is one of the key features of lumped plasticity models. Different procedures to define the backbone are available. The backbone is typically considered trilinear (e.g. [17, 20, 22]), having an initial elastic branch, a plastic branch, and a post-capping branch (Fig. 9a).

The trilinear model can be refined by increasing the number of branches, which may increase the generality of the model but also make it more difficult to calibrate. As this study focused on the post-capping part of the backbone, the impact of increasing the number of branches in that region was explored. An example of such a backbone is the quadrilinear moment–rotation model with a bilinear post-capping response (Fig. 9b) proposed by Anžlin [23]. In the present study, both types of backbone models, trilinear and quadrilinear, were evaluated and compared to the results of the experiments presented in Section 3.1.

4.1 Trilinear moment–rotation backbone

The trilinear moment–rotation backbone (Fig. 9a) can be defined by three characteristic points. In this study, the first two characteristic points corresponded to the yield (Y) and NC limit states.

The rotations at these limit states were defined according to the empirical approach included in the current version of Eurocode 8/3 (see Subsection 2.4). Following the typical procedures reported in the literature, the capping (Cap) point and the total collapse (TC) point were obtained based on the slope of the post-capping branch of the backbone curve. In their evaluation of a code-compliant structure, Žižmond et al. [30] defined the post-capping slope as a ratio of 3.5 between the rotation at the TC point and the rotation at the Cap point (Model T1 in Table 6). This value is consistent with the

observations Dolšek [31], which showed that the ratio between the TC and Cap rotations in backbone models is usually between 3 and 4.

In another study, Kreslin and Fajfar [22] have analysed an older structure and defined the post-capping slope based on a ratio between the plastic parts of the TC and NC rotations ($k_{pl,TC/NC}$) equal to 2.0 (Model T2 in Table 6). Comparing these two studies suggests that the post-capping stiffness is affected by the level of design. Consistent with this observation, Anžlin [23] has proposed an equation for determining $k_{pl,TC/NC}$ based on the effective mechanical volumetric confinement ratio in the column, $\omega_\alpha = \alpha\rho_w f_{yw}/f_c$ (Model T3 in Table 6):

$$k_{pl,TC/NC} = \min(-0.02\omega_\alpha(\%) + 1.55 \geq 1; 1.34) \quad (34)$$

In Model T3, $k_{pl,TC/NC}$ was equal to the upper bound (1.34) for both columns.

Three different models of the trilinear moment–rotation backbone were defined by considering these three approaches. The corresponding moments were calculated using the section analysis described in Subsection 2.2 and the following assumptions: moments M_Y and M_{Cap} were assumed to be equal to the maximum moment from the section analysis, moment M_{NC} was assumed to be 80 % of M_{Cap} , and moment M_{TC} was assumed to be 0. Moreover, the rotations at points Y and NC (see Fig. 9) were considered equal to rotations θ_y and θ_{um} , respectively. They were defined according to the Eurocode 8/3 empirical procedure (see Subsection 2.4).

The moment–rotation backbones were calculated for the two tested columns (Subsection 3.1) and compared to the experimentally obtained cyclic responses (Fig. 10). All three backbone models intersect at the NC point, one of the modelling assumptions. At this point, the models matched well with the experimental results, which is a direct consequence of the capability of the Eurocode 8/3 empirical procedure to predict the NC rotation.

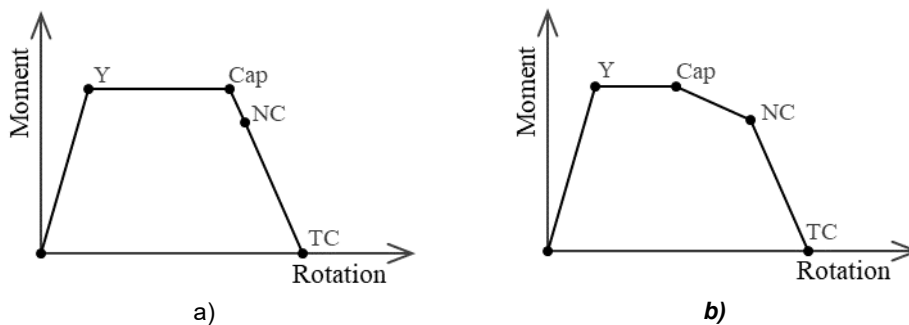


Figure 9. Moment–rotation backbone models: a) trilinear and b) quadrilinear

Table 6. Characteristic points of trilinear moment–rotation backbone models

Model	Characteristic point	Rotation
Model T1	Cap	$\theta_{Cap} = \theta_{NC}/1.5$
	TC	$\theta_{TC} = 3.5\theta_{Cap}$
Model T2	Cap	$\theta_{Cap} = 1.25\theta_{NC} - 0.25\theta_{TC}$
	TC	$\theta_{TC} = \theta_Y + 2.0(\theta_{NC} - \theta_Y)$
Model T3	Cap	$\theta_{Cap} = 1.25\theta_{NC} - 0.25\theta_{TC}$ $k_{pl,TC/NC} = 1.34$
	TC	$\theta_{TC} = \theta_Y + k_{pl,TC/NC}(\theta_{NC} - \theta_Y)$ (SUB/90 and STD/135)

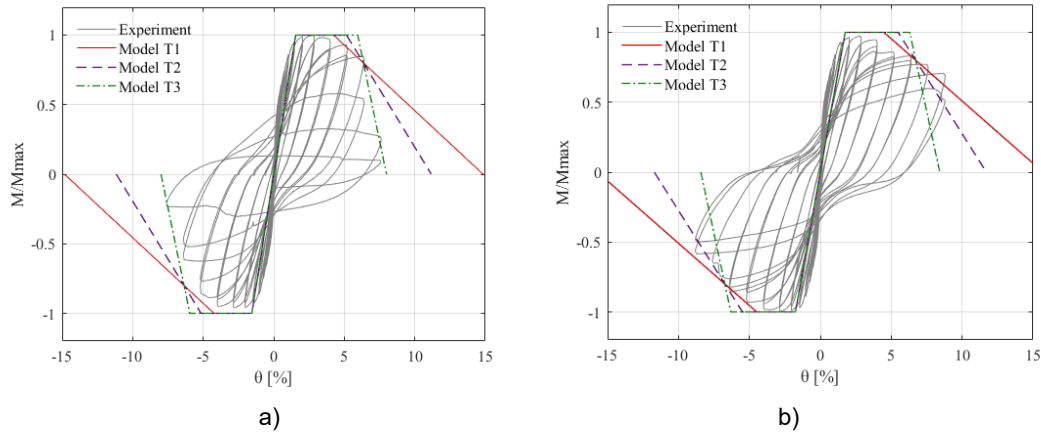


Figure 10. Comparison of trilinear moment–rotation backbones for columns a) SUB/90 and b) STD/135

Model T1 and Model T2 provided a fair prediction of the post-capping region up to the NC point for both columns. This result was expected because these models were originally proposed for such purposes. However, Model T3 gives the best prediction for the poorly confined column from the NC point on. However, none of the trilinear backbone models was suitable for modelling the entire post-capping region of both columns.

4.2 Quadrilinear moment–rotation backbone

In order to better match the post-capping response with the experimental results, four quadrilinear moment–rotation backbone models were also defined (Fig. 9b). The definition of quadrilinear backbone models includes an additional characteristic point as an independent parameter. The Cap point, which has already been addressed, was used as this additional fourth characteristic point. For all quadrilinear backbone models, the capping rotation was calculated according to the empirical procedure proposed by Haselton [10]:

$$\theta_{cap} = 0.12(1 + 0.4\alpha_{sl})(0.2)^v(0.02 + 40\rho_{sx})^{0.52}(0.56)^{0.01f_c}(2.37)^{10\rho_l} \quad (35)$$

$$k_{TC/cap} = \min(0.19\omega_\alpha(\%); -0.02\omega_\alpha(\%) + 6.86; 4) \quad (36)$$

where v is the level of axial load, f_c is the concrete compressive strength, ρ_l is the longitudinal reinforcement ratio, ρ_{sx} is the ratio of lateral reinforcement in the direction of loading, and α_{sl} is an indicator of the possibility of bond–slip. The moment corresponding to the Cap point was considered equal to the maximum moment from the section analysis in the same manner as for the trilinear backbone (Subsection 4.1). Moreover, the same moments and rotations corresponding to the Y and NC points were used as for the trilinear backbone.

Four quadrilateral models with different post-NC branches were considered (see Table 7 and Fig. 11). Models Q1 and Q2 were defined based on the same assumptions as the trilinear backbone models (Subsection 3.1). In Model Q3, the rotation at the TC point was obtained using the ratio between the rotation at the TC point and the Cap point ($k_{TC/cap}$) proposed by Anžlin [23], specifically for application to quadrilinear backbones:

Table 7. Characteristic points of quadrilinear moment–rotation backbone models

Model	Characteristic point	Rotation	
Model Q1	Cap	θ_{cap} – from Eq. 14	
	TC	$\theta_{TC} = 3.5\theta_{cap}$	
Model Q2	Cap	θ_{cap} – from Eq. 14	
	TC	$\theta_{TC} = \theta_Y + 2.0(\theta_{NC} - \theta_Y)$	
Model Q3	Cap	θ_{cap} – from Eq. 14	$k_{TC/cap} = 2.1$ (SUB/90)
	TC	$\theta_{TC} = k_{TC/cap}\theta_{cap}$	$k_{TC/cap} = 3.2$ (STD/135)
Model Q4	Cap	θ_{cap} – from Eq. 14	
	TC	θ_{TC} – from Eq. 16	

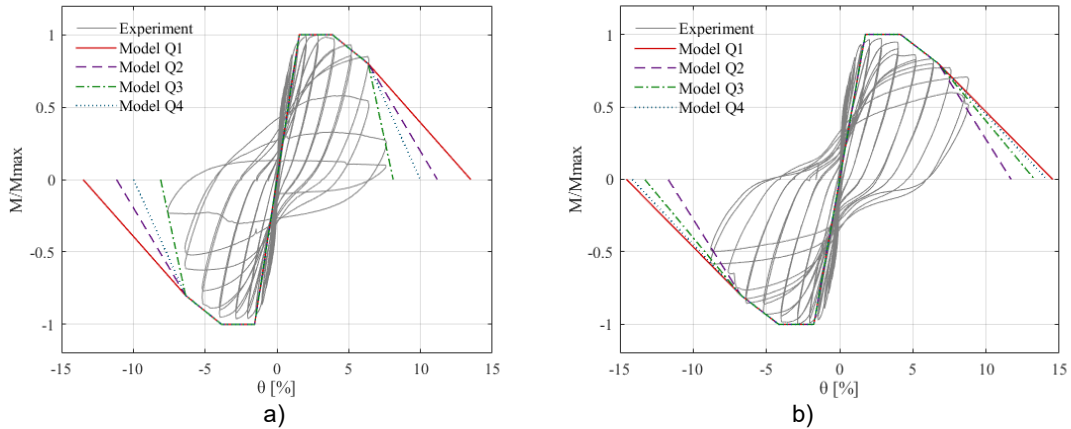


Figure 11. Comparison of quadrilinear moment–rotation backbones for columns a) SUB/90 and b) STD/135

In Model Q4, the rotation at the TC point was obtained using an empirical expression for post-capping rotation capacity developed by Haselton [10]:

$$\theta_{TC} = \theta_{Cap} + 0.76(0.031)^{\nu}(0.02 + 40\rho_{sx})^{1.02} \leq \theta_{Cap} + 0.1 \quad (37)$$

This model was selected by considering the capping rotation model (Eq. (35)) proposed by the same author. Eqs. (35) and (37) were originally proposed for use in combination with the Ibarra hysteresis model [20]. This model accounts for history-dependent strength and stiffness deterioration, which is not the case in the present study.

The quadrilinear moment–rotation backbones are compared with the experimental data in Fig. 11. In the poorly confined column, the post-capping response was very accurately predicted by Model Q3, while the other three models overestimated the TC rotation. The experimental response of the well-confined column was simulated very well by Models Q1, Q3 and Q4. The model Q2 slightly underestimated the moments after the NC point. This outcome was expected because Model Q2 was originally used to predict the post-capping response of columns that did not meet the requirements of Eurocode. Model Q3 was found to be the most general and suitable for predicting the post-capping response of both poorly and well confined columns based on these findings.

4.3 Application of the quadrilinear moment–rotation backbone model

The best match with the experimental results was obtained with the quadrilinear backbone model (see Fig. 11b) defined by: (i) the Cap rotation calculated according to Haselton [10], (ii) the NC rotation determined according to the empirical Eurocode 8/3 procedure [25], and (iii) the TC rotation as proposed by Anžlin [23]. Therefore, this model was chosen for the simulation of the cyclic experiments. The experiments were numerically simulated in the *OpenSees* software [29]. The columns were modelled with the Giberson lumped plasticity model. A nonlinear ZeroLength element was used at the base to model the nonlinear response. The rest of the column was represented by an infinitely stiff and elastic element.

The cyclic behaviour of the nonlinear element was modelled using the *TakedaDAsym* material [32] which follows the Takeda hysteresis rules [1] and considers a quadrilinear moment–rotation backbone. The analytical and experimental cyclic responses are compared in Fig. 12. They had a good match for both the poorly and well confined columns.

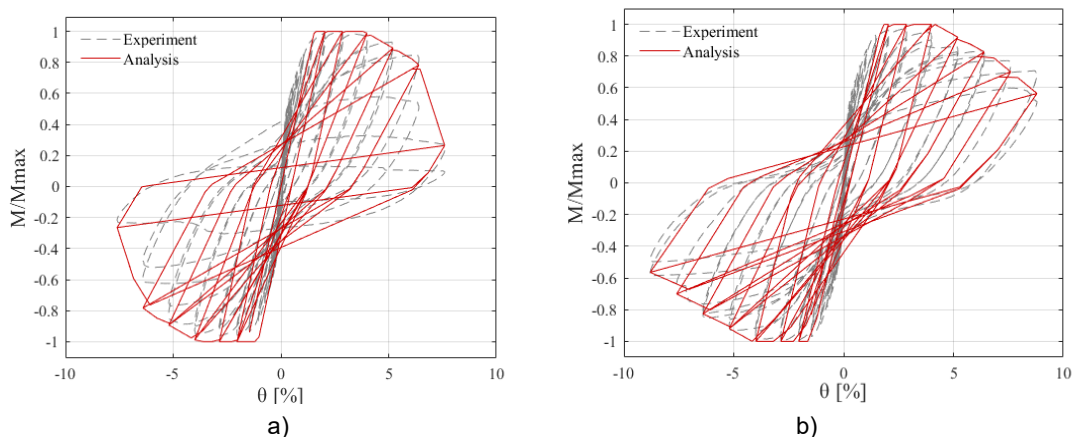


Figure 12. Results of numerical analysis for columns a) SUB/90 and b) STD/135

5 Conclusions

Different procedures for estimating the NC rotation included in Eurocode 8 (current versions of Eurocode 8/3 [25], Eurocode 8/2 [26], and the draft of the new version of Eurocode 8/1 [27]) were compared and evaluated by cyclic experiments of well- and poorly-confined RC columns with rectangular cross-sections.

Some procedures predicted the response of substandard columns well but were less effective for standard columns, while others had the opposite results. The only effective procedure in both cases was the empirical procedure included in Eurocode 8/3.

The NC rotation estimated according to the Eurocode 8/3 empirical procedure was used as a basis to define several trilinear and quadrilinear moment–rotation backbone models. These were verified against the experiments, and the most suitable model was identified.

The models proposed in the literature for columns with a certain level of confinement may not be generally suitable. The generality of a model can be improved by increasing the number of branches in the post-capping part of the backbone. The best match for both types of columns was obtained using the quadrilinear backbone model defined by: (i) the Haselton capping rotation [10], (ii) the Eurocode 8/3 NC rotation, and (iii) the TC rotation proposed by Anžlin for quadrilinear backbones [23].

This quadrilinear backbone model is proposed for simulating the seismic response of reinforced concrete elements with predominantly flexural behaviour. The results suggest that the model can be applied generally regardless of the seismic design level of the structure, which is a useful feature when analysing a portfolio of structures constructed in different periods. Moreover, the proposed model simulates the seismic response at various intensity levels up to the point of TC, making it suitable for studies to estimate the risk of casualties.

However, only a limited number of columns were considered in this study. Extension of the presented study is needed, and it is planned to be performed soon. Moreover, further research is needed to evaluate the impact of the modelling uncertainty associated with the simulation of the post-capping response on the risk of casualties, as this would help to better understand the significance of appropriate modelling of the post-capping region.

Acknowledgements

The research presented in this paper is based on work sponsored by the Slovenian Research Agency, which is gratefully acknowledged. The authors would also like to thank Andrej Anžlin from the Slovenian National Building and Civil Engineering Institute for his help.

References

- [1] Takeda T, Sozen M. A, Nielsen N. N. Reinforced concrete response to simulated earthquakes. *Journal of Structural Division* 96, 1970, 12: 2557–2573, <https://doi.org/10.1061/JSDEAG.0002765>.
- [2] Allahabadi R, Powell G. H. DRAIN-2DX: user guide. Berkeley, the United States: Earthquake Engineering Research Center, University of California, 1988.
- [3] Kunnath S. K, Reinhorn A. M, Park Y. J. Analytical modeling of inelastic seismic response of R/C structures. *Journal of Structural Engineering* 116, 1990, 4: 996-1017, [https://doi.org/10.1061/\(ASCE\)0733-9445\(1990\)116:4\(996\)](https://doi.org/10.1061/(ASCE)0733-9445(1990)116:4(996)).
- [4] Dymiotis C, Kappos A. J, Chryssanthopoulos M. K. Seismic reliability of RC frames with uncertain drift and member capacity. *Journal of Structural Engineering* 125, 1999, 9: 1038-1047, [https://doi.org/10.1061/\(ASCE\)0733-9445\(1999\)125:9\(1038\)](https://doi.org/10.1061/(ASCE)0733-9445(1999)125:9(1038)).
- [5] Pincheira J, Dotiwala F. S, D'Souza J. T. Seismic analysis of older reinforced concrete columns. *Earthquake Spectra* 15, 1999, 2: 245-272, <https://doi.org/10.1193/1.1586040>.
- [6] Blasone V, Basaglia A, De Risi R, De Luca F, & Spacone E. A simplified model for seismic safety assessment of reinforced concrete buildings: framework and application to a 3-storey plan-irregular moment resisting frame. *Engineering Structures*, 250, 2022, 113348, <https://doi.org/10.1016/j.engstruct.2021.113348>
- [7] D'Angela D, Magliulo G, Celano F, & Cosenza E. Characterization of local and global capacity criteria for collapse assessment of code-conforming RC buildings. *Bulletin of Earthquake Engineering* 19, 2021, 9: 3701-3743, <https://doi.org/10.1007/s10518-021-01115-y>
- [8] Bayari M A, Shabakhty N, & Abadi E I Z. Analyzing uncertainties involved in estimating collapse risk with and without considering uncertainty probability distribution parameters. *Earthquake engineering and engineering vibration*, 2022, 1-16. <https://doi.org/10.1007/s11803-021-2068-x>
- [9] Panagiotakos T. B, Fardis M. N. Deformations of reinforced concrete members at yielding and ultimate. *Structural Journal*, 98, 2001, 2: 135-148. <https://doi.org/10.14359/10181>.
- [10] Haselton C. B. Assessing Seismic collapse safety of modern reinforced concrete modern frame buildings. PhD Thesis. Stanford, CA, USA: Stanford University, 2006.
- [11] Singhal A, Kiremidjian A. S. Method for probabilistic evaluation of seismic structural damage. *Journal of structural Engineering* 122, 1996, 12: 1459-1467, [https://doi.org/10.1061/\(ASCE\)0733-9445\(1996\)122:12\(1459\)](https://doi.org/10.1061/(ASCE)0733-9445(1996)122:12(1459)).
- [12] Melani A, Khare R. K, Dhakal R. P, Mander J. B. Seismic risk assessment of low rise RC frame structure. *Structures* 5, 2016, 13-22, <https://doi.org/10.1016/j.istruc.2015.07.003>.
- [13] Babič A, Dolšek M. Seismic fragility functions of industrial precast building classes. *Engineering structures* 118, 2016, 357-370, <https://doi.org/10.1016/j.engstruct.2016.03.069>.
- [14] Suselo A. A. Simulated Behavior of Rectangular Reinforced Concrete Columns under Seismic Loading. Doctoral dissertation, The University of Texas at San Antonio, 2021.
- [15] Eldawie A. Collapse Modeling of Reinforced Concrete Frames Under Seismic Loading. Doctoral dissertation, Ohio State University, 2020.
- [16] ASCE/SEI. Seismic rehabilitation of existing buildings (ASCE/SEI 41-17). Reston, VA, 2017, 623pp

- [17] Fischinger M, Kramar M, Isaković T. Cyclic response of slender RC columns typical of precast industrial buildings. *Bulletin of earthquake engineering*6, 2008, 3: 519-534, <https://doi.org/10.1007/s10518-008-9064-7>.
- [18] Jalayer F, Ebrahimi H. Seismic risk assessment considering cumulative damage due to aftershocks. *Earthquake Engineering & Structural Dynamics*46, 2017, 3: 369-389, <https://doi.org/10.1002/eqe.2792>.
- [19] Dolšek M, Fajfar P. Mathematical modelling of an infilled RC frame structure based on the results of pseudo-dynamic tests. *Earthquake engineering & structural dynamics*31, 2002, 6: 1215-1230, <https://doi.org/10.1002/eqe.154>.
- [20] Ibarra L. F, Medina R. A, Krawinkler H. Hysteretic models that incorporate strength and stiffness deterioration. *Earthquake Engineering & Structural Dynamics* 34, 2005, 12:1489–1511, <https://doi.org/10.1002/eqe.495>.
- [21] Verderame G. M, Polese M, Mariniello C, Manfredi G. A simulated design procedure for the assessment of seismic capacity of existing reinforced concrete buildings. *Advances in Engineering Software*41, 2010, 2: 323-335, <https://doi.org/10.1016/j.advengsoft.2009.06.011>.
- [22] Kreslin M, Fajfar P. Seismic evaluation of existing complex RC building. *Bulletin of Earthquake Engineering* 8, 2010, 2: 363–385, <https://doi.org/10.1007/s10518-009-9155-0>.
- [23] Anžlin A. Influence of buckling of longitudinal reinforcement in columns on seismic response of existing reinforced concrete bridges. PhD Thesis. Ljubljana, Slovenia: University of Ljubljana, 2017.
- [24] Di Domenico M, Ricci P, Verderame GM. Empirical calibration of hysteretic parameters for modeling the seismic response of reinforced concrete columns with plain bars. *Eng Struct*, 2021, 237:112120, <https://doi.org/10.1016/j.engstruct.2021.112120>
- [25] CEN. Eurocode 8: Design of structures for earthquake resistance – Part 3: Assessment and retrofit of buildings. Comité Européen de Normalisation (EN 1998-3:2005). Brussels, Belgium, 2005.
- [26] CEN. Eurocode 8: Design of structures for earthquake resistance – Part 2: Bridges. Comité Européen de Normalisation (EN 1998-2:2005). Brussels, Belgium, 2005.
- [27] CEN. Eurocode 8: Design of structures for earthquake resistance – Part 1-1: General rules and seismic actions. Working draft by project team SC8 2021-02-17, CEN TC 250 work programme. Comité Européen de Normalisation (prEN 1998-1:2020). Brussels, Belgium, 2020.
- [28] CEN. Eurocode 2: Design of concrete structures – Part 1-1: General rules and rules for buildings. Comité Européen de Normalisation (EN 1991-1:2005). Brussels, Belgium, 2005.
- [29] McKenna F, Fenves G. L, Scott M. H. Open system for earthquake engineering simulation. University of California, Berkeley, 2000. <http://opensees.berkeley.edu>.
- [30] Žižmond J, Podgorelec D, Dolšek M. Relationship between the collapse risk and the reinforced concrete frame structure. In *Second European conference on earthquake engineering and seismology*. Istanbul, Turkey, 2014.
- [31] Dolšek M. Development of computing environment for the seismic performance assessment of reinforced concrete frames by using simplified nonlinear models. *Bulletin of Earthquake Engineering* 8, 2010, 6: 1309–1329, <https://doi.org/10.1007/s10518-010-9184-8>.
- [32] Zevnik J. Potresna ranljivost armiranobetonskih viaduktov s škatčastimistebri. PhD Thesis. Ljubljana, Slovenia: University of Ljubljana, 2007.



Design of cross-laminated timber (CLT) floors for human-induced vibrations

Nađa Simović^{*1)}, Ivan Glišović¹⁾, Marija Todorović¹⁾

¹⁾ University of Belgrade, Faculty of Civil Engineering, Bulevar kralja Aleksandra 73, 11000 Belgrade, Serbia

Article history

Received: 06 December 2022

Received in revised form:

20 February 2023

Accepted: 23 February 2023

Available online: 30 March 2023

Keywords

CLT floor,
vibrations,
walking excitation,
design method,
serviceability

ABSTRACT

Cross-laminated timber (CLT) is an innovative engineering wood product made by gluing layers of solid timber boards placed in an orthogonally alternating orientation to the neighbouring layers. CLT panels provide an efficient solution for floors in single- and multi-storey buildings. Due to their light weight and often long-span, the design of these floors is generally governed by serviceability limit state criteria, that is, deflection or vibration limits. Vibrations induced by dynamic actions, such as people walking and their everyday activities, cannot result in structural failure but may cause discomfort to occupants if vibrations are not properly controlled. This paper gives an overview of some available methods for the vibration serviceability design of residential CLT floors. Differences between these methods are discussed through the consideration of criteria and their limit values. Although some criteria are common to certain methods, it may happen that the same criteria take into account different factors. In order to get a better description of the actual behaviour of floor structure, certain classifications of floors based on vibration serviceability performance were introduced in design methods.

1 Introduction

Cross-laminated timber (CLT) is a massive engineering wood product made by gluing cross-wise layers of solid timber boards together to form large-scale panels. CLT products are usually fabricated with an odd number of layers (in general, three to seven layers). Due to their excellent in-plane and out-of-plane resistance, CLT panels have become very common for walls and floors. Advantages such as dimensional stability, good acoustic and thermal properties, and a high level of prefabrication make CLT a competitive structural material for many building types.

For CLT panels used as floor elements, serviceability limit states (deformations, vibrations) generally control the design. Although floor vibrations may result from many sources (e.g. use of machinery, external traffic, explosions), the most common and problematic ones are caused by the occupants themselves from their everyday activities. Such vibrations are particularly problematic because they cannot be easily isolated from the structure and they occur frequently [1]. Human-induced vibrations do not collapse floors, but they can annoy occupants or cause malfunctions of vibration-sensitive equipment.

When compared to heavy floors such as those made of concrete, the amplitudes of vibration responses found in timber floors are relatively high. This is because amplitudes of response are inversely proportional to the self-weight of the structure being vibrated. As human bodies are generally sensitive to vibrations, this high-level response can cause discomfort and disturbance to building occupants. As a

result, design requirements for disturbing vibration performance are especially important for light-weight floors made of materials such as timber. New floor systems, such as CLT floors, differ in mechanical characteristics compared to traditional joist floors, as strength and stiffness are higher both in the load-bearing (longitudinal) and transverse directions. This also improves vibration performance, but the issue of floor vibrations induced by human activities is still very significant since new building designs allow buildings with larger spans.

Vibrational performance of wood floor systems has received a lot of attention in the last few decades, and different design rules have been suggested. Proposed design methods range from simple limitations of static deflection to those intended to limit fundamental frequency and vibration velocity or acceleration levels at floor surfaces caused by defined excitations [2]. However, the vibration serviceability design criteria applied to traditional timber floors are probably not appropriate for CLT floor design.

This paper focuses on the basic principles for the vibration design of residential floors made of cross-laminated timber. Some available design methods are presented and compared. Due to differences in considered parameters and limit values, application of these methods may lead to significantly different results.

* Corresponding author:

E-mail address: nsimovic@grf.bg.ac.rs

2 Floor dynamics

Acceleration and deceleration of the human body during various human activities cause dynamic forces. Forces depend upon many factors, including characteristics of the person(s) involved, activity being undertaken (e.g., walking, running, jumping), number of people, whether activities of different people are coordinated, and characteristics of the floor surface [3]. Walking excitation is commonly associated with the annoying vibration of timber floors. Walking frequency (common range 1.5-2.5 Hz) has a direct impact on the dynamic load applied. The dynamic force of walking has been found to excite frequencies up to the third or fourth harmonic of walking frequency [4].

The vibration response of a floor when subjected to dynamic loading depends on its stiffness, mass, and damping. For each floor mode of vibration, stiffness and mass determine the floor's natural frequencies, while damping affects the time it takes for an induced vibration to decay. Depending on the value of the fundamental frequency, the vibration response of the floor due to people walking may differ [5]. So-called low-frequency floors have a fundamental frequency below 8-10 Hz and can respond to walking excitation with resonant vibrations. The resonance is constantly maintained by continuous walking. On the other hand, high-frequency floors with a fundamental frequency above 8-10 Hz show a transient vibration response to each individual heel strike from each footstep. Depending on the intervals between successive impacts and the damping of vibration, adjacent transient vibration responses may interact with each other.

The response of floors to an impact can be represented by the time history of displacement, velocity, or acceleration [6]. Quantities such as peak value or root-mean-square (r.m.s.) value have been used as a measure of human sensitivity to vibration. The peak value is extracted from the initial part of the response (forced vibration) due to an impact. The r.m.s. value is determined from the entire response, including the initial forced and free vibration parts of the response.

The use of CLT elements has altered the characteristics of the dynamic response of floors and complete buildings, resulting in more vibration serviceability problems. At least in part, this is because engineered wood products, such as

CLT, increase the modal stiffness-to-mass ratio and the design live load-to-dead load ratio, both of which tend to result in increased vibration acceleration levels [2].

3 Human perception of floor vibrations

The human body is an incredibly complex and sensitive receiver that is self-adapting and more or less susceptible to almost any type and level of motion, such as periodic, random, or transient vibrations, which normally occur in nature [7]. Acceptable vibration levels for human occupancy vary with the individual's activity, body posture, life environment, and expectation of felt vibrations. The presence of visual or audio effects may significantly reduce the acceptable vibration magnitude. Therefore, it is difficult to set the threshold for human perception of vibrations.

The characterization of building vibration with respect to human response is given in ISO 10137 Annex C [8], which includes "base curves" expressed as a function of r.m.s. acceleration and frequency. At vibration acceleration magnitudes below the values corresponding to the base curves, in general, adverse comments, sensations, or complaints are very rare. Since the magnitude that is considered satisfactory, depends on the circumstances, multiplying factors are used to increase the acceleration level of these base curves according to the intended use of the building. These multiplying factors are referred to as "response factors."

The base curve for vertical vibration is presented in Figure 1. The graph shows that the perception threshold for vibrations is lowest for the frequency range between 4 and 8 Hz, with a constant value of $a_{\text{rms,base}} = 0.005 \text{ m/s}^2$. Vibrations having a frequency between 4 and 8 Hz are particularly critical because large body organs within the rib cage and abdomen resonate within this frequency range. Above 8 Hz, the minimum perception level is not constant in terms of acceleration, but it increases as the frequency increases. However, when this part of the curve is integrated, it can be shown that it is constant in terms of velocity with a value of $v_{\text{rms,base}} = 0.0001 \text{ m/s}$. Therefore, below the floor frequency of 8 Hz, the acceleration criterion for vibration perception threshold can be applied, and above the 8 Hz, velocity criterion can be applied.

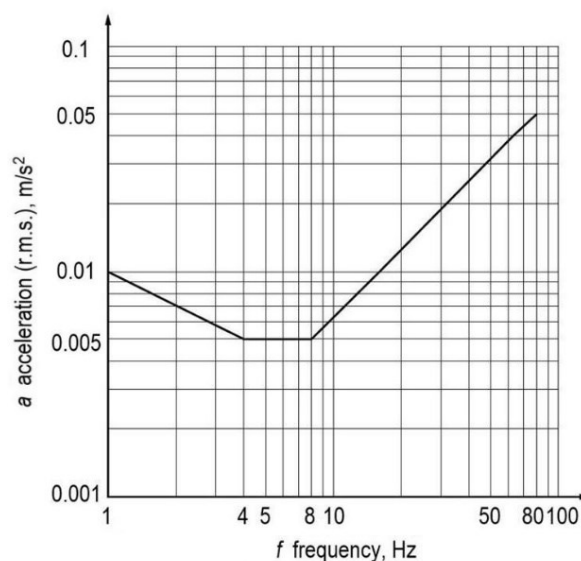


Figure 1. Building vibration z-axis base curve for acceleration (vertical direction) [8]

4 Design methods for CLT floor vibrations

The vibration serviceability design method in current Eurocode 5 [9] essentially refers to the design of joisted floors, where annoying vibration is attributed to isolated floor structure. As CLT floors are solid slabs, their vibration performance differs from that of traditional timber floors. Due to the fact that shear flexibility in CLT is of crucial importance and is already taken into account when calculating deflections, it is also mandatory to consider it in the context of vibrations. CLT slabs can have hinge-like joints between adjacent segments that enforce vertical translation continuity but not continuity of curvature at those locations, which makes their behaviour inconsistent with joisted floors [10]. Due to the orthotropic nature of CLT, floor stiffness is not equal in perpendicular directions, but appropriate support conditions can be provided at all edges. For floor elements supported on four sides, the transverse load-carrying effect should be taken into account. For multi-span systems, the continuous slab effect should be considered.

Multi-storey CLT buildings are generally of platform construction, where each successive storey is built from the floor below; hence, the floor is clamped in between walls of two storeys. A degree of semi-rigidity is therefore expected in all CLT floor-to-wall connections, which, combined with the stiffness of the walls above and below, will influence the dynamic response of the floor [11]. Thus, another highly important aspect of vibrations is seen in the influence of support conditions (e.g., hinged, partly clamped, fully clamped) and in the influence of upper-storey loads transmitted through the walls on the degree of clamping. In addition, the vibration behaviour of CLT floors is strongly influenced by non-load-bearing internal walls, flooring systems, and suspended ceilings [12].

4.1 Design method according to Hamm et al.

The vibration serviceability design method proposed by Hamm et al. [13] is the result of a research project at the Technical University of Munich that involved experimental and theoretical investigations of different types of timber floors (timber-joist floors, timber-concrete floors, and massive timber floors). Based on this research, the Austrian

National Annex NORM B 1995-1-1 [14] was created. It should be noted that this is the only national annex to Eurocode 5 that addresses CLT floor vibrations.

Rules for design and construction applicable to timber floors are divided into three different classes according to Table 1. The first step is to decide whether floors should have higher or lower vibration performance demands, or no demands at all.

In general, the fundamental frequency f_1 of the floor is used for verification of the frequency criterion. The fundamental frequency of a simply supported rectangular floor can be calculated as:

- For floors supported on two sides:

$$f_1 = \frac{\pi}{2 \cdot L^2} \sqrt{\frac{(EI)_L}{m}} \quad [\text{Hz}] \quad (1)$$

- For floors supported on all four sides:

$$f_1 = \frac{\pi}{2 \cdot L^2} \sqrt{\frac{(EI)_L}{m}} \sqrt{1 + \left(\frac{L}{B}\right)^4 \frac{(EI)_B}{(EI)_L}} \quad [\text{Hz}] \quad (2)$$

where:

- L is floor span, in m;
- B is floor width, in m;
- m is mass per unit area of floor, in kg/m².
- $(EI)_L$ is effective stiffness in longitudinal direction of the CLT element (with possible final screed, but without composite action, just adding its own moment of inertia), in Nm²/m;
- $(EI)_B$ is effective stiffness in transverse direction of the CLT element, where $(EI)_L > (EI)_B$, in Nm²/m.

Since subjective evaluation of the vibration behaviour of floors is not correlated with frequency, it is equally important to check the stiffness criterion. Deflection of the floor due to a point load of 2 kN may be determined as follows:

$$w_{2\text{kN}} = \frac{2 \cdot L^3}{48 \cdot (EI)_L \cdot B_{\text{eff}}} \quad [\text{mm}] \quad (3)$$

Table 1. Floor classes, constructive requirements and limiting values of criteria [13]

	Floor class I	Floors class II	Floors class III
Vibration demands	Floors with higher demands	Floors with lower demands	Floors without demands
Description of perception of vibrations	- Vibrations are not perceptible or perceptible only when concentrating on them - Vibrations are not annoying	- Vibrations are perceptible - Vibrations are not annoying	- Vibrations are clearly perceptible - Vibrations are sometimes annoying
Type of use	- Corridors with short span - Floors with different occupancies - Floors in offices	- Floors inside occupancies - Floors in single-family houses under normal use	- Floors under non-residential rooms or roof spaces
Constructive requirements	Floating, heavy or light screed on grit fill or not	Floating, heavy or light screed on grit fill or not	-
Frequency criterion	$f_{\text{limit}} = 8 \text{ Hz}$	$f_{\text{limit}} = 6 \text{ Hz}$	-
Stiffness criterion	$w_{\text{limit}} = 0.5 \text{ mm}$	$w_{\text{limit}} = 1.0 \text{ mm}$	-
Acceleration criterion	$a_{\text{limit}} = 0.05 \text{ m/s}^2$	$a_{\text{limit}} = 0.1 \text{ m/s}^2$	-

with

$$B_{\text{eff}} = \min \left\{ \frac{L}{1.1} \cdot \sqrt[4]{\frac{(EI)_B}{(EI)_L}}; B \right\} \quad (4)$$

where:

B_{eff} is effective floor width for calculating deflection, in m; L , B , $(EI)_L$ and $(EI)_B$ are as previously defined.

The reason for using a load of 2 kN instead of the standard 1 kN was the good correlation between deflection values and subjective vibration behavior evaluation.

In the verification procedure, the vibration serviceability limit state for CLT floors is satisfied if the limiting values given in Table 1 are not exceeded. The fundamental frequency for floors classified as floor classes I and II must be at least $f_{1,\text{min}} = 4.5$ Hz. In the case of floor structure with $f_{1,\text{min}} \leq f_1 \leq f_{\text{limit}}$, the limiting value of vibration acceleration should be satisfied in addition to the stiffness criterion. The value of vibration acceleration can be calculated as follows:

$$a = \frac{F_{\text{dyn}}}{M^* \cdot 2 \cdot \zeta} = \frac{0.4 \cdot F(t)}{0.25 \cdot m \cdot L \cdot B \cdot 2 \cdot \zeta} \quad [\text{m/s}^2] \quad (5)$$

where:

F_{dyn} is total dynamic force that includes factor of 0.4 considering that the force on the floor is acting during a limited time and not always in the middle of the span, in N;

$F(t)$ are harmonic parts of the force on the floor (for third harmonic part $F(t) = 70$ N);

M^* is modal mass of the floor, in kg;

ζ is modal damping ratio of floor construction (for bare CLT floors $\zeta = 0.01$; for CLT floors with floating screed $\zeta = 0.02$);

m , L and B are as previously defined, but for this criterion B should be less than $1.5 \cdot L$.

4.2 Design method according to Thiel et al.

Based on in-situ measurements on CLT buildings at different construction phases conducted by the Competence Centre holz.bauforschungsgmbh Austria, Thiel et al. [15] expanded and modified design method from Hamm et al.

As previously stated, vibration acceleration must be checked if the fundamental frequency is less than the critical value, in addition to frequency and stiffness criteria. Without detailed explanation, as the following equations refer to the previous design method, the focus is on the additional parameters that are taken into account.

When a floor is supported on all four sides, the transverse load-carrying effect should be considered.

That is, both torsional stiffness D_{xy} and effective bending stiffness in the transverse direction $(EI)_B$ should be included in the fundamental frequency calculation, as shown below:

$$f_1 = \frac{\pi}{2 \cdot L^2} \sqrt{\frac{(EI)_L}{m}} \sqrt{1 + \left(\frac{L}{B}\right)^2 \cdot \frac{2 \cdot D_{xy}}{(EI)_L} + \left(\frac{L}{B}\right)^4 \frac{(EI)_B}{(EI)_L}} \quad [\text{Hz}] \quad (6)$$

In addition, shear flexibility in CLT elements should be considered using the effective apparent bending stiffness $(EI)_L$ (based on bending and shear deformations). Additionally, different support conditions and a continuous floor effect for multi-span floors can be considered through modification factors k_m and $k_{t,2}$ that multiply the frequency.

In the examination of the stiffness criterion, the maximum instantaneous vertical deflection due to a concentrated static force $F=1$ kN should be determined and compared with the limit value. Load distribution and shear flexibility should be considered when calculating the deflection:

$$w_{1\text{kN}} = \frac{F \cdot L^3}{48 \cdot (EI)_L \cdot B_{\text{eff}}} + \frac{F \cdot L}{4 \cdot (GA)_L \cdot B_{\text{eff}}} \quad [\text{mm}] \quad (7)$$

where:

B_{eff} is floor effective width according to eq. (4);

$(GA)_L$ is effective shear stiffness in longitudinal direction of the CLT element.

Vibration acceleration depends on the effective (generalised) floor mass M_{gen} , floor fundamental frequency f_1 , excitation frequency f_i (see Table 2), Fourier coefficient of the prevailing harmonic partial oscillation α_{i, f_1} (see Table 2), self-weight of the excitatory person $F_0 = 700$ N and the modal damping ratio ζ . For single-span floors, it may be determined as follows:

$$a = \frac{0.4 \cdot \left(\frac{F_0 \cdot \alpha_{i, f_1}}{M_{\text{gen}}} \right)}{\sqrt{\left(\left(\frac{f_1}{f_i} \right)^2 - 1 \right)^2 + \left(2 \cdot \zeta \cdot \frac{f_1}{f_i} \right)^2}} \quad [\text{m/s}^2] \quad (8)$$

with effective floor mass:

$$M_{\text{gen}} = m \cdot \frac{L}{2} \cdot B_{\text{eff}} \quad [\text{kg/m}^2] \quad (9)$$

where B_{eff} is floor effective width according to eq. (4), but with $B_{\text{eff}} \leq$ half room width $B/2$.

The damping ratio ζ for CLT floors was found to be between 2% and 3.5%, depending on the type of floor construction and support conditions.

Table 2. Fourier coefficients and excitation frequencies based on fundamental frequency [15]

Fundamental frequency f_1 [Hz]	Fourier coefficient α_{i, f_1}	Excitation frequency f_i [Hz]
$4.5 < f_1 \leq 5.1$	0.20	f_1
$5.1 < f_1 \leq 6.9$	0.06	f_1
$6.9 < f_1 \leq 8.0$	0.06	6.9

4.3 Design method according to Hu and Gagnon

Hu and Gagnon [16] developed design criteria based on understanding the fundamentals of CLT floor vibrations as well as laboratory tests and subjective evaluations of vibration floor performance conducted in Canada. The CSA O86 Technical Committee included this vibration-controlled design method in the CLT design guidance of CSA Standard [17].

Based on the laboratory study data analysis, it was found that vibrations induced by normal walking could be effectively controlled by designing a floor with a proper combination of longitudinal stiffness and mass, as expressed by the fundamental frequency f_1 and the 1 kN static deflection w of a 1 m wide CLT panel. The design criterion is expressed as:

- For bare CLT floors or CLT floors with light topping:

$$\frac{f_1}{w^{0.7}} \geq 13.0 \tag{10}$$

- For CLT floors with heavy topping (mass per unit area > 100 kg/m²):

$$\frac{f_1}{w^{0.7}} \geq 20.0 \tag{11}$$

Proposed limit values may be increased for multi-span floors and floors with semi-rigid or rigid support conditions, as these changes in parameters increase the natural frequency.

The fundamental frequency of a simply supported CLT panel may be calculated as follows:

$$f_1 = \frac{\pi}{2 \cdot L^2} \sqrt{\frac{(EI)_L}{\rho A}} \text{ [Hz]} \tag{12}$$

where:

- L is floor span, in m;
- $(EI)_L$ is effective apparent bending stiffness in span direction for 1 m wide panel, which takes into account shear deformation, in Nm²;
- ρ is density of CLT panel, in kg/m³;
- A is cross section area of 1 m wide CLT panel, in m².

Static deflection at mid-span of a simply supported CLT panel under a 1 kN point load may be calculated as:

$$w = \frac{1000 \cdot F \cdot L^3}{48 \cdot (EI)_L} \text{ [mm]} \tag{13}$$

where:

- F is vertical concentrated static force of 1000 N applied at mid-span of the floor;
- L and $(EI)_L$ are as previously defined.

4.4 Design method according to Abeysekera et al.

Abeysekera et al. [18] presented new design rules for the vibration serviceability of timber floors, which are currently being drafted in CEN/TC250/SC5/WG3 Sub-group 4 "Vibrations". The revision of the chapter on vibrations in Eurocode 5 is adapted for use in the design of floor structures made from CLT.

The new design method for human-induced floor vibrations introduces floor performance levels as given in Table 3. Level I stands for the best floor performance level, VI for the worst, but still acceptable, and VII for an unacceptable floor performance level. Table 4 shows the recommendation for selecting the floor performance level for residential categories. Nevertheless, these floor performance levels should be specified in the National annexes of each member country, as it is necessary to consider cultural variations between countries, or they should be specified by investors or designers.

For floor performance levels from I to VI, no further investigations are necessary if requirements in respect to fundamental frequency, acceleration or velocity, and stiffness from Table 3 are satisfied.

In the case of single- or multi-span rectangular floors supported on two or four sides directly onto rigid supports, primarily subjected to uniform loading, the fundamental frequency may be determined as:

$$f_1 = k_{e,1} \cdot k_{e,2} \cdot \frac{\pi}{2 \cdot L^2} \sqrt{\frac{(EI)_L}{m}} \text{ [Hz]} \tag{14}$$

with

$$k_{e,2} = \sqrt{1 + \left(\frac{L}{B}\right)^4 \frac{(EI)_B}{(EI)_L}} \tag{15}$$

Table 3. Floor performance levels and corresponding criteria [18]

Criterion	Floor performance levels							
	I	II	III	IV	V	VI	VII	
Frequency criterion f_1 [Hz] \geq	4.5							
Stiffness criterion w [mm] \leq	0.25	0.5	0.8	1.2	1.6	no criterion		
Response factor $R \leq$	4	8	12	16	20			24
Acceleration criterion (when $f_1 < 8$ Hz) a_{rms} [m/s ²] \leq	$R \times 0.005$							
Velocity criterion (when $f_1 \geq 8$ Hz) v_{rms} [m/s ²] \leq	$R \times 0.0001$							

Table 4. Recommended selection of floor performance levels for residential use category [18]

Use category	Quality choice	Base choice	Economy choice
Residential – multi-storey	Level I, II, III	Level IV	Level V
Residential – single house	Level I, II, III, IV	Level V	Level VI

where:

- $k_{e,1}$ is frequency multiplier in the case of a double-span floor on rigid supports;
- $k_{e,2}$ is frequency multiplier in the case of a two-way spanning floor;
- L is floor span, in m;
- B is floor width, in m;
- $(EI)_L$ is apparent effective bending stiffness in longitudinal floor direction which should take into account shear deformation where applicable and may take into account bending stiffness of floating floor or screed (without composite action), in Nm^2/m ;
- $(EI)_B$ is effective bending stiffness in transverse floor direction, in Nm^2/m ;
- m is mass per unit area of the floor, in kg/m^2 .

When calculating vibrations, floor mass should be a unique value, including at least the sum of mass caused by permanent loads (the self-weight of the floor as well as all supported or suspended horizontal layers). The floor mass may also include mass caused by the quasi-permanent value of uniformly distributed imposed loads. It is recommended to consider only additional mass induced by movable equipment (such as furniture) limited to 10% of total imposed loads.

When all factors affecting deflection are taken into account, such as when floors are partially or completely supported by non-rigid supports or when floors are not only subjected to uniform loading, eq. (14) can be replaced with:

$$f_1 = k_{e,1} \cdot k_{e,2} \cdot \frac{18}{\sqrt{\delta_{sys}}} \quad [Hz] \quad (16)$$

where δ_{sys} is deflection of the floor under self-weight load applied on a single bay in a multi-span case, in mm.

When the fundamental frequency of the floor is below 8 Hz, floor vibration is assumed to be resonant. For resonant vibration design situations, root mean square acceleration a_{rms} may be approximated as:

$$a_{rms} = \frac{0.4 \cdot \alpha \cdot F_0}{\sqrt{2} \cdot 2 \cdot \zeta \cdot M^*} \quad [m/s^2] \quad (17)$$

where:

- α is Fourier coefficient according to the fundamental frequency as $\alpha = e^{-0.4 \cdot f_1}$;
- F_0 is vertical load of a walking person, usually taken as 700 N, in N;
- ζ is modal damping ratio;
- M^* is modal mass (taken as 50% of $m \cdot L \cdot B$ for floors supported on two sides, and as 25% of $m \cdot L \cdot B$ when floor is supported on all four sides), in kg.

When the fundamental frequency of the floor is equal to or above 8 Hz, floor vibration is assumed to be transient. For transient vibration design, root mean square velocity v_{rms} can be approximated as follows:

$$v_{rms} = \beta \cdot v_{tot,peak} = \beta \cdot k_{imp} \cdot v_{1,peak} = \beta \cdot k_{imp} \cdot k_{red} \cdot \frac{l}{M^*} \quad [m/s] \quad (18)$$

with

$$k_{imp} = \max \left\{ \begin{array}{l} 0.48 \cdot \left(\frac{B}{L} \right) \cdot \left(\frac{(EI)_L}{(EI)_B} \right)^{0.25} \\ 1.0 \end{array} \right\} \quad (19)$$

$$l = \frac{42 f_w^{1.43}}{f_1^{1.3}} \quad (20)$$

where:

- $\beta = (0.65 - 0.01 \cdot f_1) \cdot (1.33 - 11.0 \cdot \zeta) \cdot \eta$;
- $\eta = 1.52 - 0.55 \cdot k_{imp}$ when $1.0 \leq k_{imp} \leq 1.5$, else $\eta = 0.69$;
- $v_{tot,peak}$ is total peak velocity response, in m/s;
- k_{imp} is impulse multiplier factor;
- $v_{1,peak}$ is peak velocity response for fundamental mode, in m/s;
- k_{red} is reduction factor with a value of 0.7 considering that exciting source on floor and sensing person are at a distance from each other;
- l is mean modal impulse, in Ns;
- f_w is walking frequency and is assumed to be 1.5 Hz for residential floors, in Hz;
- ζ is modal damping ratio;
- $M^*, L, B, (EI)_L, (EI)_B$ and f_1 are as previously defined.

Realistic floor damping values are needed for the design procedure. Unless other values are proven to be more appropriate, the modal damping ratio for CLT floors may be assumed to be between 2.5 and 6% depending on floor construction, support conditions, the presence of non-load-bearing partitions, and the presence of people on the floor.

For all floors, there is a stiffness criterion that checks maximum deflection due to a single point load of 1 kN placed in the most unfavourable position of a single span floor strip having an effective width B_{eff} calculated according to eq. (4). Although this empirical criterion based on historical practice is not very relevant for CLT floors due to the neglect of floor mass, it allows an approximate comparison of proposed performance levels with existing requirements. The maximum deflection in mid-span of a single-span floor may be calculated as follows:

$$w = \frac{F \cdot L^3}{48 \cdot (EI)_L \cdot B_{eff}} \quad [mm] \quad (21)$$

where all of the parameters are as previously defined.

5 Calculation of the stiffness properties of CLT floors

As stiffness properties participate in each vibrational serviceability design method, it is important to specify how they can be calculated. Even though advanced plate theories were proposed, the current design of CLT elements, usually treated as one-meter-wide panel strips under transverse load, is based on beam theories. Traditional Euler-Bernoulli beam theory is the most commonly used approach for bending elements. However, as a result of shear deformations in CLT elements, it cannot be applied directly. There are basically three analytical methods for calculating the bending properties of CLT floors: the Gamma method, the K-method, and the Shear analogy method [19]. The main assumption when applying these methods is that floors are simply supported, loaded perpendicular to their plane, and carry load only in one longitudinal direction.

5.1 Gamma method

The Gamma method is based on the theory of a mechanically joined beams and is mostly used for beams with member sections flexibly connected by mechanical fasteners that are evenly spaced. Cross-sections and joint stiffness are constant in the direction of the beam axis. Shear deformation is accounted for by connection efficiency factors γ , which increase bending deformation, where $\gamma = 1,0$ represents a rigid connection and $\gamma = 0$ represents a non

connection at all. The Gamma method is shown in Annex B of Eurocode 5 [9], and current European Technical Approvals (ETA) have adopted this method for CLT bending elements.

Certain changes to the original theory were introduced so that it could be applied to CLT panels. Assuming that only boards in the longitudinal direction are carrying the load, only longitudinal layers are used for calculating the effective bending stiffness. The effect of cross layers is considered only through their rolling shear properties as the stiffness of imaginary fasteners connecting longitudinal layers. Shear deformations in longitudinal layers are ignored, so this method should be applied to CLT floors with span-to-depth ratios greater than 10.

Effective bending stiffness in the longitudinal direction, for cases with two or three longitudinal layers, is defined as follows:

$$(EI)_{L,eff} = \sum_{i=1}^n (E_i \cdot I_i + \gamma_i \cdot E_i \cdot A_i \cdot z_i^2) \quad (22)$$

with

$$\gamma_i = \frac{1}{1 + \frac{\pi^2 \cdot E_i \cdot A_i}{L^2} \cdot \frac{t_{i,2}}{G_{R,i,2} \cdot b}} \quad \text{for } i = 1 \text{ and } i = 3 \quad (23)$$

and

$$\gamma_2 = 1 \quad (24)$$

where:

- n is number of longitudinal layers;
- E_i is modulus of elasticity parallel to the grain of the i -th longitudinal layer;
- I_i is moment of inertia of the i -th longitudinal layer ($I_i = b \cdot t_i^3 / 12$);
- A_i is cross-section area of the i -th longitudinal layer ($A_i = b \cdot t_i$);
- b is width of CLT cross-section (usually taken as 1 m);
- t_i is thickness of the i -th longitudinal layer;
- z_i is distance between the center point of the i -th longitudinal layer and neutral axis of CLT cross-section, as presented in Figure 2;
- $t_{i,2}$ is thickness of cross layer next to the i -th layer;
- $G_{R,i,2}$ is shear modulus perpendicular to the grain (rolling shear modulus) of cross layer next to the i -th layer; it can be assumed to be 1/10 of shear modulus parallel to the grain G_0 ;
- L is span of CLT panel.

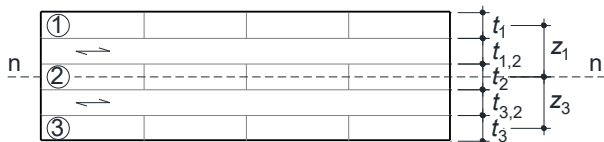


Figure 2. Cross-section of symmetrical 5-layer CLT panel with relevant distances and thicknesses for the Gamma method

The Gamma method has an advantage over other methods for panels with asymmetrical cross-sections due to the different layer thicknesses or material properties of the layers. However, this method can be difficult to apply in multi-span floors and when a CLT panel has more than five layers.

Furthermore, the Gamma method cannot provide precise effective stiffness in the transverse direction.

5.2 K-method

Blass and Fellmoser [20] established the K-method by applying the theory of composite materials to CLT panels. In this method, it is assumed that the stiffness of each layer adds to the effective bending stiffness of a CLT panel when it is bent. Since this method does not take into account how shear deformation affects each layer, it works best for CLT floors with a high span-to-depth ratio (greater than 30).

To obtain the value of effective bending stiffness $(EI)_{eff}$, the modulus of elasticity parallel to the grain E_0 of each individual layer needs to be multiplied by a composition factor k_i depending on certain loading configurations, as well as on the panel orientation. For floors loaded perpendicular to their plane, it is relevant to use k_1 and k_2 composite factors for longitudinal and transverse floor directions. Hence, effective bending stiffnesses in longitudinal and transverse directions, respectively, are defined as follows:

$$(EI)_{L,eff} = E_0 \cdot \frac{b \cdot a_m^3}{12} \cdot k_1 \quad (25)$$

and

$$(EI)_{B,eff} = E_0 \cdot \frac{b \cdot a_m^3}{12} \cdot k_2 \quad (26)$$

with

$$k_1 = 1 - \left(1 - \frac{E_{90}}{E_0} \right) \cdot \frac{a_{m-2}^3 - a_{m-4}^3 + \dots \pm a_1^3}{a_m^3} \quad (27)$$

$$k_2 = \frac{E_{90}}{E_0} + \left(1 - \frac{E_{90}}{E_0} \right) \cdot \frac{a_{m-2}^3 - a_{m-4}^3 + \dots \pm a_1^3}{a_m^3} \quad (28)$$

where:

- E_0 is modulus of elasticity parallel to the grain of individual layer;
- E_{90} is modulus of elasticity perpendicular to the grain of individual layer; it can be assumed to be 1/30 of modulus of elasticity parallel to the grain E_0 ;
- b is width of CLT cross-section (usually taken as 1 m);
- m is total number of layers;
- $a_m, a_{m-2}, a_{m-4}, \dots, a_1$ are relevant thicknesses of the panel.

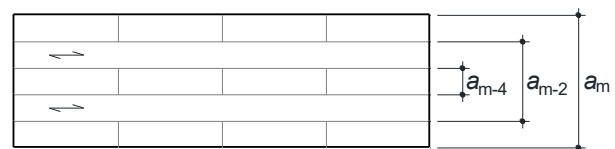


Figure 3. Cross-section of symmetrical 5-layer CLT panel with relevant thicknesses for K-method

For a 5-layer CLT panel, a_m is the thickness of the whole panel, a_{m-4} is the thickness of the middle layer, and a_{m-2} is the panel thickness minus the thickness of the outer layers (Figure 3).

5.3 Shear analogy method

The shear analogy method was developed by Kreuzinger [21] and shares many similarities with the Timoshenko beam theory. This method takes into account shear deformation of

both longitudinal and cross layers and has been proven to be the best model for calculating the bending stiffness of CLT panels. This method has been implemented in Canadian and American standards for the design of timber structures [22].

The main principle of the shear analogy method is that the cross-section of a CLT panel is approximated with two rigidly coupled virtual beams that have equal deflection. One virtual beam has a bending stiffness equal to the sum of the inherent bending stiffnesses of each layer with infinite shear stiffness, while the bending stiffness of the second virtual beam is presented as the sum of the Steiner points of each layer (Steiner's theorem) with definite shear stiffness. Based on this, effective bending stiffness and effective shear stiffness in the longitudinal floor direction, respectively, can be calculated as follows:

$$(EI)_{L,eff} = \sum_{i=1}^n \left(E_i \cdot b \cdot \frac{t_i^3}{12} \right) + \sum_{i=1}^n (E_i \cdot A_i \cdot z_i^2) \quad (29)$$

and

$$(GA)_{L,eff} = \frac{\left(h - \frac{t_1}{2} - \frac{t_n}{2} \right)^2}{\left[\left(\frac{t_1}{2 \cdot G_1 \cdot b} \right) + \left(\sum_{i=2}^{n-1} \frac{t_i}{G_i \cdot b} \right) + \left(\frac{t_n}{2 \cdot G_n \cdot b} \right) \right]} \quad (30)$$

where:

- n is total number of layers;
- E_i is modulus of elasticity of the i -th individual layer (taken as E_0 for longitudinal layers and E_{90} for transverse layers);
- A_i is cross-section area of the i -th individual layer ($A_i = b \cdot t_i$);
- b is width of CLT cross-section (usually taken as 1 m);
- t_i is thickness of the i -th individual layer;
- z_i is distance between the center point of the i -th layer and neutral axis, as presented in Figure 4;
- h is thickness of the panel;
- G_i is shear modulus of the i -th individual layer (taken as G_0 for longitudinal layers and G_{90} for transverse layers).

In the case of floors supported on all four sides, effective bending stiffness in transverse direction should be obtained as follows:

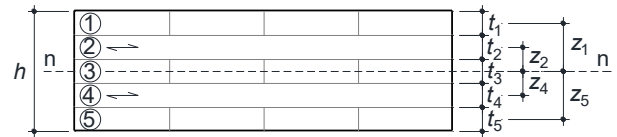


Figure 4. Cross-section of symmetrical 5-layer CLT panel with relevant distances and thicknesses for the Shear analogy method

$$(EI)_{B,eff} = \sum_{i=2}^{n-1} \left(E_i \cdot b \cdot \frac{t_i^3}{12} \right) + \sum_{i=2}^{n-1} (E_i \cdot A_i \cdot z_i^2) \quad (31)$$

When calculating deflections and vibrations of a CLT floor, effective bending and shear stiffness are included through apparent bending stiffness, defined as:

$$(EI)_{L,app} = \frac{(EI)_{L,eff}}{1 + \frac{K_s \cdot (EI)_{L,eff}}{(GA)_{L,eff} \cdot L^2}} \quad (32)$$

where K_s is constant based on the influence of shear deformation, depending on loading configuration and boundary conditions (taken as 11.5 for uniformly distributed load and floors simply supported on two sides).

The Shear analogy method is accurate for various load configurations and multi-span systems and is not limited by the number of layers within a panel. It is best suited to floor structures with span-to-depth ratios greater than 8.

6 Discussion

Overall criteria that should be checked through different design methods are presented in Table 5. The verification of the frequency and stiffness criterion is shared by all methods. Some of them also prove vibration velocity and acceleration. The critical frequency of most design methods is 8 Hz.

Although some criteria are common to certain methods, it may happen that the same criteria take into account different factors. This may lead to noticeably different results. An overview of differences in consideration of some factors is given in Table 6.

Table 5. Overview of considered criteria in different design methods

Method	Frequency	Stiffness criterion	Velocity criterion	Acceleration criterion
Hamm [13]	yes	yes	no	yes
Thiel [15]	yes	yes	no	yes
Hu [16]	yes	yes	no	no
Abeysekera [18]	yes	yes	yes	yes

Table 6. Overview of considered factors in different design methods

Method	Support conditions	Shear flexibility	Transverse load-carrying effect	Effective width B_{eff}	Mass
Hamm [13]	no	no	yes	yes	$g_0 + \Delta g$
Thiel [15]	yes	yes	yes	yes	$g_0 + \Delta g$
Hu [16]	no	yes	no	no	g_0
Abeysekera [18]	yes	no	yes	yes	$g_0 + \Delta g + \psi_2 \cdot p$

The support conditions have a large effect on the values of natural frequencies. When the floor is clamped or partially clamped, the frequencies increase. When loads from the upper floor are transferred through walls, the floor can be clamped. This will also have a positive effect on floor deflections. From the aspect of CLT as a material, shear flexibility is of crucial importance, and it is highly advised to take it into account in the context of vibrations. This implies that the Shear analogy method should be used when calculating the stiffness properties of CLT floors. Consideration of shear flexibility leads to a decrease in fundamental frequency and an increase in deflection. The transverse load-carrying effect should be considered when the floor is supported on all four sides. This parameter raises the floor's fundamental frequency, which depends mostly on the ratio of bending stiffness in the longitudinal and transverse directions as well as on the ratio of floor width to span. Effective floor width B_{eff} has an impact on floor deflection in such a way that taking the effective width into account reduces floor deflection. As with the previous parameter, this influence greatly depends on the ratio of bending stiffnesses. Floor mass affects floor natural frequencies and vibration acceleration, so an increase in the mass leads to lower natural frequencies and also vibration acceleration. Taking into account more mass according to vibration sensitivity has more positive than negative effects. Permanent loads should always be considered, but in certain cases it is reasonable to include quasi-permanent parts of imposed loads.

When speaking of limit values, it is evident that limit values for proposed criteria are based on the highly subjective opinion of the test person. Hence, it is impossible to define which design method would be best suited for verifying vibrations. In order to get a better description of the actual behaviour of floor structure, a floor classification system based on vibration serviceability performance was developed. Floor classification based on dynamic characteristics (different limit values of criteria) allows designers and investors to be more aware of actual floor performance and to target desired floor performance.

7 Conclusion

Human-induced floor vibrations are regarded as a serviceability issue, primarily relating to occupant discomfort. Although vibration serviceability issues with timber floors are primarily associated with existing floors, they are also relevant to new floors. Taking contemporary trends into account, it is realistic to expect that in the future floor spans will be even larger, floors even lighter, and human expectations regarding the quality of living and working surroundings will be even greater. Therefore, it is necessary to define an adequate method (criteria) in current standards that would predict excessive vibrations, thus enabling the given problems to be eliminated or decreased during the design stage. Although the procedure must be simple in practice, it must not be at the expense of accuracy.

Due to the specific dynamic behaviour of CLT floors, the existing design methods for low- and high-frequency floors may not be applicable to CLT floors. There are several methods specifically for the verification of CLT floor vibrations. However, it is currently impossible to define which design guidelines would be best suited for the prediction of unacceptable vibrations. This is because the criteria and their limit values differ. Any reliable design approach should be derived from predictable and measurable parameters and should reflect the type of occupancy for which it is intended.

It seems that the development of contemporary probabilistic methods can significantly change the approach to the problem of floor vibrations. Classification of floors based on the target response to vibration excitations (different limit values of criteria) has the advantage of providing a tool by which designers and investors can be more aware of actual floor performance.

Acknowledgements

The Science Fund of the Republic of Serbia supported this research with Grant No. 7677448: "Towards Sustainable Buildings: Novel Strategies for the Design of Vibration Resistant Cross-Laminated Timber Floors -- Substrate4CLT."

References

- [1] L. Hanagan, T. Murray, Active control approach for reducing floor vibrations, *Journal of Structural Engineering* 123(11) (1997) 1497-1505.
- [2] J. Weckendorf, T. Toratti, I. Smith, T. Tannert, Vibration serviceability performance of timber floors, *European Journal of Wood and Wood Products* 74 (2016) 353-367.
- [3] I. Smith, Vibration of timber floors: Serviceability aspects, in: S. Thelandersson, H. Larsen (Eds.), *Timber Engineering*, Wiley, Chichester, England, 2009, pp. 241-266.
- [4] G. Pernica, Dynamic load factors for pedestrian movements and rhythmic exercises, *Canadian Acoustics*, 18(2) (1990), 3-18.
- [5] K. Järnerö, Vibrations in timber floors – dynamic properties and human perception, PhD Thesis, Linnaeus University, Sweden, 2014.
- [6] L.J. Hu, Y.H. Chui, D.M. Onysko, Vibration serviceability of timber floors in residential construction, *Progress in Structural Engineering and Materials* 3 (2001) 228-237.
- [7] A. Pavić, P. Reynolds, Vibration serviceability of long-span concrete building floors. Part 1: Review of background Information, *Shock and Vibration Digest* 34(3) (2002) 191-211.
- [8] ISO 10137: Bases for design of structures – Serviceability of buildings and walkways against vibrations, International Organisation for Standardization, Switzerland, 2007.
- [9] EN 1995-1-1: Eurocode 5: Design of timber structures - Part 1-1: General - Common rules and rules for buildings, European Committee for Standardization - CEN, Brussels, Belgium, 2004.
- [10] E. Ussher, K. Arjomandi, J. Weckendorf, I. Smith, Prediction of motion responses of cross-laminated-timber slabs, *Structures* 11 (2017) 49-61.
- [11] C.U. Chulain, K. Sikora, A. Hart, Influence of connection systems on serviceability response of CLT timber flooring, *World Conference on Timber Engineering – WCTE 2012*, pp. 4214-4221, Vienna, Austria, 2016.
- [12] S. Zimmer, M. Augustin, Vibrational behavior of cross laminated timber floors in residential buildings, *World Conference on Timber Engineering – WCTE 2016*, pp. 4803-4812, Vienna, Austria, 2016.
- [13] P. Hamm, A. Richter, S. Winter, Floor vibrations – new results, *World Conference on Timber Engineering – WCTE 2010*, Trentino, Italy, 2010.

- [14] ÖNORM B 1995-1-1: Eurocode 5: Bemessung und Konstruktion von Holzbauten, Teil 1-1: Allgemeines – Allgemeine Regeln und Regeln für den Hochbau (konsolidierte Fassung). Österreichisches Normungsinstitut, Vienna, Austria, 2015.
- [15] A. Thiel, S. Zimmer, M. Augustin, G. Schickhofer, CLT and floor vibrations: A comparison of design methods, CIB - W18 Meeting 46, paper 46-20-1, Canada, 2013.
- [16] L. Hu, S. Gagnon, Controlling cross-laminated timber floor vibrations: Fundamentals and method, World Conference on Timber Engineering – WCTE 2012, pp. 269-275, Auckland, New Zealand, 2012.
- [17] CSA 086: Engineering Design in Wood, Canadian Standards Association, Mississauga, Ontario, Canada, 2019.
- [18] I.K. Abeysekera, P. Hamm, T. Toratti, A. Lawrence, Development of a floor vibration design method for Eurocode 5, INTER Meeting 51, paper 51-20-2, Estonia, 2018.
- [19] Lj. Kozarić, A. Prokić, M. Bešević, Cross laminated timber elements in contemporary timber structures of buildings – application and design, Constr. Build. Mater. 58 (2015) 4 (51-69).
- [20] H.J. Blass, P. Fellmoser, Design of solid wood panels with cross layers, World Conference on Timber Engineering – WCTE 2004, pp. 543-548, Lahti, Finland, 2004.
- [21] H. Kreuzinger, Platten, Scheiben und Schalen - ein Berechnungsmodell für gängige Statikprogramme [Plate and shell structures - A calculation model for common structural analysis programs], Bautechnik 1(1999) 34–39.
- [22] E. Karacabeyli, S. Gagnon (Eds.), Canadian CLT Handbook, Volume 1, FPInnovations, Pointe-Claire, QC, Canada, 2019.



Building Materials and Structures

GUIDE FOR AUTHORS

In the journal *Building Materials and Structures*, the submission and review processes take place electronically. Manuscripts are submitted electronically (online) on the website [https:// www.dimk.rs](https://www.dimk.rs). The author should register first, then log in and finally submit the manuscript which should be in the form of editable files (e.g. Word) to enable the typesetting process in journal format. All correspondence, including Editor's decision regarding required reviews and acceptance of manuscripts, take place via e-mail.

Types of articles

The following types of articles are published in *Building Materials and Structures*:

Original scientific article. It is the primary source of scientific information, new ideas and insights as a result of original research using appropriate scientific methods. The results are presented briefly, but in a way to enable readers to assess the results of experimental or theoretical/numerical analyses, so that the research can be repeated and yield with the same or results within the limits of tolerable deviations.

Review article. It presents the state of science in particular area as a result of methodically systematized, analyzed and discussed reference data. Only critical review manuscripts will be considered as providing novel perspective and critical evaluation of the topics of interest to broader BMS readership.

Preliminary report. Contains the first short notifications of research results without detailed analysis, i.e. it is shorter than original research paper.

Technical article. Reports on the application of recognized scientific achievements of relevance to the field of building materials and structures. Contain critical analysis and recommendations for adaption of the research results to practical needs.

Projects Notes. Project Notes provide a presentation of a relevant project that has been built or is in the process of construction. The original or novel aspects in design or construction should be clearly indicated.

Discussions. Comment on or discussion of a manuscript previously published in *Building Materials and Structures*. It should be received by the Editor-in-Chief within six months of the online publication of the manuscript under discussion. Discussion Papers will be subject to peer review and should also be submitted online. If Discussion Paper is selected for publication the author of the original paper will be invited to respond, and Discussion Paper will be published alongside any response that the author.

Other contributions

Conference Reports. Reports on major international and national conferences of particular interest to *Building Materials and Structures*. Selected and/or awarded papers from the ASES Conferences are published in Special issues.

Book Reviews. Reviews on new books relevant to the scope of *Building Materials and Structures*.

Manuscript structure

The manuscript should be typed one-sided on A4 sheets. Page numbers should be included in the manuscript and the text should be single spaced with consecutive line numbering - these are essential peer review requirements. The figures and tables included in the single file should be placed next to the relevant text in the manuscript. The corresponding captions should be placed directly below the figure or table. If the manuscript contains Supplementary material, it should also be submitted at the first submission of the manuscript for review purposes.

There are no strict rules regarding the structure of the manuscript, but the basic elements that it should contain are: Title page with the title of the manuscript, information about the authors, abstract and keywords, Introduction, Materials / Methods, Results and Conclusions.

The front page

The front page contains the title of the manuscript which should be informative and concise; abbreviations and formulas should be avoided.

Information about the authors are below the title; after the author's name, a superscript number is placed indicating his/her affiliation, which is printed below the author's name, and before the abstract. It is obligatory to mark the corresponding author with superscript *) and provide his/her e-mail address. The affiliation should contain the full name of the institution where the author performed the research and its address.

Abstract

Abstract should contain 150-200 words. Motivation and objective of the conducted research should be presented; main results and conclusions should be briefly stated as well. References and abbreviations should be avoided.

Keywords

Keywords (up to 10) should be listed immediately after the abstract; abbreviations should be used only if they are generally accepted and well-known in the field of research.

Division into chapters

The manuscript should be divided into chapters and sub-chapters, which are hierarchically numbered with Arabic numbers. The headings of chapters and sub-chapters should appear on their own separate lines.

Appendices

The manuscript may have appendices. If there is more than one appendix, they are denoted by A, B, etc. Labels of figures, tables and formulas in appendices should contain the label of the appendix, for example Table A.1, Figure A.1, etc.

Acknowledgments

At the end of the manuscript, and before the references, it is obligatory to list institutions and persons who financially or in some other way helped the presented research. If the research was not supported by others, it should also be stated in this part of the manuscript.

Abbreviations

All abbreviations should be defined where they first appear. Consistency of abbreviations used throughout the text should be ensured.

Math formulae

Formulae should be in the form of editable text (not in the format of figures) and marked with numbers, in the order in which they appear in the text. The formulae and equations should be written carefully taking into account the indices and exponents. Symbols in formulae should be defined in the order they appear, right below the formulae.

Figures

- figures should be made so that they are as uniform in size as possible and of appropriate quality for reproduction;
- the dimensions of the figures should correspond to the format of the journal: figures with a width approximately equal to the width of 1 column (± 80 mm width), width of 2 columns (± 170 mm width) or width of 1.5 columns (± 130 mm width);
- figures should be designed so that their size is not disproportionately large in relation to the content;
- the text on the figures should be minimal and the font used should be the same on all figures (Arial, Times New Roman, Symbol);
- figures should be placed next to the appropriate text in the manuscript and marked with numbers in the order in which they appear in the text;
- each figure should have a caption that is placed below the figure - the caption should not be on the figure itself.

In cases of unadequate quality of reproduction the author should be required to submit figures as separate files. In this case, the figure should be saved in TIFF (or JPG) format with a minimum resolution of 500 dpi.

Tables

- tables should be in the form of editable text (not in the format of figures);
- tables should be placed next to the appropriate text in the manuscript and marked with numbers in the order in which they appear in the text;
- each table should have a caption that is placed below the table;
- the tables should not show the results that are already presented elsewhere in the manuscript - duplicating the presentation of results should be avoided;
- tables are without vertical lines as boundaries between cells and shading cells.

References

Citation in the text

Each reference cited in the text should be in the reference list (and vice versa). It is not recommended to list unpublished results or personal communications in the reference list, but they can be listed in the text. If they are still listed in the reference list, the journal style references are used, with 'Unpublished results' or 'Personal communication' instead of the date of publication. Citing a reference as 'in press' means that it is accepted for publication.

Web references

Web references are minimally listed with the full URL and the date when the site was last accessed. These references can be included in the reference list, but can also be given in a separate list after the reference list.

Reference style

In text: References are given in the text by a number in square brackets in the order in which they appear in the text. Authors may also be referred to directly, but the reference number should always be given.

In reference list: References marked with a number in square brackets are sorted by numbers in the list.

Examples

Reference to a journal publication:

[1] V.W.Y. Tam, M. Soomro, A.C.J. Evangelista, A review of recycled aggregate in concrete applications (2000-2017), *Constr. Build. Mater.* 172 (2018) 272-292. <https://doi.org/10.1016/j.conbuildmat.2018.03.240>.

Reference to a book:

[3] A.H. Nilson, D. Darwin, C.W. Dolan, *Design of Concrete Structures*, thirteenth ed., Mc Graw Hill, New York, 2004.

Reference to a chapter in an edited book:

[4] J.R. Jimenez, Recycled aggregates (RAs) for roads, in: F Pacheco-Torgal, V.W.Y. Tam, J.A. Labrincha, Y. Ding, J. de Brito (Eds.), *Handbook of recycled concrete and demolition waste*, Woodhead Publishing Limited, Cambridge, UK, 2013, pp. 351–377.

Reference to a website:

[5] WBCSD, The Cement Sustainability Initiative, World. Bus. Council. Sustain. Dev. <http://www.wbcscement.org/pdf/CSIRecyclingConcrete-FullReport.pdf>, 2017 (accessed 7 July 2016).

Supplementary material

Supplementary material such as databases, detailed calculations and the like can be published separately to reduce the workload. This material is published 'as received' (Excel or PowerPoint files will appear as such online) and submitted together with the manuscript. Each supplementary file should be given a short descriptive title.

Ethics in publishing

Authors are expected to respect intellectual and scientific integrity in presentation of their work.

The journal publishes manuscripts that have not been previously published and are not in the process of being considered for publication elsewhere. All co-authors as well as the institution in which the research was performed should agree to the publication in the journal. The authors are obliged not to publish the research which is already published in this journal (electronically or in print) in the same form, in English or any other language, without the written consent of the Copyright owner.

Authors are expected to submit completely original research; if the research of other researchers is used, it should be adequately cited. Authors who wish to include in their manuscript images, tables or parts of text that have already been published somewhere, should obtain permission from the Copyright owner and provide a proof in the process of submitting the manuscript. All material for which there is no such evidence will be considered the original work of the author. To determine the originality of the manuscript, it can be checked using the Crossref Similarity Check service.

The Journal and Publishers imply that all authors, as well as responsible persons of the institute where the research was performed, agreed with the content of the submitted manuscript before submitting it. The Publishers will not be held legally responsible should there be any claims for compensation.

Peer Review

This journal uses a single blind review process, which means that the authors do not know the names of the reviewers, but the reviewers know who the authors are. In the review process, the Editor-in-Chief first assesses whether the contents of the manuscript comply with the scope of the journal. If this is the case, the paper is sent to at least two independent experts in the field, with the aim of assessing its scientific quality and making recommendation regarding publication. If the manuscript needs to be revised, the authors are provided with the reviewers' remarks. The authors are obliged to correct the manuscript in accordance with the remarks, submit the revised manuscript and a special file with the answers to the reviewers within the given deadline. The final decision, whether the paper will be published in journal or not, is made by the Editor-in-Chief.

After acceptance

Once accepted for publication, the manuscript is set in the journal format. Complex manuscript is sent to the authors in the form of proof, for proof reading. Then, authors should check for typesetting errors, and whether the text, images, and tables are complete and accurate. Authors are asked to do this carefully, as subsequent corrections will not be considered. In addition, significant changes to the text and authorship at this stage are not allowed without the consent of the Editor-in-Chief. After online publication, changes are only possible in the form of Erratum which will be hyperlinked for manuscript.

Copyright

Authors retain copyright of the published papers and grant to the publisher the non-exclusive right to publish the article, to be cited as its original publisher in case of reuse, and to distribute it in all forms and media.

The published articles will be distributed under the Creative Commons Attribution ShareAlike 4.0 International license ([CC BY-SA](https://creativecommons.org/licenses/by-sa/4.0/)). It is allowed to copy and redistribute the material in any medium or format, and remix, transform, and build upon it for any purpose, even commercially, as long as appropriate credit is given to the original author(s), a link to the license is provided, it is indicated if changes were made and the new work is distributed under the same license as the original.

Users are required to provide full bibliographic description of the original publication (authors, article title, journal title, volume, issue, pages), as well as its DOI code. In electronic publishing, users are also required to link the content with both the original article published in *Building Materials and Structures* and the licence used.

Authors are able to enter into separate, additional contractual arrangements for the non-exclusive distribution of the journal's published version of the work (e.g., post it to an institutional repository or publish it in a book), with an acknowledgement of its initial publication in this journal.

Open access policy

Journal *Building Materials and Structures* is published under an Open Access licence. All its content is available free of charge. Users can read, download, copy, distribute, print, search the full text of articles, as well as to establish HTML links to them, without having to seek the consent of the author or publisher.

The right to use content without consent does not release the users from the obligation to give the credit to the journal and its content in a manner described under *Copyright*.

Archiving digital version

In accordance with law, digital copies of all published volumes are archived in the legal deposit library of the National Library of Serbia in the Repository of SCIndeks - The Serbian Citation Index as the primary full text database.

Cost collection to authors

Journal *Building Materials and Structures* does not charge authors or any third party for publication. Both manuscript submission and processing services, and article publishing services are free of charge. There are no hidden costs whatsoever.

Disclaimer

The views expressed in the published works do not express the views of the Editors and the Editorial Staff. The authors take legal and moral responsibility for the ideas expressed in the articles. Publisher shall have no liability in the event of issuance of any claims for damages. The Publisher will not be held legally responsible should there be any claims for compensation.

Financial support



**MINISTRY OF EDUCATION, SCIENCE AND
TECHNOLOGICAL DEVELOPMENT OF
REPUBLIC OF SERBIA**



**INSTITUTE FOR TESTING OF MATERIALS-
IMS INSTITUTE, BELGRADE**



SERBIAN CHAMBER OF ENGINEERS